UNIVERSITÀ DI PARMA

Dottorato di ricerca in SCIENZE CHIMICHE

Ciclo XXX

Organic Molecular Materials: Crystal Growth and Spectroscopic Characterization

Coordinatore:
Prof. Roberto Corradini
Tutor:
Prof. Alberto Girlando e **Dott. Matteo Masino**

Dottorando: **Nicola Castagnetti**

2014-2017

Contents

Introduction

The information society we belong to has his roots in the development of the materials for electronics, first and foremost on the transistor and other devices based on silicon. In the mid of the last century people started to consider organic molecular material as possible alternatives to Si, giving birth to the field of organic molecular materials. Indeed back in 1989 a special issue of the journal *Molecular Crystals and Liquid Crystals* had the title “Studies of Organic Semiconductors for 40 Years” [1], but at the time the investigations were far from the application stage. As a matter of fact, after this special issue the research on electronic devices based on organic semiconductor fell into almost oblivion for a long time, the attention being shifted to organic conductors, superconductors, electroluminescent, magnetic materials and so on [2].

Interest in molecular materials as potential Field Effect Transistors (FET) resurrected about 15 years ago, when progress in the synthesis and purification techniques showed that mobilities μ comparable or superior to amorphous silicon (a-Si:H) could be achieved (see Fig. 1) [3].

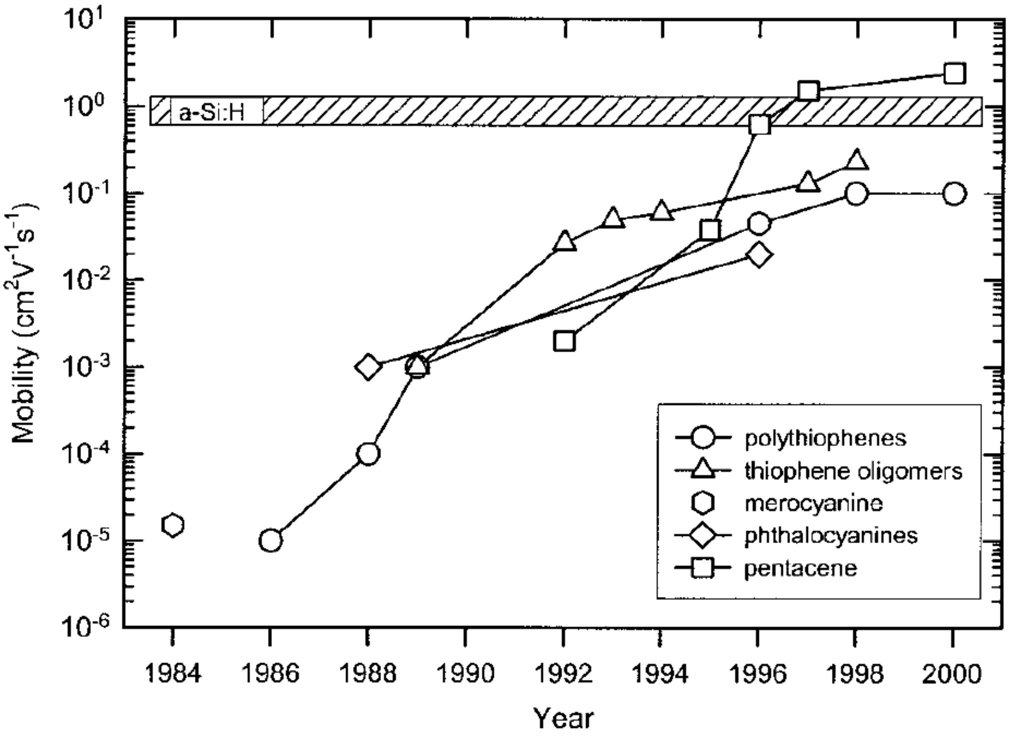

Figure 1: Time progress of hole mobilities of organic semiconductors (from Ref. [3]).

Since then, the field has enjoyed huge progress, and nowadays hole or electron mobilities of the order of a few tenths of cm^2 V^{-1} s^{-1} have been commonly achieved, with organic polymers lagging just a little below. The advantage of organic materials with respect to Si is the low-temperature processing and the possibility of building large area, flexible devices, with the additional bonus offered by the complexity of molecular systems, which opens the way to a wide variety of new and multiple functionalities [4].

The present Thesis is focused on two emerging trends of the research on organic molecular materials. The first concerns the search of bio-compatible molecules [5] to reduce the actual massive amount of waste of electronic equipment. The second concerns the use of two-component, mixed stack charge transfer (CT) crystals, as it has been suggested that they might be good semiconductors with balanced hole *and* electron transport [6], coupled to the possibility of tuning the band gap and the potential control of the packing design [7]. In general, flat, π-conjugated molecules constitute the building blocks of organic materials. The chemical formula and related acronyms of the molecules considered in the present Thesis are reported in Fig.2.

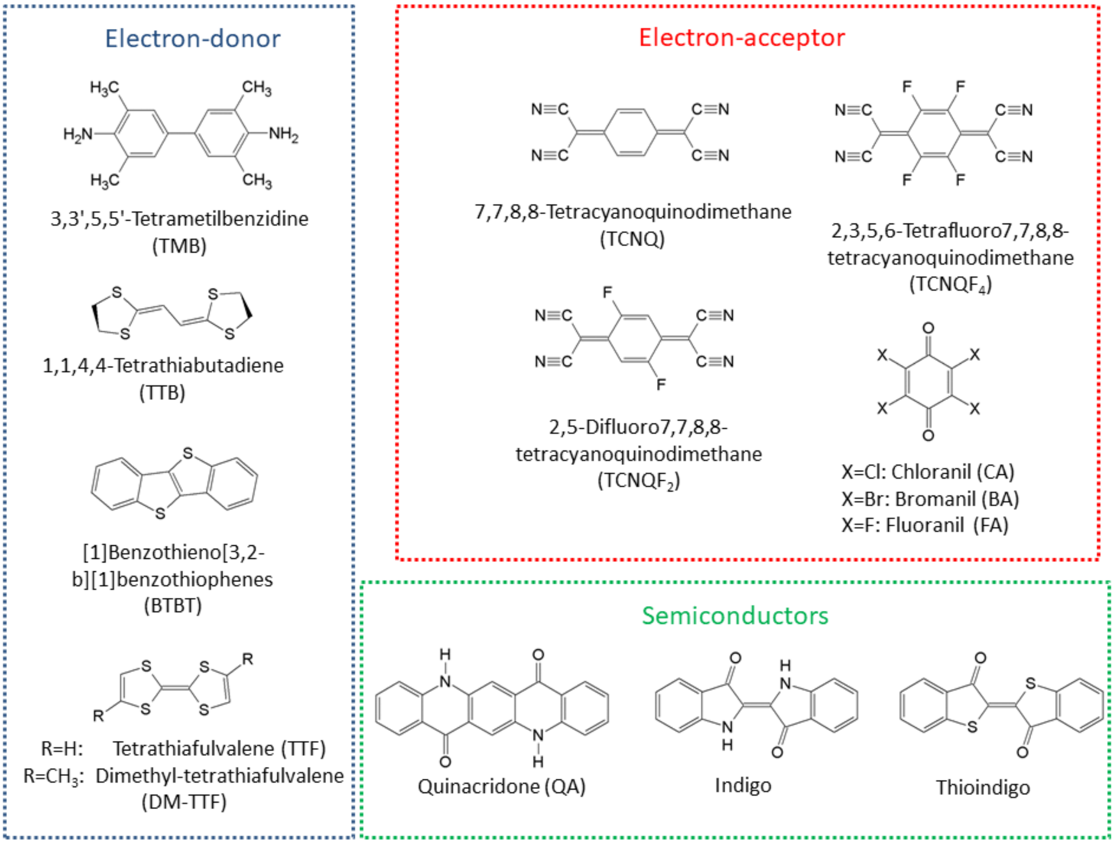

Figure 2: Chemical formula and related acronyms of the molecules considered in the present Thesis

One of the ideas to build bio-compatible semiconductors was to use ancient natural dyes, like thioindigo, indigo or quinacridone [8]. One of the problems with these materials is that, due to strong hydrogen bonding, most of them are hardly soluble in water or in organic solvents, so obtaining crystals or thin films is a difficult process. Moreover, like many other molecular semiconductors, they may grow in different polymorphs which may occur in a single crystallite, thus degrading performance [9]. Since the guest group had developed a simple spectroscopic method to detect different polymorphs [10], and since the problem of polymorphism (including the

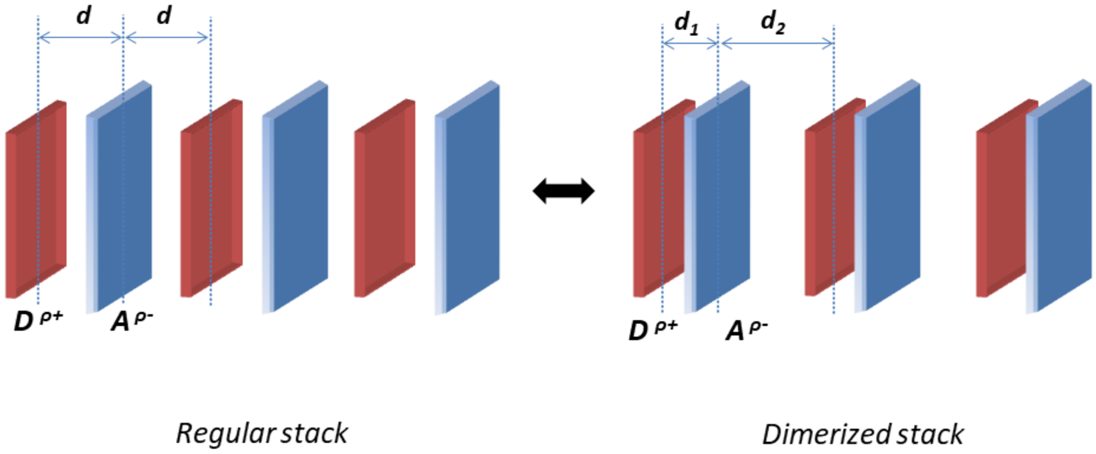

Figure 3: Sketch of a regular stack (left) and a dimerized stack (right)

identification of polymorphs) was particularly difficult in the case of quinacridone, this was the molecule we addressed our attention. Unfortunately, the problem of growing quidacridone crystals or films turned out to be a formidable one, and only a preliminary study could be accomplished before the end of the Thesis period. This part is reported in the last Chapter.

Most of the work of this Thesis has been devoted to [1:1] mixed stack CT crystals. These crystals are made up by an electron-donor (D) and acceptor (A) π-conjugated molecule. The strongly dimensional CT interaction between the D/A frontier orbitals dominates over the other intermolecular interactions and yields the formation of one-dimensional stacks, (see Fig.3) with sizeable overlap between frontier orbitals. We then have delocalized electrons along the stack. while different stacks interact mainly via electrostatic interactions. The charge delocalization and the inequivalence of D and A sites cause a CT between D and A. The resulting stack can be described as $\mathrm{D}^{+\rho}\mathrm{A}^{-\rho}\ \mathrm{D}^{+\rho}\mathrm{A}^{-\rho}$ where ρ, the degree of CT or ionicity, is the average charge on the molecular sites. The degree of CT is determined by the competition between two energies: $(I_\mathrm{D} - A_\mathrm{A})$, the cost of ionizing a donor-acceptor (D-A) pair (I_D is the ionization potential of the donor and A_A is the acceptor electron affinity), and M, the electrostatic Madelung energy gained if the lattice is ionic. The ground state of the crystal is neutral if $(I_\mathrm{D} - A_\mathrm{A}) > M$, and ionic if $(I_\mathrm{D} - A_\mathrm{A}) < M$. If one neglects the CT or hopping integral t between D and A molecules, the crystal can be either completely neutral, $\rho = 0$, or completely ionic, $\rho = 1$. A finite value of t mixes these two states and makes possible the existence of intermediate value of the molecular charge, namely quasi-neutral (N, $\rho \lesssim 0.5$) or quasi-ionic (I, $\rho \gtrsim 0.5$) compounds.

The increase in pressure or the decrease in temperature increases the Madelung energy, and may induce the crossing of the $(I_\mathrm{D} - A_\mathrm{A}) = M$ borderline, with the passage of the ground state from N to I. The phase transition, named NIT (neutral ionic transition) was discovered in 1981 by J.B.Torrance *et al.* for tetrathiafulvalene-chloranil (TTF-CA) and other handful of CT crystals [11, 12]

Furthermore, on the ionic side the stack is instable due the Peierls mechanism, so that the transition is always accompanied by stack dimerization (see the right part of Fig.3) [13]. The interplay between correlated electrons and both inter- and intra-molecular phonons enhances the complexity of the system both in terms of the appearance of new phases and of amplification of materials responses [14].

From the perspective of materials research, several applicative aspects are being pursued, that span from the already cited ambipolar semiconductivity to ferroelectricity [15]. Since the above described phenomenology depends on the interplay of the different interactions involved, it is important to explore the phase space of mixed stack CT crystals to understand and ultimately control the factors determining the physical properties of interest. Such a task has been the main focus of the present Thesis.

Chapter 1

Crystal Growth

Crystal growth has been the first step in the present investigation, and indeed has occupied a considerable part of the work. Often obtaining good quality crystals is not an easy task, so that one has to do several attempts and try different methods.

Crystal growth is a process strongly based on personal experience, and everyone has his own favorite technique and procedures. Reproducibility is also an issue, as some parameters affecting crystallization may be not clear and difficult to control. Of course, there are general aspects and principles that must be taken into account together with the availability of different growth methods that can be adopted in specific conditions. It has also to be remarked that different kind of characterizations may require different constraints on the size of the sample. For example, a good X-ray crystal structure determination requires crystals of some tens/hundreds microns in the three dimensions, while for absorption measurement platelets of thickness less than the wavelength of the used radiation are needed for good spectrometric accuracy.

In this Chapter the principal methods of crystal growth employed in this thesis are described. They can be divided into two main categories: solution and vapor phase growth. Solution based methods are the most popular among chemists, due to the simplicity of their implementation, but suffer from the disadvantage of introducing a third component, the solvent, that can interfere with the growth. Vapor phase methods permit to bypass this problem providing a controlled atmosphere (vacuum or inert gas) in which the crystals are grown. In this chapter the different growth methods employed in this thesis will be first described. Then the growth of each considered crystal will be discussed in detail.

1.1 Solution methods

Organic molecules are typically soluble in common organic solvents over a range of temperatures and pressures. As a consequence it is possible to exploit solubility to grow single component or two components crystals (co-crystals). Few mg (in the order of units) of starting material are often enough for a single solution growth, so that different attempts even with few tents mg can be performed. For these reasons solution methods are often the first ones attempted.

1.1.1 Solvent evaporation

Solvent evaporation is the simplest and the most effective method. It involves the slow evaporation of the solvent from a saturated or nearly saturated solution containing the compound(s). Supersaturation can thus be reached and nuclei can form and grow into larger crystals (see Fig. 1.1 a)). The employed solvents are typically dichloromethane, chloroform, acetonitrile, and ethanol. In order to ensure slow evaporation, for instance in case the solvent is too volatile, it is useful to cover the sample with a holed cap. Another smart trick is to put the vial containing the evaporating solution into a larger beaker so that it remains inclined with respect to the vertical. This will encourage the crystals to grow on the lower side of the vial, since more solvent is in contact with the wall. Furthermore the angle prevents newly-formed crystals from falling straight to the bottom of the vial. Due to the narrowness of the vial, crystals on the walls are easier to remove.

1.1.2 Solvent layering

Layering can be tried when others solution methods fail. This method also is good for milligram amounts of materials which are sensitive to ambient laboratory conditions (air, moisture).

The technique is based on the slow diffusion of a solvent (S_2), in which the compound is insoluble, into another solvent S_1, in which the compound has been dissolved. While the solution becomes more rich in S_2 the solubility of the compound is decreased, so that supersaturation is reached and nucleation occurs.

In the more conventional version of this method, the solute is dissolved in the solvent (S_1) and placed in a test tube. Then a second solvent (S_2) is slowly dribbled into the tube so that S_1 and S_2 form discrete layers as sketched in Fig. 1.1 b). For the process to be successful, diffusion must be slow, so S_1 must have higher density than S_2, and the two solvent must be co-miscible. A critical point is the creation of the solvent layer. For this goal, a syringe is probably the best way to add the second solvent. Moreover, narrower is the tube, the easier it is to build up the layer. Five millimeter NMR tubes, one side sealed Pasteur pipette, or a 6-8 ml vial are good vessels to use for this crystal growth technique. CH_2Cl_2/Et_2O is a typical good solvent combination by trying this method (if the compound of interest is insoluble in ether).

In the case of co-crystals it is possible to use a variant of the previous method, named “reactant diffusion”. In this case solutions of the reactants (a solution of the donor and a solution of the acceptor in the case of a CT compound) are layered as described above, and allowed to slowly diffuse into one another. If the product of the reaction is insoluble, crystals of the product may form where the reactants mix.

1.1.3 Solution cooling

This method is suitable for compounds whose solubility in organic solvents is poor at room temperature but increases considerably at higher temperatures. The technique involves preparing a saturated solution at high temperature and then slowly cooling it. As the temperature decreases, the solvent ability to dissolve the solute decreases and a supersaturated environment is reached. In this condition nuclei form and, if the rate of cooling is slow enough, crystals grow (see Fig.1.2)). The entire range of

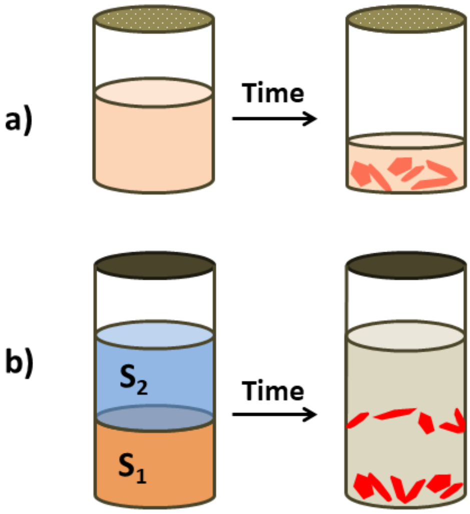

Figure 1.1: a) Slow solvent evaporation; b) solvent diffusion

temperatures at which the solvent remains liquid can be in principle used, so the solution is usually heated to just below the solvent boiling point and then slowly cooled down to room temperature and below with an available cooler/refrigerator. In order to obtain a slow rate of cooling it is important to cool the sample in a stepwise manner, hot ⟶ room temperature ⟶ 0°C or slightly below. It is also possible to use a Dewar flask and a water bath to minimize the rate of cooling. For this purpose the hot solution prepared in a capped tube is inserted in the Dewar containing hot water (just below the temperature of the solution). The Dewar flask is then left in a safe place until the solvent has cooled to room temperature and crystals have possibly formed. An other option is to use a programmable oven able to provide a uniform cooling rate over a pre-set time (see Fig. 1.2). In this case the hot solution in a closed tube is inserted in the oven already heated at the same temperature of the solution. Then the programmed cooling can start. This method should only be used when the compound is known to be thermally stable.

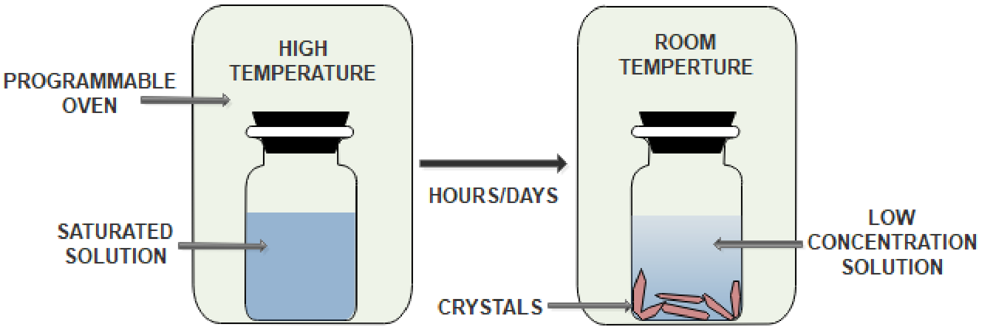

Figure 1.2: Sketch of the controlled slow cooling of a saturated solution in a programmable oven

1.2 Vapor phase methods

Most of the organic molecular materials have relatively low melting points and low sublimation temperatures, so that obtaining crystals from the vapor phase can be a convenient method. The physical vapor transport (PVT) allows to separate the organic compound from impurities, thus combining crystal growth with material purification. Since PVT occurs in the protected atmosphere provided by an inert gas and doesn't imply the use of a potentially interfering element like the solvent, it is considered the best method to obtain crystals of high purity [16, 17]. Several different PVT methods are frequently employed. Closed and open tube setup have been employed in this thesis and are described in the following subsections. It must also be noted that for binary CT compounds, two components (donor and acceptor) can sublime separately and react in a second moment to form the compound and finally crystallize. Since in this case also a chemical reaction is involved, the more general term "vapor phase method" (VPM) instead of PVT is probably more appropriate.

1.2.1 Closed tube system

In a closed system, the source materials are sealed by flame in a quartz or glass ampule under vacuum or inert gas conditions, and neither reactants nor products can escape from the ampule during crystal growth (see Fig.1.3a). The ampule is then inserted into a tubular furnace for the growth (see Fig.1.3b). The furnace is set to a proper temperature profile in order to have a higher temperature in the sublimation point, and a lower temperature in the deposition area, were crystallization is expected, as depicted in Fig.1.4. A furnace equipped with two heating zone is the ideal system to have a precise temperature profile, but also half of a single heating zone furnace can do the job. The typical temperature gradient is 5-10°cm^{-1}.

Due to the applied temperature gradient, buoyancy driven convection occurs in the closed tube. A quantitative study of the growth condition is beyond the aim of this thesis , nevertheless it is possible to have an idea of the magnitude of the convective motions thanks to a model based on a two dimensional closed tube (Handley cell) developed by Simpkins and Chen [18], according to which the velocity distribution is a cubic function of the depth. So that if the hot zone is on the left, velocity will be from left to right on the upper part of the ampule and reversed at the bottom (see Fig. 1.4). According to the model, the maximum velocity u^* results to be:

$$u^* \cong 3 \times 10^{-2} R/LC$$

and is located in between the ampule axis and the upper or lower wall. In the equation, L is the aspect ratio, length for gradient/tube diameter and C is a constant (approximately unity), while R is the Rayleigh number given by:

$$R = \frac{g\beta \Delta T d^3}{vk}$$

where g is the gravitational constant, β is the thermal expansion coefficient, k is the thermal diffusivity, d is the tube diameter and ΔT is the temperature difference across the region of steepest gradient. The R value for the carrier gases of interest,

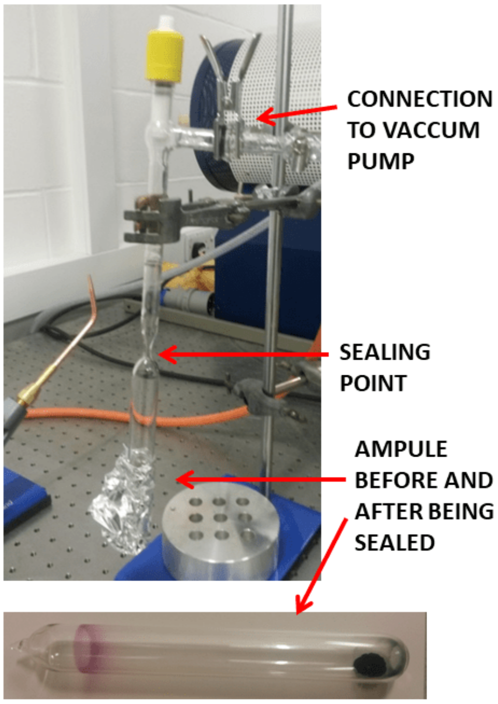

(a) Ampule charged with organic compound and connected to vacuum pump before being sealed (top); ampule ready for growth (bottom).

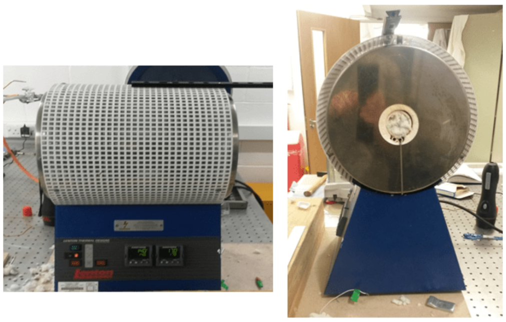

(b) Tubular furnace used for the growth).

Figure 1.3

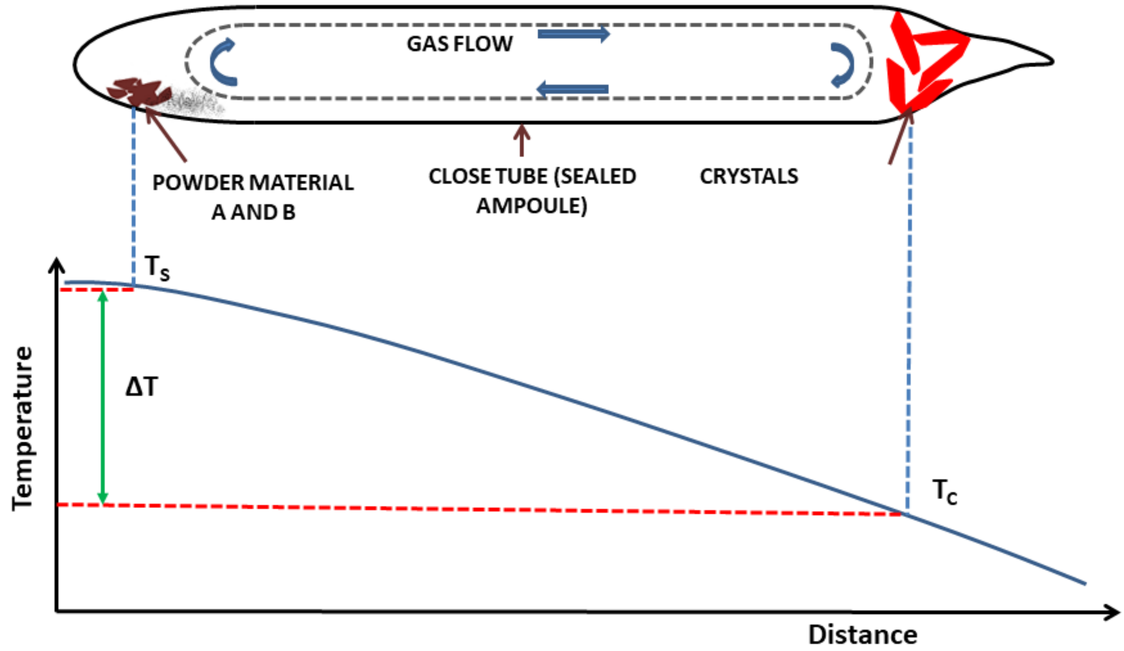

Figure 1.4: Sketch of the closed tube set-up (sealed ampule)

i.e. argon, helium and nitrogen, is $R = 51800$, 1120 and 64660, respectively. The corresponding maximum velocities are therefore about 14, 1.6 and 12 cm/s. From the experimental point of view the best quality crystals are obtained when the gradient temperature is kept as low as possible, and evaporation temperature are chosen typically to be some tens degree lower than material melting point. It must be noted that in the closed system possible impurities can deposit together with the crystals and even when high purity materials are used as source, some novel compounds may still form because of decomposition, photo-reaction, polymerization, or chemical reactions that occur during the crystal growth process.

1.2.2 Open tube system

In the open tube configuration a cylindrical quartz tube open at both ends is used as reactor instead of the sealed ampoule. A sketch of the system is shown in Fig.1.5. An inert gas flow is applied to the system in the direction of the decreasing temperature profile. The gas flow acts as transport agent during the crystal growth and influences the velocity of the vapor transport. Thus the contribution of the so called "forced convection", is added to the overall velocity together with the "buoyancy driven convection", the latter being the only one present in the case of the previously described closed tube configuration.

Thanks to the open reactor and the gas transport, the desired crystals and impurities are deposited in separated positions along the tube axis beacuse of their different molecular weights. The open tube also allows to put different reactants in different positions. This results particularly useful in the case of binary compounds such as CT materials. Often donor and acceptor materials have significantly different melting points, resulting usually in a marked difference in the vapour pressure at the same temperature. The material with higher melting point is therefore put at higher temperature, while the other material can be put at lower temperature, for example a distance of 6 cm corresponds to $\Delta T \cong 40$ ℃. Starting materials are put in small bowls and then moved at the proper positions. Due to the mild growth conditions used for organic materials (often not beyond 200 ℃), also glass can be used to contain the reactants. The part of a Pasteur pipette sealed at a thinner part can be successfully used (see Fig.1.6).

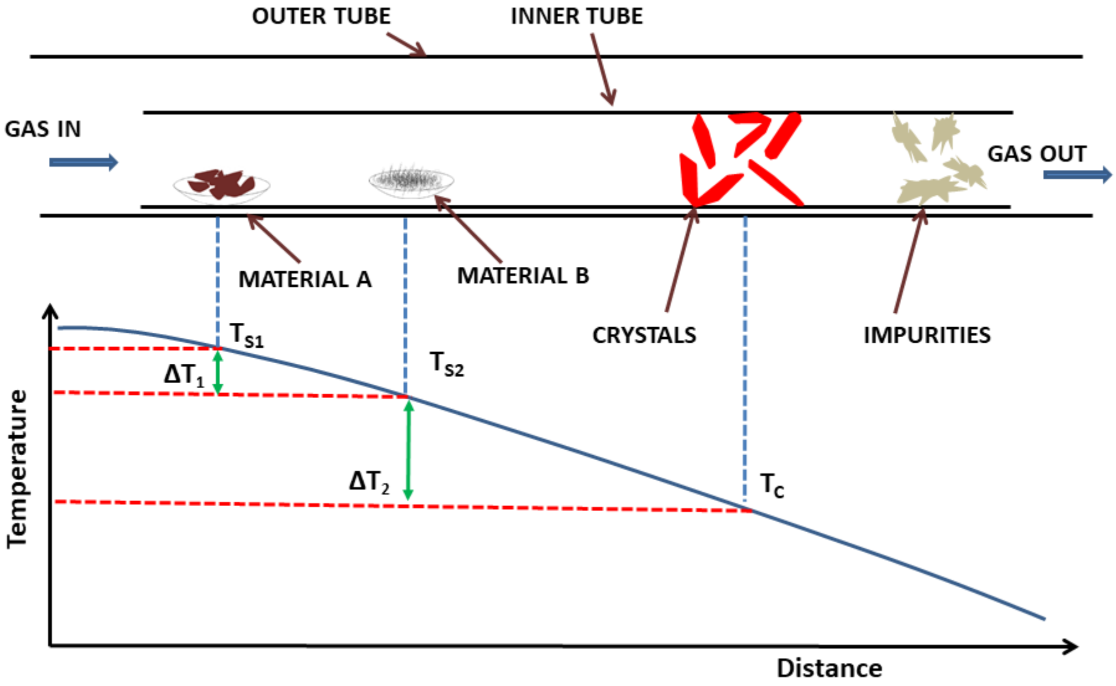

Figure 1.5: Sketch of the open tube set-up

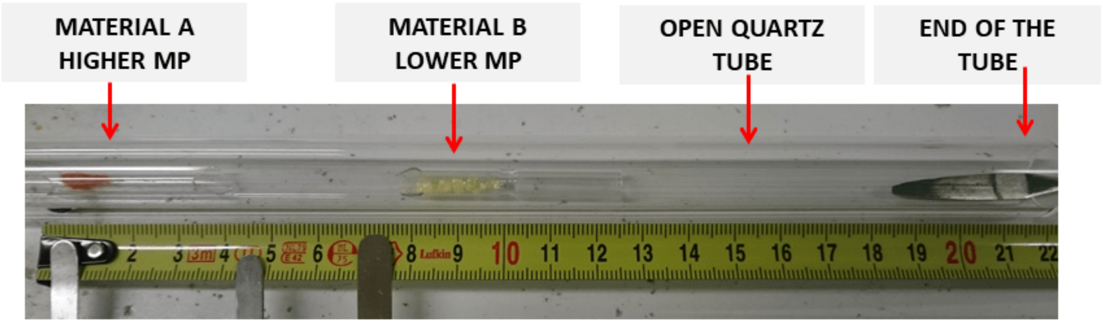

Figure 1.6: Photo of the open tube used as inner tube for crystallization in the present work. Material A and B are positioned in different points according to their melting points (vapor pressure)

The growth system utilized in this thesis is inspired to the one described by Laudise *et al.* [17] for the growth of organic semiconductors. In that case buoyant driven convection is considered to be dominant over the forced convection (2 order of magnitude greater). It is possible to understand the probable circulation pattern by referring to the idealized circulation pattern for a closed ampule described in Subsection 1.2.1. This circulation pattern can be used to understand the buoyancy driven component of circulation even in an apparatus where the tube is open at the ends. In this case the buoyancy cell is expected to reverse where the temperature gradient decays significantly, probably only a little to the right of the crystal deposition region. In other words since the velocity profile of the gas flow broadens as it proceeds downstream, the forced convection velocity is not significant in an apparatus with the dimensions of the one employed for this thesis. For such an apparatus the approximate overall velocity in a particular point of the tube is the sum of the buoyancy and forced convection velocities. Thus, even for the case of an open tube, counter-flux due to the buoyancy effect appears to be still present and prevalent.

Our growth apparatus can be seen as a simplified version of the one described by Laudise *et al.* [17] for several reasons. First of all, a furnace with only one heating zone was employed. Second, there was no precise control of the magnitude of the gas flow rate. This was empirically regulated by checking the number of bubbles per second produced by the gas coming out from the tube and entering a bubble trap. The flow rate empirically estimated in this way was kept as low as possible ($\cong 0.25$ bubbles/sec) in order to be closer to the case of a steady controlled gas atmosphere. Third, the external reactor tube was larger (3 cm diameter), so that the velocity profile broadening is supposed more marked. It is so possible to hypothesize that even in our system, buoyant driven convection dominate over forced convection, as in the system by Laudise *et al.* [17] or perhaps even in a more significant way. However, even with this simplified system it has been possible to obtain very good quality CT crystals, both for optical and structural analysis.

1.3 Details on individual crystal growths

1.3.1 TMB-CA, TMB-BA

Single crystals suitable for both structural and spectroscopic characterization were obtained following the solvent evaporation method (see Subsection 1.1.1) using acetonitrile as solvent. In both cases solution of the binary compounds were prepared by mixing in a beaker two nearly saturated solution of each component in [1:1] stoichiometric proportion at 40 ℃. After leaving the obtained solution at 40 ℃ for a few minutes, the beaker was covered with a holed aluminum foil and let to evaporate slowly at room temperature. In the case of TMB-CA, since after two days the formation of many thin needle-shape crystals was observed, the solution was filtered collecting a first batch of crystals, and the filtered liquid was rescued and let evaporate again. After 5 days it was possible to observe some needle-shape crystals with size 2-5 × 0.1-0.5 mm. The first batch was found good for IR absorption characterization, while crystals of the second batch were used for XRD (see Fig. 1.7). In the case of TMB-BA crystals were collected trough filtration after one week. In the same batch, crystals suitable for each kind of characterization were found (see Fig. 1.8). By observing crystal at optical microscope with polarized light it is possible to appreciate the anisotropy of light absorption, resulting in change of the sample color.

1.3.2 TMB-FA

Many attempts to crystallize TMB-FA were performed and finally the best obtained crystals provided only the cell parameters and the structural class. No crystal were

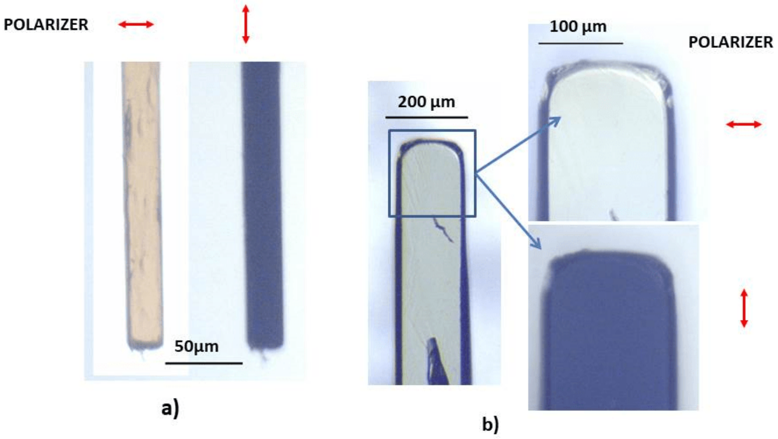

Figure 1.7: Microscopic images of TMB-CA samples. a) Polarized transmitted light perpendicular (left) and parallel (right) to the stack axis, of a sample from batch 1; b) Polarized reflected light perpendicular (top, right) and parallel (down, right) to the stack axis, of a sample from batch 2

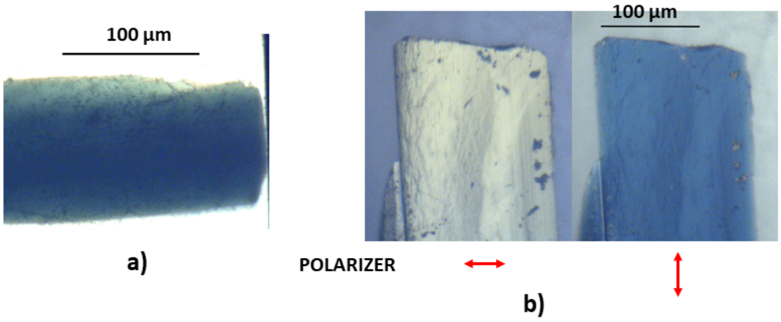

Figure 1.8: Microscopic images of TMB-BA samples. a)Transmitted light (left) to the stack axis, of a thin sample; b)Polarized reflected light perpendicular (left) and parallel (right) to the stack axis, of a thick sample

obtained by solvent evaporation, layering methods and controlled slow cooling. By slow evaporation in chlorinated solvents in dark condition and in inert gas atmosphere, small crystals were found. These crystals were to small for XRD, and optical characterization suggested the presence of at least two polymorphs. The best batch of crystals was obtained by cooling a hot solution (30°C) of TMB-FA in acetonitril close to saturation, directly in the refrigerator (-19°C). Even in this batch the presence of more polymorphs could not be excluded. The acquired structural data and a comment on IR characterization will be reported in Section 3.2).

1.3.3 BTBT-TCNQF$_X$ series

All the components of the family BTBT-TCNQF$_X$ (where X=0,2,4) were crystallized from solution trough a cooling process controlled by a programmable oven (see Subsection 1.1.3). 2 mg of BTBT were dissolved in dichlorobenzene (DCB) with the proper amount of TCNQF$_x$ to form an equimolar solution. The solutions were heated up to 90 ℃ and the total volume of DCB was determined in such a way to have saturated starting solutions. Each solution was then inserted in a programmable oven that was set up to decrease the temperature from 90 to 24 ℃ in 48h. Single

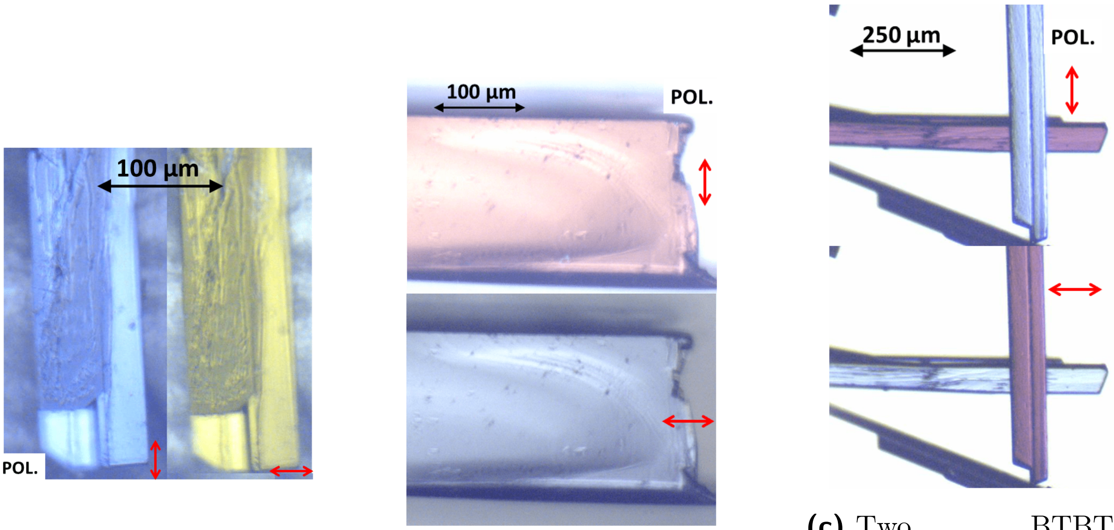

(a) BTBT-TCNQ single crystal images with reflected polarized light parallel (left) and perpendicular to the stack axis (right)

(b) BTBT-TCNQF$_2$ single crystal images with reflected polarized light parallel (top) and perpendicular (bottom) to the stack axis)

(c) Two BTBT-TCNQF$_4$ single crystals almost perpendicular to each other in reflected light. Anisotropy of light absorption can be appreciated with two perpendicular polarization of light.

Figure 1.9

crystals of good quality for all kind of crystallization were found for each compound. Example of crystals are reported in Fig.1.9a, 1.9b, 1.9c.

1.3.4 TMB-TCNQ

Obtaining good crystals of TMB-TCNQ was not a trivial task. As will be seen in details in Chapter 2, the availability of crystals suitable for a given characterization, in particular the low temperature phase structural determination, influenced the evolution of the experimental activity and the complete understanding of the material properties.

A first batch of good crystals was obtained from solution by following the reactants diffusion method (see Susbsection 1.1.2).

A 5 ml TMB saturated solution in isopropilic alcohol was layered onto a 5 ml TCNQ saturated solution in dichlorobenzene-chloroform [1:1], in a 10 ml closed tube. The alcoholic TMB solution, standing on the more dense and viscous TCNQ solution, promotes slow diffusion of the solutes at the interface, yielding the formation of crystals. After 3 days it was possible to observe needle-shaped crystals of millimeter size at the interface between the two liquids. After 1 week the solution was filtered and crystals were dried and collected (see Fig.1.10a)). They typically show the following features: needle-shape, twinned structure and low thickness. The twinned structure, together with transparency, and anisotropic light absorption of the crystals can be observed in the images with transmitted light reported in Fig.1.10b). These crystals were found suitable for absorption measurement.

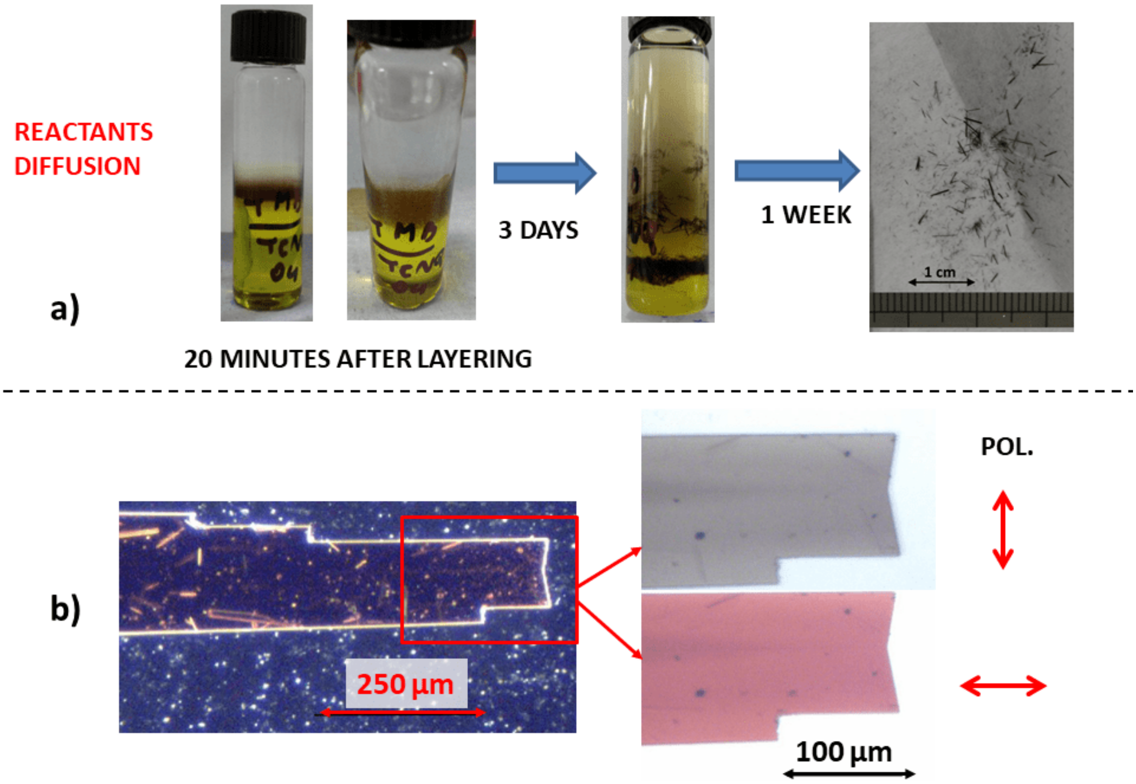

Figure 1.10: a) Evolution of the reactants diffusion crystallization after the layering of the two starting solution; b)A typical TMB-TCNQ twinned crystal observed with transmitted light (left); A part of the same crystal observed with transmitted polarized light perpendicular to the stack axis (right, up) and parallel (right, down)

A second batch of crystals was obtained by the closed tube VPM described in Subsection 1.2.1. Here, powders of the starting materials TMB and TCNQ were put in a clean glass ampule. The ampule was sealed by flame while being kept under low vacuum, $\cong 10^{-3}$ mbar (rotative pump). Then the ampule was inserted into a two-heating-zone tubular furnace for growth. The furnace was set to a proper temperature profile, i.e. around 195 ℃ at the source and around 160 ℃ in the colder deposition area. The ampule was kept at this temperature for one week, and formation of needle-shaped crystals was observed in the cold area. The needle-shaped crystals grown by vapor phase are of good quality, with well-formed surfaces. These crystals were found suitable for structural analysis at room temperature, for Raman measurement, and for IR reflectance and absorption measurements. Some images of the crystals are reported in Fig.1.11a).

The third batch of crystals was the result of a sublimation process in an open tube apparatus with controlled nitrogen flux (see Subsection 1.2.2). A tubular furnace equipped with a single heating zone was used for the growth. A proper temperature profile was provided by simply selecting the the maximum temperature measured at the center of the furnace. Reactants (20 mg TCNQ and 20 mg TMB) were put in glassy bowls an positioned in different points along the inner tube as in the situation depicted in Fig. 1.6. Position were chosen in order to have a temperature of $\cong$ 190

℃ for TCNQ, while the TMB bowl was shifted by ≅6cm in the direction of the gas flux, so that the temperature was about ≅ 155 ℃ . The inner tube was then inserted in the outer tube, in turn connected with the inert gas line (in and out). Finally the outer tube was placed in the furnace and connected to the gas flux. Then the furnace was switched on and brought to the growth temperature. The process was stopped after 40 h and the extracted quartz tube is shown in Fig.1.11b). All the starting material was evaporated. With this method it was finally possible to obtain very good quality needle-shaped crystals up to several mm size. Also very thin and transparent crystals were found. Microscopic images of some samples registered with reflected and transmitted polarized light are reported in Fig.1.11b). With these samples it was possible to characterize the low temperature phase of this material, as discussed in Chapter 2. For each batch, the room temperature crystal structure is the same, and coincides with that reported by Iwasa *et al.*[19].

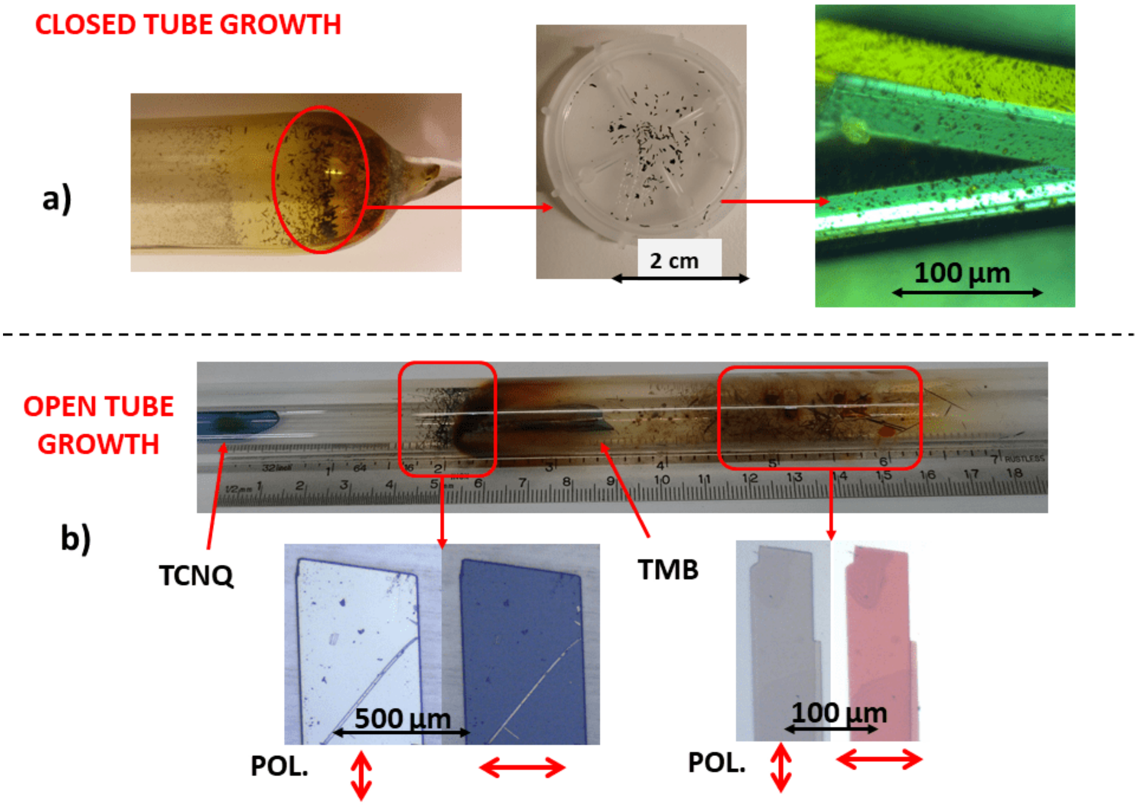

Figure 1.11: a) From left to right: crystals of TMB-TCNQ inside the sealed ampule just extracted extracted; crystals extracted from the ampule; microscopic images of a sample. b) Top: Open tube just extracted from the furnace after growth. Bottom: Images of sample collected in different positions. Images are obtained with polarized reflected light (left) and polarized transmitted light (right).

1.3.5 TMB-TCNQF$_2$, TMB-TCNQF$_4$

Growth of TMB-TCNQF$_2$, TMB-TCNQF$_4$ crystals was carried out by open tube VPM (see Subsection 1.2.2) following the same procedure used for TMB-TCNQ.

Starting powder of TMB and, $TCNQF_2$ or $TCNQF_4$ respectively, were located in the same position as TMB and TCNQ. Thus TMB was kept at the same distance of 6 cm to $TCNQF_X$. The maximum temperature was lowered by 10 ℃ so that TMB-$TCNQF_2$ and TMB-$TCNQF_4$ were expected to sublime at $\cong$ 180 ℃, to have a slower sublimation rate than in the case of TMB-TCNQ. After 48h the process was stopped. Crystals of TMB-$TCNQF_2$ are shown in Fig.1.12, in microscopic images with polarized transmitted and reflected light. Images of crystals of TMB-$TCNQF_4$ together with the open tube just extracted from the furnace are reported in Fig.1.13.

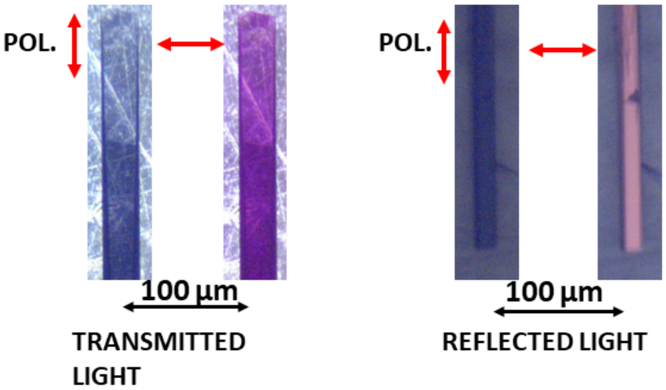

Figure 1.12: Images of TMB-$TCNQF_2$ crystals obtained by PVT, observed with polarized transmitted light (left), and polarized reflected light (right)

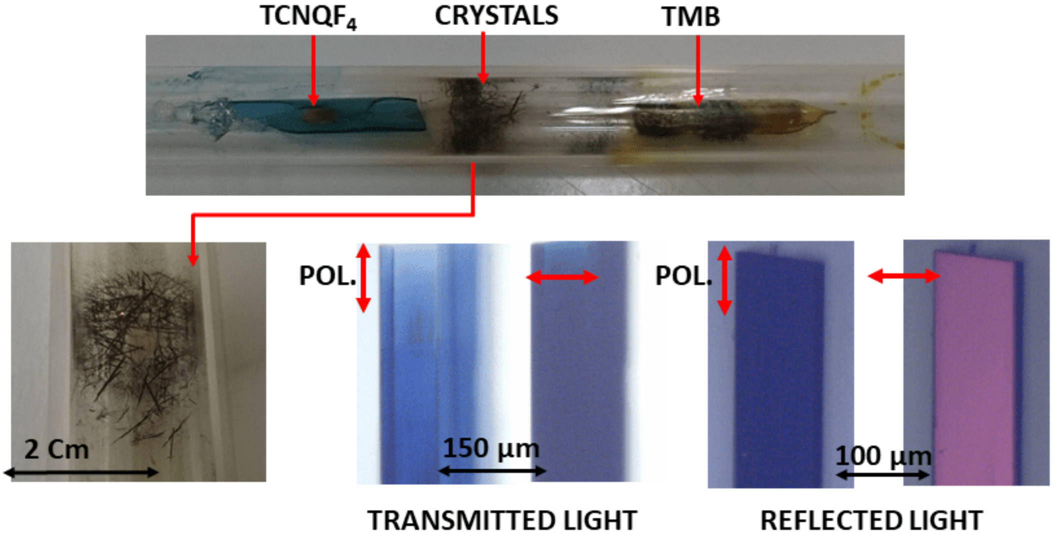

Figure 1.13: Top: Open tube extracted from the furnace just after the growth of TMB-$TCNQF_4$; Down, from left to right: zoom on crystals inside the tube, images of crystals observed with polarized transmitted light, and reflected light

1.3.6 Quinacridone

Since it is known that quinacridone (QA) can crystallize in different structures [20], as anticipated in the Introduction, many efforts were spent trying to crystallize the different polymorphs and to combine structural data with the relevant spectroscopic characterization. Collecting and characterizing the different polymorphs has turned out to be particularly complex, as is well expressed by the emblematic title of the first paragraph of the paper by Schmidt *et al.*: [20] *"Polymorphs of quinacridone: a real caos"*. Now it seems ascertained that at least four polymorphs can be isolated: α^I, α^{II} β and γ, phases. β [21, 20] and γ [20, 22, 23] phase are known and structurally well characterized since single crystals of good quality were obtained. α^I [24] α^{II} [25] phases were not obtained in form of single crystals. For α^I phase a predicted structure based on a starting powder diffraction pattern was provided by Schmidt *et al.* [20], while the nature of the α^{II} phase, obtained and analysed by the same authors remain, according to them, yet uncertain. All polymorphs of quinacridone are insoluble or almost insoluble in water and all other solvents, even at high temperatures. Such a behavior is due to the presence of numerous hydrogen bridges and very dense Van Der Waals packing, resulting in high lattice energies. For the same reason, like other organic pigments, quinacridone melting point (390°C) is remarkably higher than typical melting point of organic compounds.

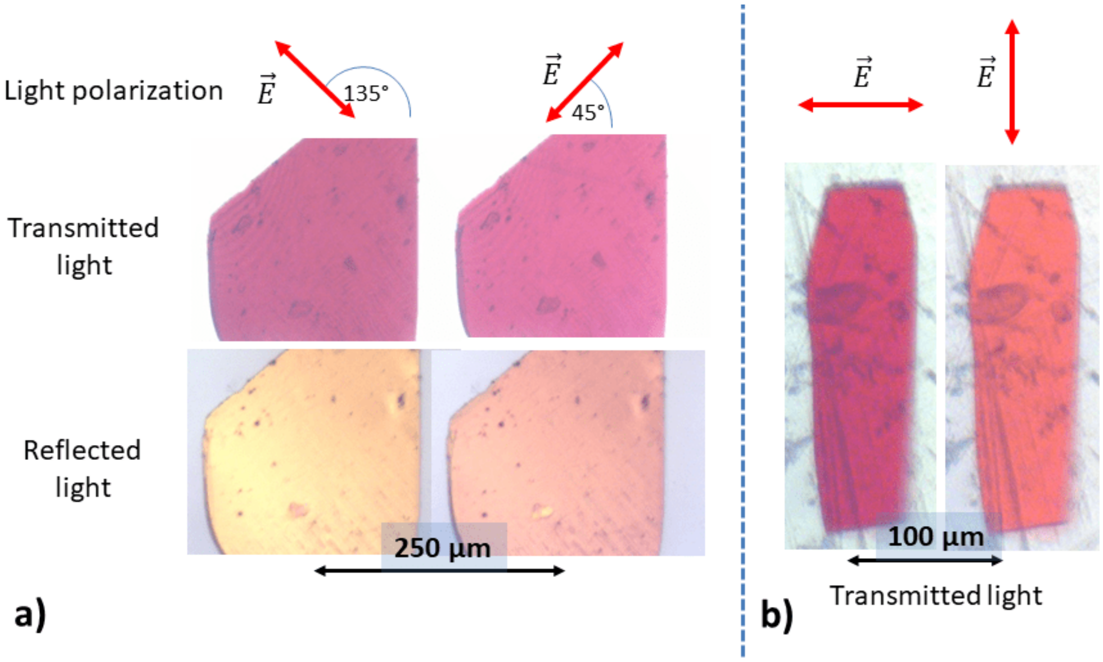

Figure 1.14: a) QA crystal grown by closed-tube PVT. (Top) Crystal seen with transmitted light and different polarizations; (Bottom) crystal seen with reflected light and different polarizations. b) QA crystal grown by open-tube PVT seen with transmitted light and two different polarizations.

Two methods have been employed to recrystallise quinacridone [20]: vacuum sublimation, and protonation, e.g. using concentrated sulphuric acid, with subsequent dilution or evaporation. With the first method β and γ-QA can be obtained sublimating QA powder at different temperatures (e.g. 200-250°C for β and 400°C for γ [21]), while the second method lead to (bad) crystals of the α^{II} phase. α^I is known to be obtained by a grinding process so that just powder can be obtained [20].

In this work, initially, the growth by protonation was tried in order to crystallize the α^{II} phase. Both fast dilution of a concentrated solution of quinacridone in sulphuric acid with water, and the slow dilution of such a solution with aqueous vapour, led to irregular growth of bad star-shape crystals, unfit for single crystal optical measurement. The attention was then switched to investigate the β and γ phases starting with vapour phase methods. Different crystals were obtained by different procedures and a tentative has been done, as PVT in a closed tube (see Subsection. 1.2.1) gave crystals assigned to the β phase. QA powder, acquired from TCI, were introduced in a glassy ampoule and sealed under low vacuum $\cong 10^{-3}$ mbar.The ampoule was later introduced in the fournace for the growth. Sublimation and deposition temperature were 340° and 300°C respectively and the growth was stopped after 6 days. Using the open-tube growth method (see Subsection 1.2.2) QA crystals, assigned to the γ phase, were obtained. For the process, QA powder were put in a quartz bowl and were then put in the reactor for the growth (the same apparatus used to grow TMB-TCNQ in Subsection 1.3.4). The sublimation temperature was 300°C and a constant nitrogen flux was applied. The growth was stopped after 80h. Extremely thin crystals were found in a colder region, corresponding to a crystal growth temperature ranging from $\approx$220 to $\approx$250°C. Images of samples for both growth are reported in Fig.1.14. Crystal of β-QA are thicker than γ-QA crystals, so that images in reflected light better show the change of color observed by changing the polarization of incident light. This is less evident by observation with transmitted light.

Chapter 2

A valence instability: TMB-TCNQ

TMB-TCNQ CT crystal is made up by the electron donor unit 3,3',5,5'-tetramethylbenzidine (TMB) and the electron acceptor-unit tetracyanoquinodimethane (TCNQ). According to the studies available in the literature, TMB-TCNQ undergoes a neutral-to-ionic (NIT) transition at $T \approx 200K$, with large hysteresis and with a change of the degree of CT (or ionicity) ρ of about 0.1 just around the N-I borderline citeiwasa90. A subsequent work showed that the crystals may break at the transition [26]. Despite the many similarities with the prototypical tetrathiafulvalene-chloranil (TTF-CA), and the convenient high temperature of the transition, no more investigation were performed. We therefore decided to re-investigate this system, in order to have a better understanding of the nature and the mechanism of the phase transition, and to try to characterize the low-temperature phase.

The availability of good quality crystals has played a key role in the investigation of TMB-TCNQ properties, and also affected the evolution of the experimental activity. In particular it was possible to collect good diffraction data of the low-temperature phase only after obtaining suitable crystals, and that happened after the first paper on TMB-TCNQ was accepted and published [27].

In a first attempt, TMB-TCNQ crystals were obtained both by precipitation from solution and by sublimation in a closed ampule. By mixing saturated solutions of the two component in hot acetonitrile, followed by slow cooling and solvent evaporation, we obtained crystals with a high degree of disorder, that could not be characterized by X-ray. These crystals did not show phase transitions down to 77 K, and likely belong to the early reported triclinic phase [28, 29]. The three batches actually used in the characterization has been obtained as described in Subsection 1.3.4. The X-ray diffraction data for the second batch were collected at the University of Bath, while the other batches were characterized at Parma. All the spectroscopic measurement have been made in Parma. The details are reported in the Appendix A.

2.1 Results

2.1.1 Room-temperature characterization

Our X-ray diffraction measurements, collected at 230 K, confirm the previously reported room temperature crystal structure [19]: monoclinic space group $P2_1/n$ (C_{2h}^5), with lattice constants a = 6.708(3) Å, b = 21.797(7) Å, c = 8.074(3) Å,

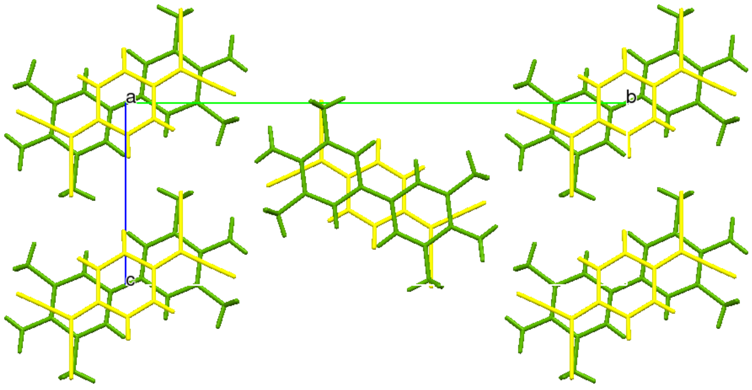

Figure 2.1: View of the TMB-TCNQ unit cell along the *a* stack axis. The TMB and TCNQ molecules are coloured in green and yellow, respectively, to put in evidence the overlap between the two molecular structures.

$\beta = 100.35(5)$, $Z = 2$ (R = 4.03). The TMB and TCNQ molecules reside on inversion centers and are stacked along the a axis, with 3.35 Å inter-planar distance. A projection of the unit cell along the stack axis is shown in Fig.2.1, putting in evidence the good overlap between the frontier orbitals of the two molecules that are depicted in Fig.2.2.

Also notice that the DADAD order of the two stacks in the unit cell is staggered, so that in the layers parallel to the bc planes each TCNQ molecule has four nearest neighbour TMB molecules and vice-versa.

The bond distances of TCNQ have been widely used to estimate the ionicity ρ in charge transfer crystals [30, 31]. The method essentially assumes a linear relationship between the ionicity and the ratio $\alpha = c/(b + d)$, where b, c and d are the TCNQ ring CC single bond, and the "wing" C=C and C-C bonds, respectively. From our structural data $\alpha = 0.4813$, and following the calibration in Ref. [31] we obtain $\rho = 0.25$, much lower than the early estimate from IR data [19].

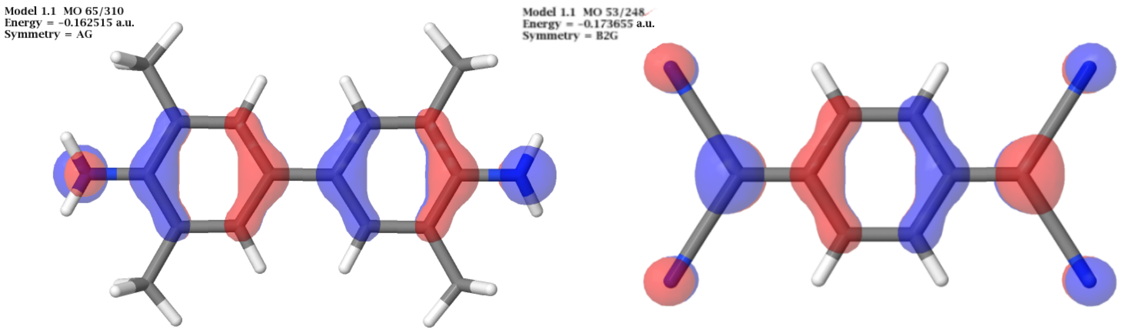

Figure 2.2: HOMO of TMB and LUMO of TCNQ.

In their optical characterization of TMB-TCNQ, Iwasa *et al.*[19] have reported the polarized reflectance spectra in the 2160-2230 cm^{-1} region, where the CN stretching vibrations occur, and the visible region, where the intra-molecular excitons are present. Here the polarized IR data are extended to the full mid-IR vibrational region, and the Raman spectra are also presented.

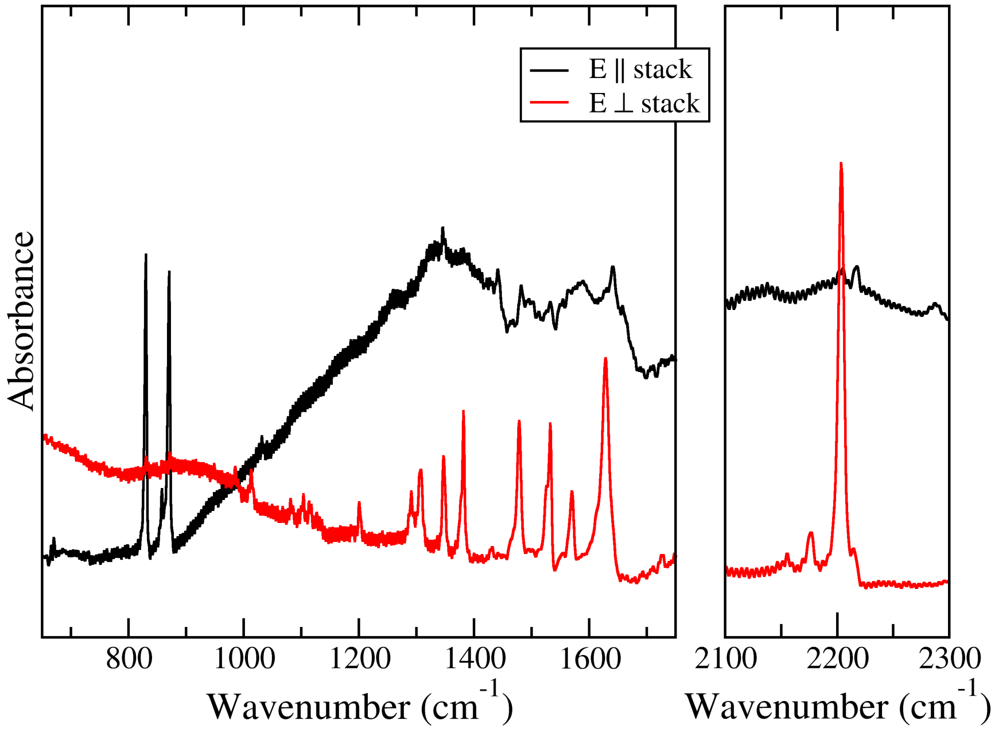

Figure 2.3: Polarized mid-IR spectra of TMB-TCNQ at room temperature. The different polarizations are offset for clarity.

The room temperature mid-IR polarized absorption spectra are reported in Fig.2.3. The examined plane contains the *a* stack axis and is likely the *ac* one. The spectra have been recorded with the electric field vector perpendicular to the stack (red curve in the Figure), showing the vibrational motions in the plane of the molecules, and with the electric field vector parallel to the stack (black line in the Figure), where the out-of-plane motions are detected.

The charge sensitive vibrations of TCNQ, namely the CN stretching $b_{1u}\nu_{19}$ and the C=C stretching $b_{1u}\nu_{20}$ [32], are clearly visible in the perpendicular spectra. It's remarkable that three absorptions are observed in the CN stretching region (right panel in Fig. 2.3), at 2204, 2176 and 2156 cm^{-1}, whereas only two are expected. The $b_{1u}\nu_{19}$ corresponds to the highest frequency, and gives $\rho = 0.49$, a value similar to that reported in Ref. [19] on the basis of reflectance spectra, but not consistent with the above estimate from structural data. On the other hand, it is well known that the TCNQ $b_{1u}\nu_{19}$ CN stretching frequency gives unreliable (generally overestimated) values of ρ since it suffers from uncertainty about the correct assignment, and is subject to extrinsic effects due to the interactions with the surrounding molecules [33, 34].

For this reason the investigation of the spectral range has been extended to the region where the $b_{1u}\nu_{20}$ C=C stretching occurs. The frequency of this mode indeed gives a much more reliable estimate of ρ. In the present case, the frequency is also easily identified, since it occurs in a spectral region (1550-1500 cm^{-1}) completely free from the absorptions of TMB unit. All the calculates frequencies of TMB and

TMB_+ are reported in Table B1 of appendix B. Fig.2.4 indeed illustrates how both the experimental infrared spectrum of neutral TMB powder and the calculated one trough DFT method of TMB^+, show a free window in the above mentioned spectral range. From this absorption, occurring at 1532 cm^{-1}, we obtain $\rho = 0.29$, a value quite consistent with the one estimated from the X-ray TCNQ bond lengths.

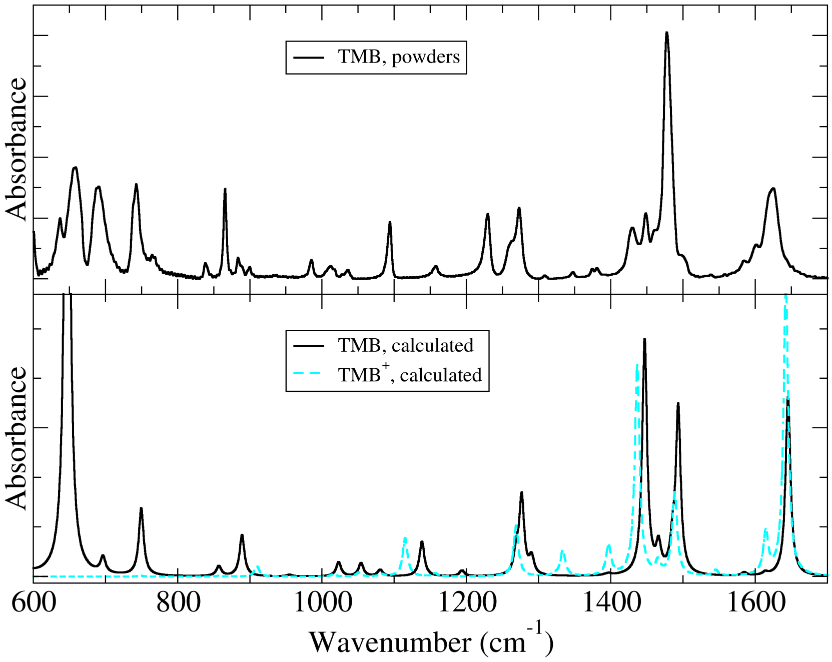

Figure 2.4: Comparison of the experimental infrared spectrum of neutral TMB powders (top panel) with the calculated one (bottom panel). The calculated spectrum of TMB^+ is also reported.

The out-of-plane modes are active in the parallel polarization (black curve in Fig.2.3) and indeed two bands, at 870 and 830 cm^{-1}, are clearly identified as due to the TMB $a_u\nu_{87}$ and TCNQ $b_{3u}\nu_{50}$ modes, respectively. Between 1000 and 1600 cm^{-1} the parallel spectrum presents a very broad band, with a strange shape. The increase of the baseline is due to the proximity of the onset of the very intense CT electronic transition, also polarized along the stack axis (see Section 3.4). On the other hand, the very strange and complex band-shape can be explained by considering that, as in TTF-CA [35], we are in the presence of combination modes between the Raman active totally symmetric intra-molecular modes and the low-frequency inter-molecular Peierls mode(s). All these modes are coupled together trough the CT electron. In TTF-CA, these modes could be identified, since the totally symmetric modes coupled to the CT electron are relatively few and isolated. In the present case between 1000 and 1600 cm^{-1} we have instead many strongly coupled totally symmetric modes, from both TMB and TCNQ, so that the combinations modes overlap and coalesce, giving rise to the strange band-shape.

Fig.2.5 reports the room temperature Raman spectrum of TMB-TCNQ in the spectral region of intra-molecular vibrations. Only one polarization is reported (electric vector of incident and scattered light perpendicular to the stack axis) as no additional information is provided by the other polarizations. The spectra are dominated by the TCNQ totally symmetric vibrations, as these have a very high Raman cross section. It is also remarkable that two bands of comparable intensity are present in the CN stretching region. Since the CN stretching of b_{3g} symmetry has an intensity much lower than that of the corresponding a_g mode [36], it is reasonable to attribute the doublet structure to the effect of different crystalline environments for the CN groups, as it is likely the case for the three bands observed in the IR.

The TCNQ $a_g\nu_4$ mode, located at 1454 cm^{-1} in neutral TCNQ [36], and exhibiting an ionization frequency shift Δ of 63 cm^{-1} [32], has been often used to estimate the ionicity of segregated stack CT crystals like TTF-TCNQ [37]. However, totally symmetric modes are coupled to the CT electron (e-mv interaction) [38], and in mixed stack crystals the linear dependence of their frequency from ρ is lost. Nevertheless, a rough estimate of ρ can be obtained by taking into account the perturbing effect of e-mv interaction through an appropriate model. For a regular chain like room temperature TMB-TCNQ we can use the trimer model, and by disregarding the interaction among e-mv coupled modes (isolated band approximation), the perturbed frequency Ω is given by [39]:

$$\Omega = \sqrt{(\omega_0 - \Delta\rho)\left[(\omega_0 - \Delta\rho) - \frac{4g^2}{\omega_{CT}}\rho(1-\rho)^2\right]} \tag{2.1}$$

where ω_0 is the vibrational frequency of the neutral molecule, Δ the ionization frequency shift, g the e-mv coupling constant and ω_{CT} is the frequency of the CT transition. In TMB-TCNQ the $a_g\nu_4$ mode occurs at 1418 cm^{-1}, ω_{CT} = 7560 cm^{-1}, and with a value of 65 meV for the e-mv coupling constant of the $a_g\nu_4$ mode [38], Eq. 2.1 gives $\rho \approx 0.4$. Being model dependent, this estimate is very approximate, and just gives a consistency check of the values obtained by other methods.

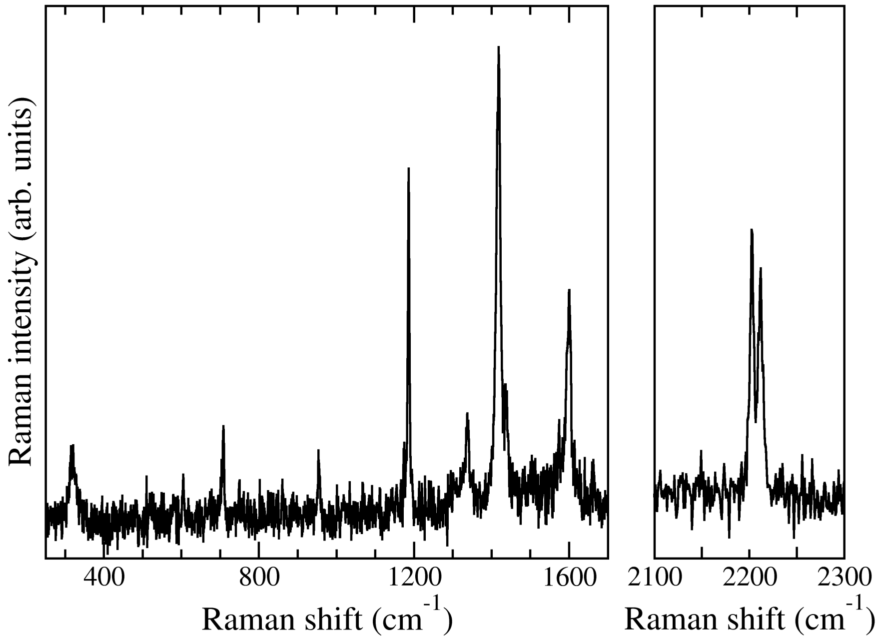

Figure 2.5: Raman spectrum of TMB-TCNQ at room temperature with electric vector of the incident and scattered light perpendicular to the stack axis.

To summarize, the X-ray bond distances and the charge sensitive vibrations (except for the unreliable CN stretching mode) all place room temperature TMB-TCNQ well on the neutral side, with ρ between 0.25 and 0.30. In the following we shall make reference to the value obtained from the $b_{1u}\nu_{20}$, $\rho = 0.29$, since we can use only this method to estimate the degree of charge transfer below the phase transition.

2.1.2 The phase transition

From the analysis of the previous Section, it turns out that at room temperature TMB-TCNQ is very similar to TTF-CA[40] or to Dimethyltetrathiafulvalene-Chloranil (DMTTF-CA)[41] just above the neutral-ionic phase transition: Ionicity not far from the N-I borderline, CT transition in the IR frequency range, and evidence of low-frequency Peierls(s) mode by the so-called IR “side-bands” in the parallel IR spectra.

As mentioned in Section 1.3.4 the two first batches of TMB-TCNQ allowed one to obtain structural information only for the room temperature phase, due to crystal breaking/damage at the phase transition. The whole spectroscopic characterization of the phase transition was possible also on these batches, because the crystal breaking during the transition resulted in the formation of fragments still of a good size for micro-IR and micro-Raman analysis. We have first collected structural data at 150 K, well below the reported transition temperature of 205 K [19], but the refinement gave a $P2_1/n$ structure, the same as that collected at 230 K, although with a worse R factor (7.89). The extensive spectroscopic measurements we have collected show that the occurrence of the transition and its critical temperature are scarcely reproducible [26], particularly if the sample is embedded or put in contact with different substrates, e.g. a KBr window, Nujol mull, etc. The cooling rate does

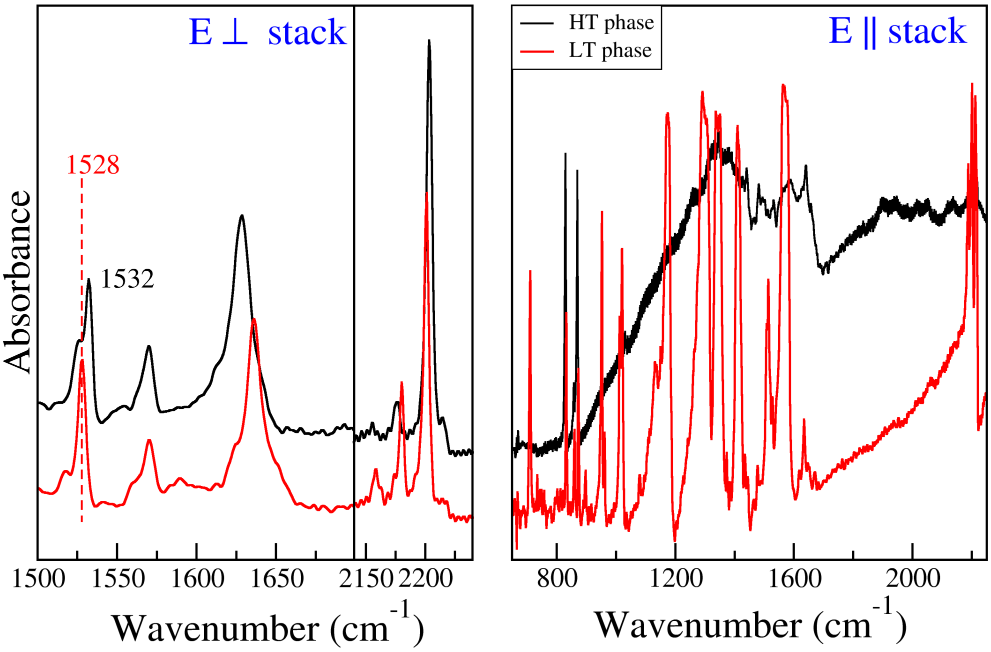

Figure 2.6: Infrared spectrum of TMB-TCNQ above (HT phase) and below (LT phase) the transition temperature.The spectra of the two phases are offset for clarity.

not seem to be important, and the sample often breaks at the transition [26]. In the case of X-ray, it was found that the grease used to hold the sample prevents the phase transition, although micro-crackings will worsen the refinement. Actually, the reported transition temperatures of $\approx$ 205 K on cooling and of $\approx$ 235 K on heating could be obtained only for "free" samples, for instance a crystal leaning on a glass slide. Also simple grinding of the crystal may prevent the transition down to 77 K.

In order to avoid confusion making reference to the critical temperatures, henceforth we will refer to the phases above and below the transition as high temperature (HT) and low-temperature (LT) phases, respectively. Fig. 2.6 compares the polarized IR absorption spectra above and below the phase transition in the spectral regions of interest. The spectra polarized perpendicular to the stack (left panel) shows that the charge sensitive bands shift very little with the transition. In particular, the $b_{1u}\nu_{20}$ C=C stretching moves from 1532 to 1528 cm^{-1}, which corresponds to a ρ increase of about 0.1, from 0.29 to 0.41. The absolute value of the ionicity is not reliably estimated from the CN stretching, but the relative change obtained from the frequency lowering is $\Delta\rho = 0.1$, as from the C=C stretching. Therefore TMB-TCNQ remains on the neutral side also in the LT phase. On the other hand, the appearance of very strong bands in the spectra polarized parallel to the stack (right side of Fig. 2.6) like in TTF-CA low temperature phase [13], unambiguously demonstrates that the stack dimerizes at the transition [38]. These bands are in fact associated to the e-mv coupled totally symmetric Raman active modes, which become IR active due to the loss of the inversion center and borrow intensity from the nearby CT transition. We notice that they are more numerous than those observed in the Raman spectra (Fig. 2.3 and Fig. 2.7 above). The reason is that, as we have already mentioned, the Raman spectra are dominated by the TCNQ bands, whereas the e-mv induced bands are due both to the TCNQ and TMB totally symmetric modes with appreciable values of the e-mv coupling constants. Fig. 2.7 shows that the frequency of the TCNQ $a_g\nu_4$ mode lowers by 7 cm^{-1} in going from the HT to the LT phase. As we have already mentioned, the estimate of ρ from Raman is very approximate in the present case. For the LT phase, the use of the dimer model[38, 39] with the further assumption of an unshifted CT band at the transition) gives practically the same $\rho \approx 0.4$ as the HT phase. The Raman data essentially confirm that the N-I borderline is not crossed at the transition.

Finally, Fig.2.8 compares the low-frequency Raman spectra of HT and LT phases. The lattice modes occurring in this spectral region are very sensitive to the crystal structure and packing [42]. In this case we present both the ($\perp\perp$) and ($\|\perp$) polarizations ($\perp$ and $\|$ with reference to the stack axis). In the examined *ac* plane of the HT phase, we expect three Raman totally symmetric lattice modes present in the two polarizations with possibly different intensities, and indeed we detect three bands, at 39, 51 and 69 cm^{-1}. In the LT phase a double number of bands is observed, at 35, 42, 50, 60, 79, and 128 cm^{-1}, clearly indicating a symmetry lowering of the unit cell. This finding is consistent with the above discussed appearance of e-mv induced bands in the LT phase IR spectra, which indicates the dimerization of the stack, i.e., the loss of the inversion center. A minimum loss of symmetry implies the passage from a C_{2h} factor group to a either a C_s group, like TTF-CA [43], or to a C_2 group.

To summarize the discussion up this point, the first order transition of TMB-TCNQ implies a change of ionicity $\Delta\rho \simeq 0.1$, from 0.29 to 0.41, and is accompanied

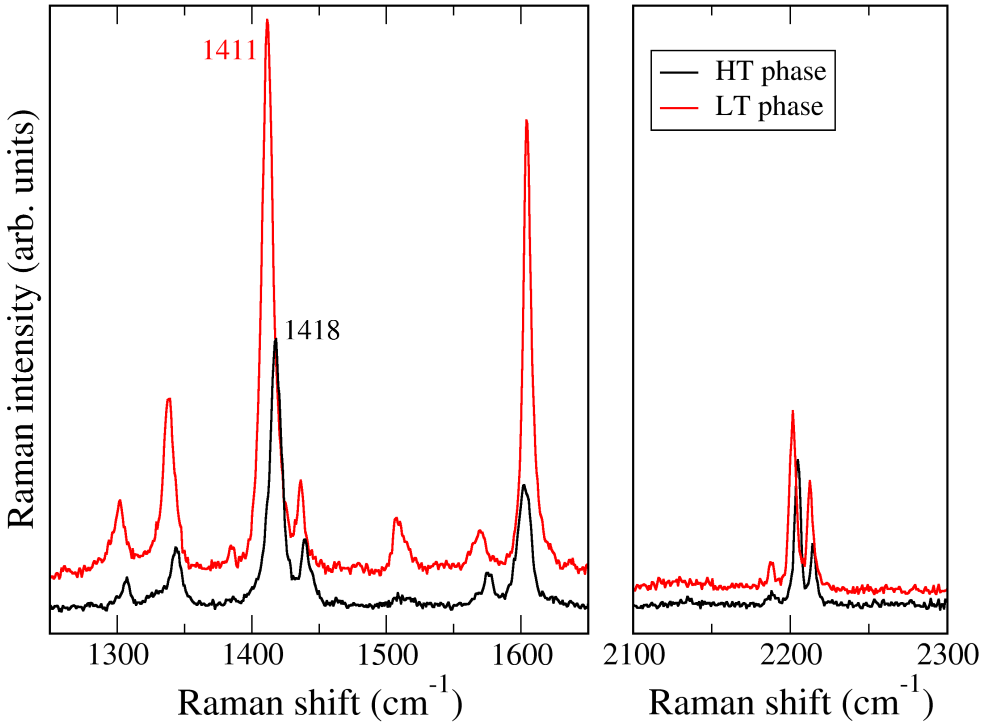

Figure 2.7: Raman spectrum of TMB-TCNQ above (HT phase) and below (LT phase) the transition temperature. The electric vector of the incident and scattered light is perpendicular to the stack axis. The spectra of the two phases are offset for clarity.

by a dimerization of the stack. Like in the case of DMTTF-CA [41], the phase transition can be hardly considered a "true" NIT, since the $\rho \simeq 0.5$ borderline is not crossed, but rather as a (small) valence instability. But in the present case we have a first order transition, like in TTF-CA, with crystal cracking or breaking and large hysteresis, whereas for DMTTF-CA the transition is practically continuous. From this point of view, the TMB-TCNQ transition appears to be different from the other known transitions of 1:1 mixed stack CT crystals. It must finally be noted that even if the N-I borderline is not crossed, the TMB-TCNQ LT phase is potentially ferroelectric, since the stack is dimerized and with intermediate degree of charge transfer. Ferro-electricity will be observed if the two stacks in the unit cell present in-phase dimerization, like TTF-CA [43].

In a first moment the cracking of the sample and the lack of reproducibility prevented us to get structural information on the LT phase. We then tried a computational approach to get some hint about the type of interaction triggering the transition and the associated mechanism [27]. We adopted a computationally not demanding semi-empirical method, MOPAC16 with PM7 parametrization [44], that allows to optimize the cell and the molecular geometry, and that has widely tested and optimized for equilibrium geometries [44].

Starting from the experimental $P2_1/n$ structure at 230 K and considering 4 unit cells, the minimum potential equilibrium geometry at 0 K was reached after 668 cycles. All the unit cell symmetry was apparently lost in the minimum search, but the use of a symmetry-recognition program[45] actually showed that the structure deviates very little from the monoclinic $P2_1$ (C_2^2) space group. This structure showed

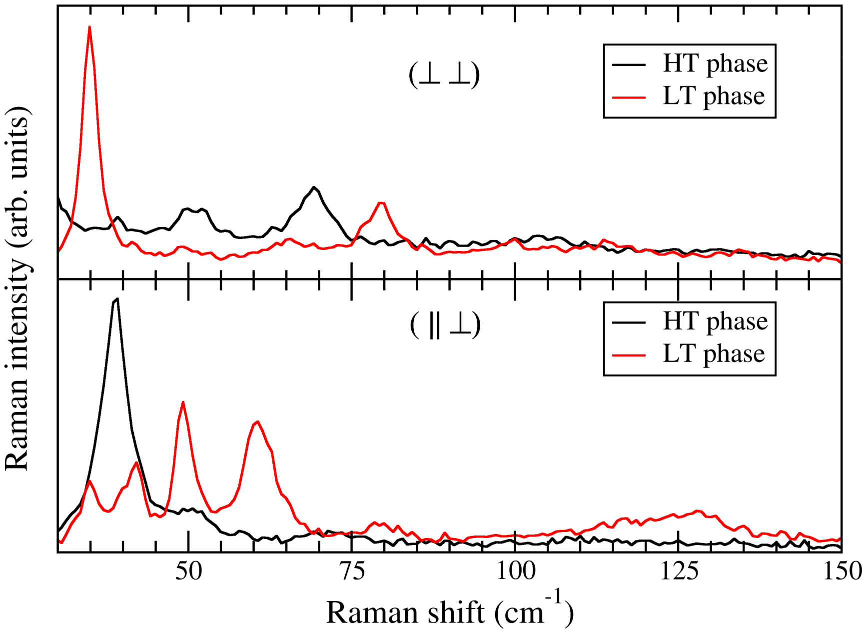

Figure 2.8: Low-frequency polarized Raman spectrum of TMB-TCNQ above (HT phase) and below (LT phase) the transition temperature. The ⊥ and ∥ symbols indicate the orientation of the electric vector of incident and scattered light with respect to the stack axis.

the loss of inversion centre together with a dimerization of the stack which is finally arranged with an antiferroelectric order. A slight increase in the cell volume is also observed. These results would be compatible with the spectroscopic evidences described above and with the tendency of the sample to break. Finally, the presence of inter-stack H-bonds in the hypothetical LT phase suggests their probable involvement of the transition.

2.1.3 Determination of the structure of the LT phase. Hysteresis.

Structural data of the LT phase were acquired only when the third batch of crystals, grown by PVT, was available. To overcome the problem related with the breaking of the crystal at the transition and the inhibition of the transition by enclosing fluids, the crystal was introduced into a glass capillary and blocked by pressing a capillary of smaller diameter at its bottom. It has been foud that the LT phase structure belongs to the monoclinic Pn (C_s^1) space group, hence both the inversion center and the screw axis of the HT phase are lost. The lattice parameters are reported in Table 2.1 together with the one of the HT phase. The most significant structural variations coming to light after the transition can be appreciated in Fig.2.9 and Fig.2.10, where the packing of the HT and LT phases viewed along different directions are reported. By comparison with the HT structure, no relevant variation of the bond distances is detected, while a slight distortion of the TMB molecule is present, with the benzene rings passing from a planar geometry to a twisted configuration with torsion angle 8.1°. The major changes observed involve the crystal stacking, that turns from a centrosymmetric scheme with a regular stack, to a dimerized one, as found from the

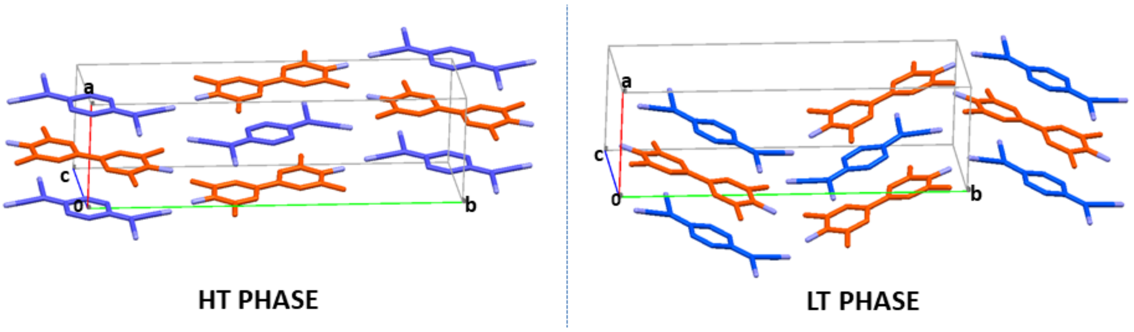

Figure 2.9: Comparison of the crystal packing of TMB-TCNQ in the HT phase (left panel) and in the LT phase (right panel)

IR analysis presented in the previous Subsection.

Table 2.1: Experimental structural parameters of TMB-TCNQ HT and LT phases.

	HT phase	LT phase
Space Group	$P2_1/n$	Pn
a (Å)	6.708	6.886
b (Å)	21.797	20.647
c (Å)	8.074	8.232
β (deg)	100.35	97.437
Z	2	2
Cell volume (Å^3)	1161.3	1160.54
D–A distance (Å)	3.35	3.614, 3,207

At 130 K indeed the distance between the molecules stacked along a is not equivalent (3.354 Å in the RT structure) but gives rise to an alternate pattern in which each molecule is 3.207 Å and 3.614 Å apart from its first neighbours. The dimerization amplitude, $\delta = (d_2 - d_1)/(d2 + d_1) = 0.060$ is large, in comparison with that of the LT phase of TTF-CA ($\delta = 0.025$) [43]. It is then remarkable, as one can observe from Fig. 2.11, that the arrangement of the partially charged dimers inside the cell is ferroelectric. The two polar columns cross the bc plane of the cell and interact summing their dipole moments (right panel of Fig. 2.11) with the resulting dipole moment parallel to the a stack axis. This is, in principle, at the origin of a net dipole moment in the compound and consequently to pyro- or ferro-electric properties. Also related to the loss of the 2_1 screw axis is the molecular ordering pattern observed in the ab plane, involving the average planes of the molecules which form puckered sheets at an angle of 34.26° as one can observe in the bottom panels of Fig. 2.10a and Fig. 2.10b. This is the most evident change with respect to the HT phase, where all the molecules lie on planes perpendicular to the [100] direction. Finally, the projection on the bc plane does not show substantial differences, as both the structures are characterized by a checkerboard-like pattern of the TMB and TCNQ moieties whose bisecting lines form an angle of 61.1° and 55.0° in the HT and 130 K phases respectively (see the top panels of of Fig. 2.10a and Fig. 2.10b). No evident H-bonding is present in the structure. It is thus likely that π-π and H-π interactions drive the crystal packing, as a consequence the temperature-induced ionicity change may be at the origin of the puckering.

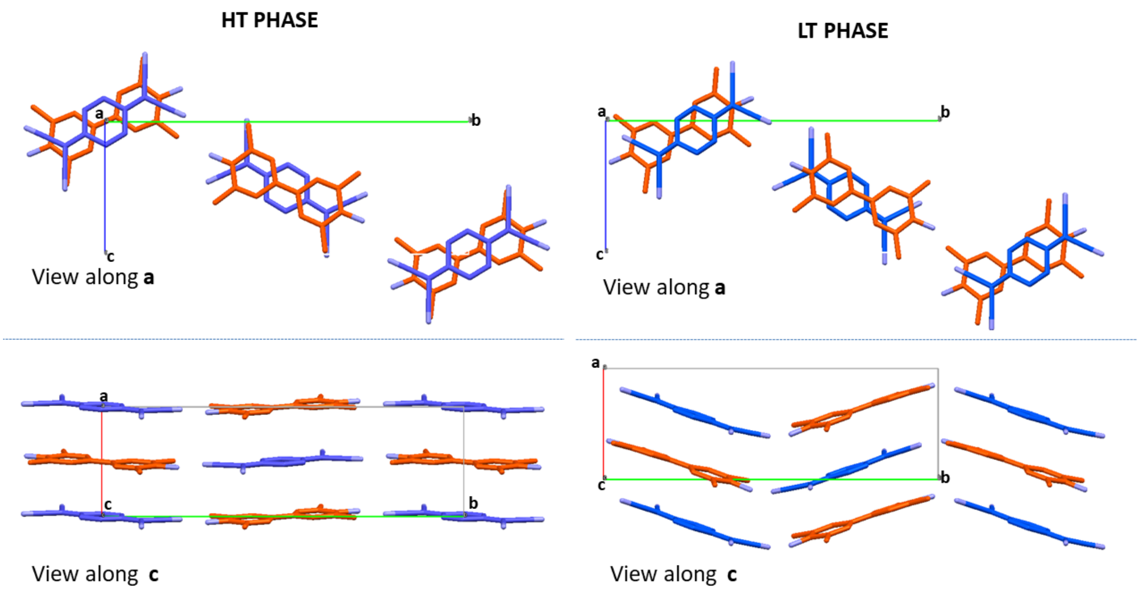

(a) Crystal packing of TMB-TCNQ in the HT phase viewed along different cristallographic directions: along *a* axis (top panel), along *c* axis (bottom panel).

(b) Crystal packing of TMB-TCNQ in the LT phase viewed along different cristallographic directions: along *a* axis (top panel), along *c* axis (bottom panel).

Figure 2.10

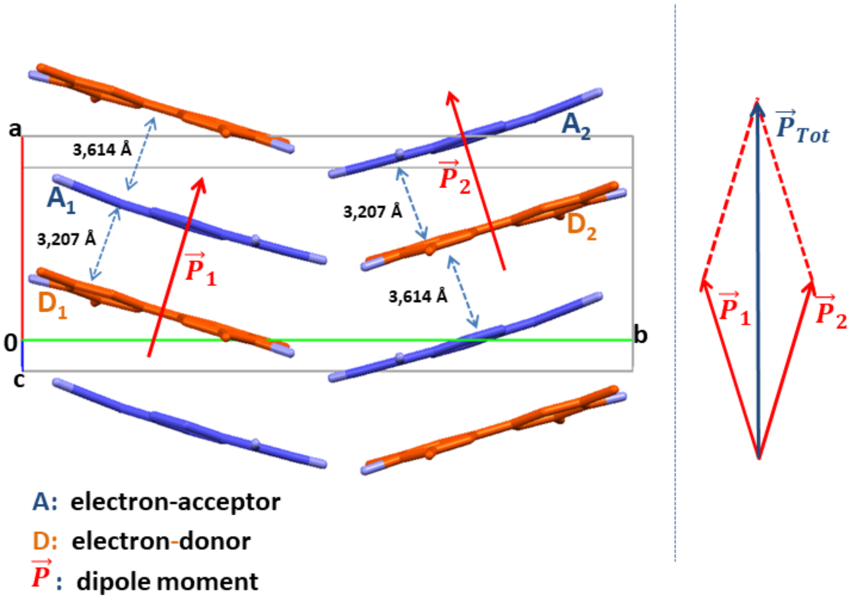

Figure 2.11: Crystal packing of TMB-TCNQ in the LT phase evidencing the dimerization of the stack and arrangement of the dipole moments within the cell (left panel). In the right panel the vectorial sum of the two dipole moments in the **ac** plane is represented.

The transition inducing the $P2_1/n$-Pn symmetry change is observed in cooling at about 160 K, however slight variability in the transition temperature is observed when different crystals are considered. This phenomenon may be related to the peculiar experimental setup, preventing the accurate determination of the temperature on the sample, or to the hysteretic nature of the process, so that the transition temperature likely depends on the initial state of the system. The lattice parameters refinement carried out at different temperatures clearly shows a discontinuous anomaly affecting a, b, c and β (see Fig. 2.12 and Fig. 2.13) and underlines a strong anisotropic character regarding the modification of such parametrs. On one hand indeed a and c increase at the transition of about 2%, on the other hand b diminishes of about 6%, as can be seen from Fig. 2.12. Such a behaviour can well explain the tendency of the crystals to break when the transition temperature is crossed, despite the volume jump is quite small: 1161.3-1160.5 Å^3 at RT and 130 K respectively, corresponding to a 0.07% variation. On heating the transition is observed at about 230 K, with an hysteresis of about 70 K. (see Fig. 2.12a). In this case

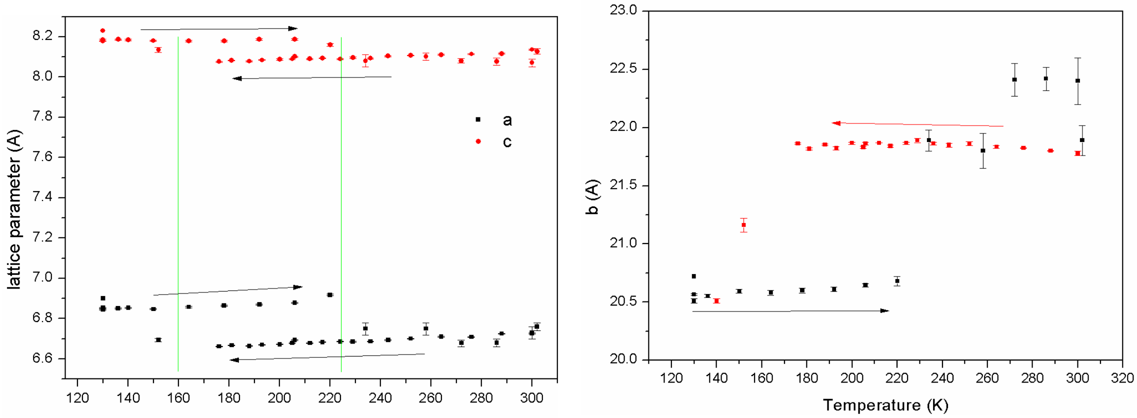

(a) Vector a (black dots); vector c (red dots)

(b) Vector b. Red dots:cooling; black dots: heating

Figure 2.12: Evolution of the cell parameters with the temperature

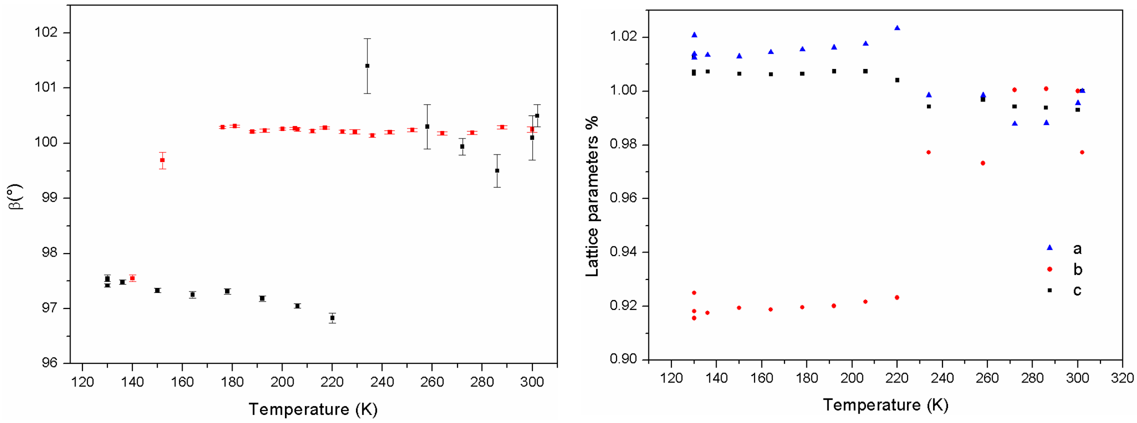

(a) Evolution of the β angle with temperature

(b) Evolution of the parameter with temperature, (percentage variation)

Figure 2.13: Evolution of the cell parameters with the temperature

severe cracking of the samples is observed, likely accompanied to microstructural damaging so that the data above the transition temperature are characterized by increased error bars. From the structural point of view however the initial structure is completely recovered, thus confirming the reversibility of the transition already verified by spectroscopic methods.

2.2 Conclusions

The accurate optical and structural study of TMB-TCNQ has shown that the first-order transition induced by the temperature is better classified as a valence instability rather than a true NIT, as the 0.1 ionicity jump does not lead to a crossing of the N-I borderline. The ionicity jump is accompanied by a strong stack dimerization, and the crystal generally breaks at the transition. The critical temperature identified trough spectroscopic observations, ($\approx$ 205 K on cooling and $\approx$ 235 K heating), appears to change when the sample is not completely free (e.g., adhesion to the KBr window in the IR measurements), and possibly depends also on the sample history. Critical temperature observed during structural measurement shows an even higher hysteresis: $\approx$ 160 K on cooling and $\approx$ 235 K heating. For these reasons the transition mechanism is difficult to study. However, the LT phase structure identification led to the conclusion that no significant H-bonds are formed, and that the transition is probably triggered by weak interactions. LT phase finally revealed a ferroelectric ordering, which is, to the best of our knowledge, the highest temperature for a transition to a ferroelectric state in organic CT crystals. As we have discussed above, the HT phase is very similar to that of TTF-CA or DMTTF-CA just before the transition [40, 41]. Yet by lowering the temperature the evolution of the three systems is different: TTF-CA undergoes a discontinuous NIT and DMTTF-CA displays an almost continuous ionicity change, accompanied by dimerization, but without crossing the N-I borderline. TMB-TCNQ instead has a first order transition with a discontinuous ionicity change, like TTF-CA, but again without crossing the N-I borderline. To give a rationale to these differences, one has to consider that by increasing the ionicity with lowering T, one reaches a multistability region [46], with a competition between a first order valence instability driven by the 3D Madelung energy and a second order one-dimensional Peierls instability. At this point very weak intermolecular forces, all connected to the compressibility of the sample, i.e. to the (anisotropic) increase of the Madelung energy, may trigger the transition and drive the system towards one of the possible minima. Such a kind of complex scenario explains why true temperature induced NIT are so rare, and why the actual type of phase transition occurring in mixed stack CT crystals is difficult to predict.

Chapter 3

TMB-Acceptor series

3.1 Introduction

3,3',5,5'-tetramethylbenzidine (TMB), the electron donor used in combination with TCNQ to form the CT crystal described in the previous Chapter, has also been coupled to other electron acceptors originating series of CT crystals having as common feature the same electron donor, TMB. The collection of such a group of systems is not casual, but is part of a project directed to explore the phase space of ms-CT crystals, i.e. to understand and ultimately control the factors determining the physical properties of interest. This kind of approach has recently started in the field of organic semiconductors, with the aim of engineering systems with different band gaps and degree of CT, in such a way to understand how these parameters affect the semiconducting behavior [31, 47, 34]. However, this systematic exploration has been so far limited to ms-CT crystals in the proximity of the neutral side ($0 \lesssim \rho \lesssim 0.2$) of the phase diagram, as a generally rather weak electron donor has been associated to acceptor of increasing electron affinity. Here we couple a relatively strong electron donor, TMB, with an extensive series of different electron acceptors, in such a way to span the ionicity from the neutral to the ionic side of the phase diagram. Evaluation of the most important phenomenological parameters entering the modified Hubbard model apt to describe and understand a large spectrum of experimental data [48] allows us to get insight into the factors determining the crystal packing and physical properties of the systems under investigation.

3.2 TMB-haloquinones

We have started by coupling TMB with haloquinones of increasing electron affinity, namely tetrafluoro-, tetrachloro- and tetrabromo-*p*-benzoquinone (FA, CA and BA, respectively). We had problems with the TMB-FA: despite several attempts, also by different methods (see Subsection 1.3.2), the crystals, when obtained, often contain impurities and/or are not stable, probably due to spontaneous sublimation of FA. We have been able to single out a small crystal for X-ray analysis, but we could only get the structural class [49] and the cell parameters, as reported in Table 3.1.

From the frequency of the antisymmetric C=O stretching (1670 cm^{-1} in the IR absorption spetrum) we deduce $\rho \simeq 0.18$ by assuming for FA a ionization frequency shift of 160 cm^{-1} analogous to that of CA and BA [50, 51]. However, the vibrational spectra also showed small but significant differences even between crystals of the

Table 3.1: Basic structural parameters of TMB-haloquinoes

	TMB-FA	TMB-CA	TMB-BA
Class	$C2/m,\ Z = 2(i)$	$C2/m,\ Z = 2(i)$	$C2/m,\ Z = 2(i)$
a(Å)	7.745(3)	20.507(10)	20.492(5)
b(Å)	14.511(6)	6.444(3)	6.5073(15)
c(Å)	20.492(5)	8.790(5)	9.063(2)
β (deg)	97.526(7)	111.144(9)	110.232(3)
V(Å^3)	984.837	1083.37	1133.96

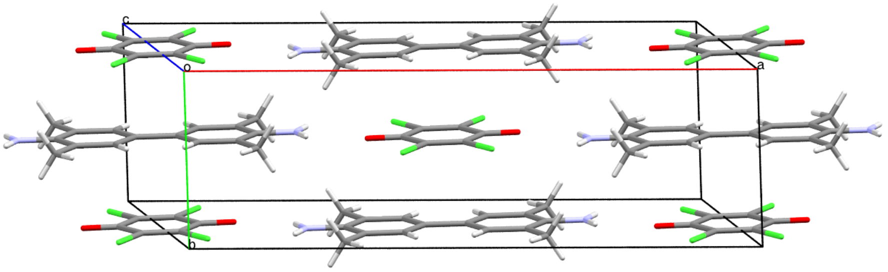

Figure 3.1: Crystal structure of the isomorphous TMB-CA and TMB-BA. Shown structure: TMB-CA.

same batch, indicating the probable presence of polymorphism and/or impurity contamination. For these reason we shall not discuss TMB-FA any further, focusing attention to the better characterized TMB-CA and TMB-BA.

TMB-CA and TMB-BA are isomorphous. They crystallize in the same class of TMB-FA (space group $C2/m,\ Z = 2$), but have a different packing, as clearly seen from Table 3.1. The TMB-CA packing is reported in Fig. 3.1. The molecules alternate along the b axis, with the molecular planes almost perpendicular to it, so that their distance is a half the axis length. Each molecule resides on inversion center, so that the interplanar distance is constant (regular stack). The TMB-BA interplanar distance is slightly higher than that of TMB-CA (3.25 vs. 3.22 Å) due to the bulkier Br atoms. Fig. 3.2 shows the packing perpendicular to the b stack axis. The red and blue color distinguishes molecules lying on different planes. It is seen that the long axes of the molecules are aligned each other, almost parallel to the a crystal axis. Furthermore, TMB and CA (BA) molecules alternate along a, connected by a network of O$\cdots$HN contacts, while molecules of the same species are found along c. The O$\cdots$HN contacts are probably at the origin of the planarity of the NH_2 groups of TMB.

Fig.3.3 shows the absorption IR spectra of TMB-CA and BA, collected with the electric vector polarized perpendicular to the stack axis. For TMB-BA, we superimpose the reflectance spectrum to the absorption one, since the crystal is thick and in absorption some bands saturate the spectrum. According the above described crystal structure, this polarization will show only the IR active vibrational modes in the plane of the molecules, where the charge sensitive vibrations occur [51, 52]. In particular, we make reference to the C=O antisymmetric stretching, because it is easily identified and has a quite large ($\sim$ 160 cm^{-1}) ionization frequency shift.

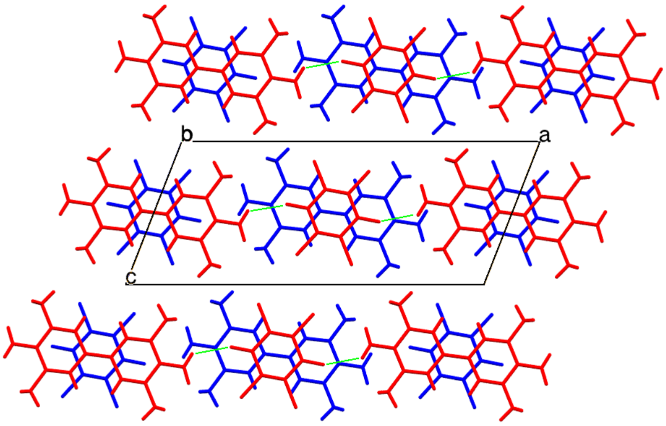

Figure 3.2: Crystal structure of TMB-CA (and the isomorphous TMB-BA) viewed from the b stack axis. Red and blue color distinguish molecules lying on different planes parallel to ac. The green lines put in evidence the O$\cdots$HN contacts

The frequencies of this mode in the CT crystals are reported directly in the Figure, and yield $\rho = 0.14$ and 0.16 for TMB-CA and TMB-BA, respectively. These values are somewhat smaller than the corresponding ones of TTF-CA [35], the prototype CT crystal undergoing the neutral-ionic phase transition [12, 11].

Fig. 3.4 reports the TMB-CA and BA mid-IR absorption spectra polarized along the b stack axis. As expected, these spectra are dominated by out-of-plane vibrations. In the Figure we also shown, superimposed to the IR, the unpolarized Raman spectra (red trace), in order to verify the occurrence of the so-called sidebands, signatures of the presence of a soft mode [35]. These are somewhat difficult to identify, particularly in TMB-CA due to the presence of overlapping bands. However, a pair of sidebands per spectrum can be singled out, as indicated by the green arrows in the Figure. The frequency difference between the sideband and the corresponding Raman central peak is about 80 and 65 cm^{-1} for TMB-CA and TMB-BA, respectively. These frequencies are interpreted as the frequency of the effective soft mode [35, 53] which ultimately might yield to the Peierls distortion [54]. However, we did not observed sign of phase transitions down to 14 K.

In correspondence with the Raman peaks connected to sidebands, and assigned to totally-symmetric modes, we observe a weak IR band located at the same frequency. This frequency coincidence cannot be accidental, in particular for the rather well isolated bands at 981 and 910 cm^{-1}, assigned to the $a_g\nu_3$ mode of CA and BA, respectively [51], lowered by the electron-molecular vibration (e-mv) interaction [38]. The occurrence of frequency coincidence means that the *same* mode is active in Raman and IR, in contradiction with the mutual exclusion rule implied by the X-ray, that indicate both TMB and haloquinones as residing on inversion center. In other words, the vibrational spectra signal that the stack is slightly dimerized, and not regular as indicated by X-ray. Since the IR bands are very weak, the distortion is indeed very small, and might be due to static or dynamic disorder induced by the TMB methyl group. In fact, X-ray detect long range order only, whereas Raman-IR coincidence might be due to a local distortion. Furthermore, the position of hydrogens is not precisely identified by X-ray, and some disorder in the methyl groups seems to be present in the case of TBM-CA.

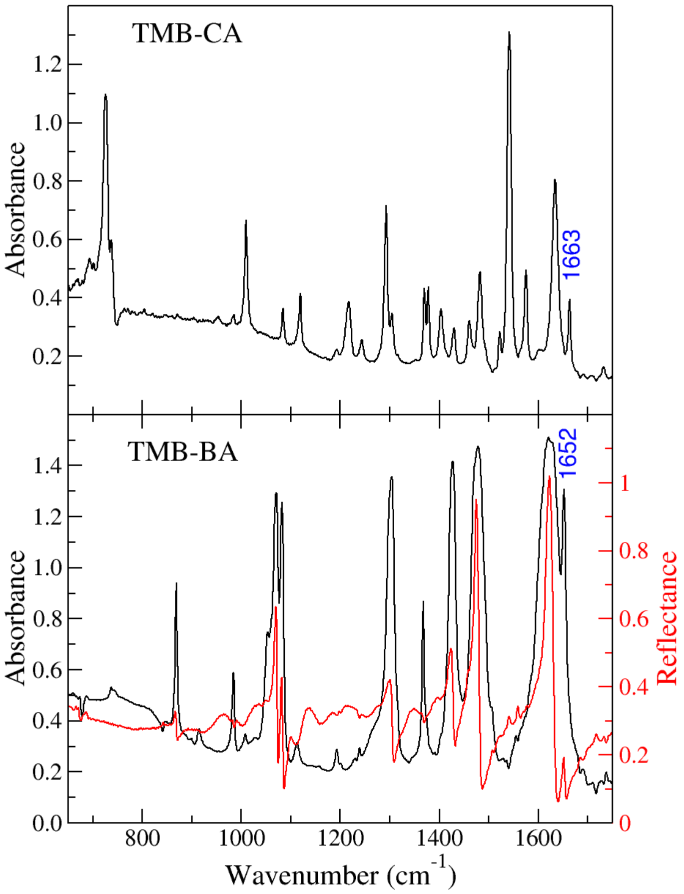

Figure 3.3: IR spectra of TMB-CA (top) and TMB-BA (bottom) polarized perpendicularly to the stack axis.

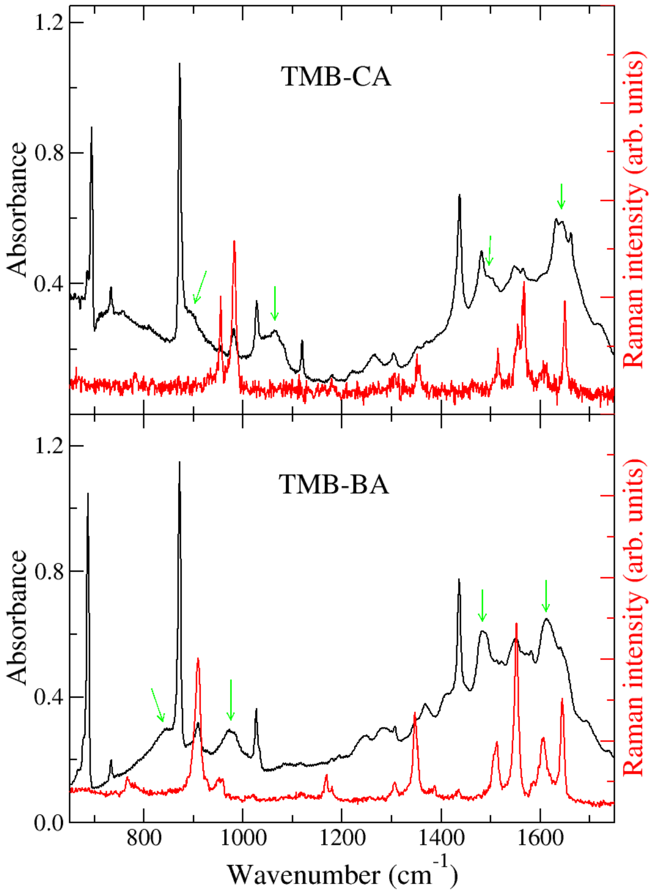

Figure 3.4: IR spectra of TMB-CA (top) and TMB-BA (bottom) polarized parallel to the stack axis, compared to the corresponding unpolarized Raman spectra (red line).

Table 3.2: Basic structural parameters of TMB-TCNQF$_x$

	TMB-TCNQ[a]	TMB-TCNQF$_2$	TMB-TCNQF$_4$
Class	$P2_1/n$, $Z = 2(i)$	$P2_1$, $Z = 2(1)$	$C2/m$, $Z = 2(i)$
a(Å)	6.708(3)	6.691(2)	8.831(6)
b(Å)	21.797(7)	21.813(7)	22.852(16)
c(Å)	8.074(3)	8.188(3)	6.679(4)
β (deg)	100.35(5)	100.755(5)	116.499(9)
V(Å^3)	1161.33	1174.05	1206.26

[a] Ref. [27]

3.3 TMB-TCNQF$_x$

The detailed characterization of the ms-CT crystal made by TMB with TCNQ [27] was presented in the previous Chapter 2 where it was shown that around 200 K, TMB-TCNQ undergoes a valence instability, with a slight increase of ρ from 0.29 to 0.41. Basic structural data are reported in the first column of Table 3.2. Since in this Chapter we are not dealing with phase transitions, the attention will be focused on ambient temperature characterization.

Since TMB-TCNQ undergoes a valence instability at relatively high temperature, we decided to couple TMB with two stronger acceptors, TCNQF$_2$ and TCNQF$_4$. The X-ray crystal structure data are compared in Table 3.2 with those of TMB-TCNQ and TMB-TCNQF$_4$. The crystal structure of TMB-TCNQF$_2$ looks like it were derived from that of TMB-TCNQ: The stacking axis is the same (a) and the cell dimensions are similar (Table 3.2). However, there is a loss of the inversion center and the plane of symmetry. Loss of the inversion center means that the stacks are dimerized, as clearly shown in Fig. 3.5. However, at variance with the low-temperature phase of TTF-CA [43] and TMB-TCNQ, the arrangement of the two DA pairs in the unit cell is anti-ferroelectric. The molecules deviate from planarity, possibly due to CN$\cdots$H$_2$N contacts. As in the case of the other TMB CT

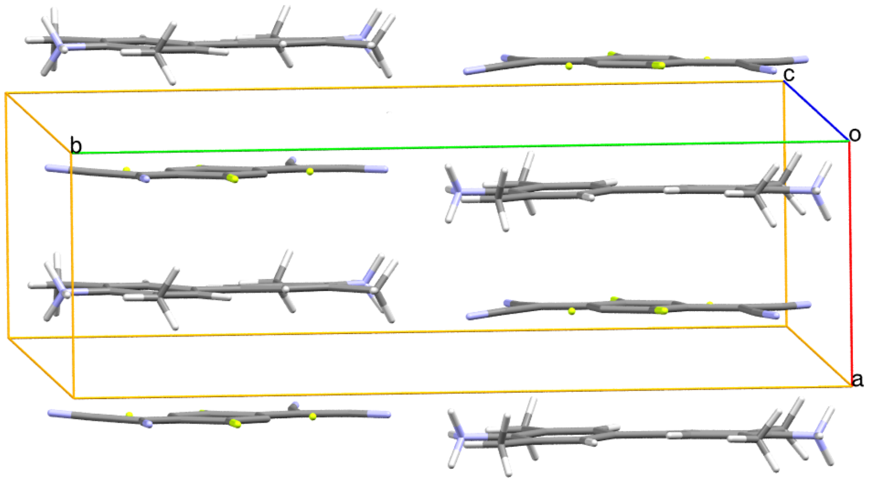

Figure 3.5: Crystal structure of TMB-TCNQF$_2$

co-crystals, TMB and the acceptor molecule are aligned along their long axes. In the present case this implies that there is disorder in the reciprocal arrangement of the molecules, as TCNQF$_2$ has two equivalent positions, rotated by 180°around the axis perpendicular to the molecular plane.

The analysis of the vibrational spectra indicate that TMB-TCNQF$_2$ is a quasi-ionic CT crystal, and that the stack is indeed dimerized. The top of Fig. 3.6 shows the IR spectra polarized perpendicularly to the stack axis, where the charge-sensitive in-plane modes are observed. To estimate ρ, the TCNQF$_2$ ring stretching vibrations will be used, as singled out and calibrated in Ref. [47].The frequencies of the two safely identified charge sensitive modes are reported directly in Fig.3.6. The resulting ρ is 0.66. The bottom panel of Fig. 3.6 compares the TMB-TCNQF$_2$ IR spectra polarized along the stack with the Raman spectrum. It is seen that the IR spectrum is dominated by strong absorptions at the same frequencies as the Raman bands. These absorptions are induced by the e-mv mechanism, and are a clear signature of the stack dimerization [38].

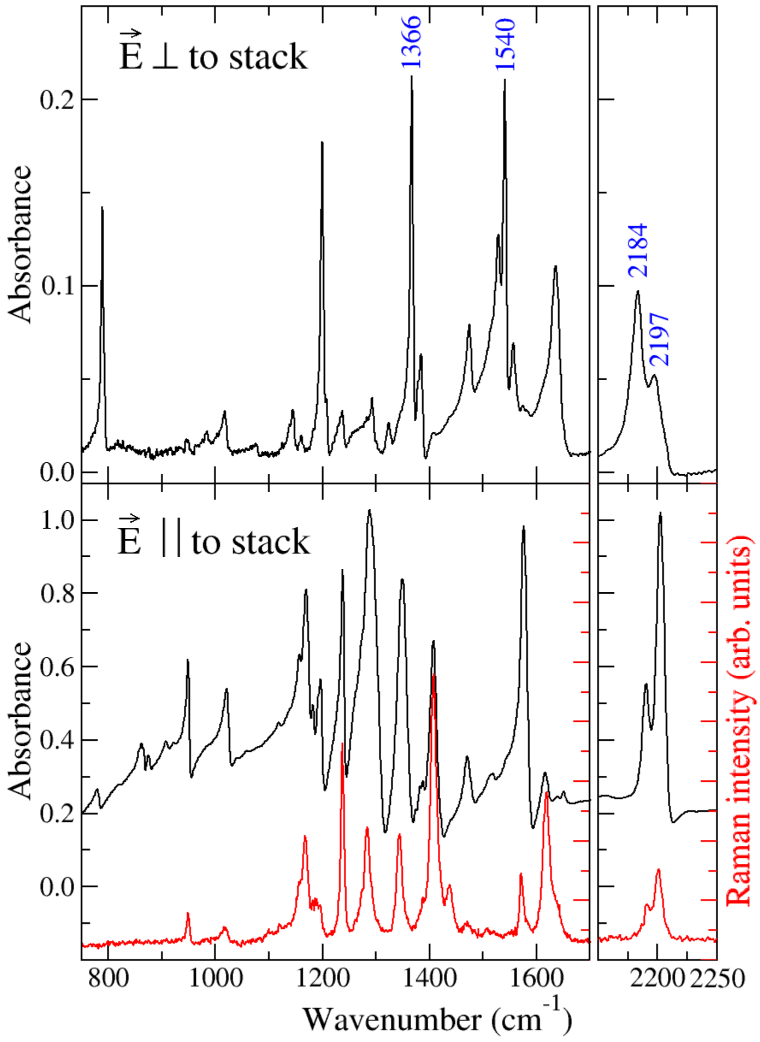

Figure 3.6: Polarized IR and Raman spectra of TCNQF$_2$

The crystal structure of TMB-TCNQF$_4$ is somewhat different from that of TMB-

TCNQ and TMB-TCNQF$_2$: As shown in Table 3.2 and Fig. 3.7, it crystallizes in the monoclinic system $C2/m$ (C^3_{2h}), with two DA pairs per unit cell. The stack axis is c, and the molecules are inclined with respect to the axis. The molecules reside on inversion center, so that the stack appears to be regular. The IR spectra polarized perpendicular to the stack (Fig. 3.8, top panel) indicates that, as expected, TMB-TCNQF$_4$ is more ionic than TMB-TCNQ and TMB-TCNQF$_2$. We have followed the procedure already described for TMB-TCNQF$_2$: three charge sensitive bands have been identified in the CC stretching region [47], and their frequencies (reported in the left top panel of the Figure) indicate a ionicity of 0.91. On the other hand, the IR spectra polarized parallel to the stack (bottom panel of Fig. 3.8) provide a somewhat unexpected result: The presence of strong IR absorptions at the same frequencies of the main Raman band would indicate that the stack is dimerized, like that of TMB-TCNQF$_2$, but this is in contrast with the X-ray crystal structure. X-ray probe long-range order, whereas vibrational spectroscopy probe the local (DA pair) structure, so that one might be thinking of a disordered structure, with opposite distortion, so that on average the stack appears as regular. But this seems to be incompatible with the X-ray atomic thermal ellipsoids. Another similar case is present in the literature [55], but we believe that the problem need to be further investigated before drawing definite conclusions.

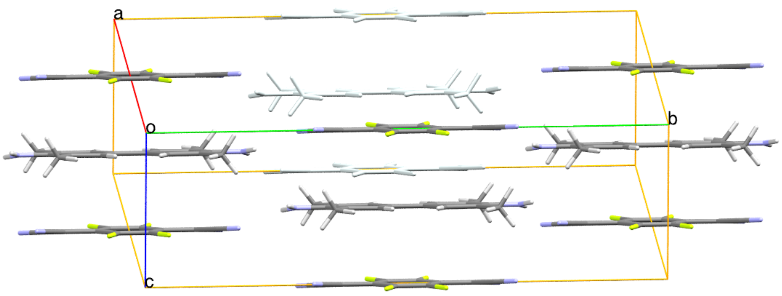

Figure 3.7: Crystal structure of TMB-TCNQF$_4$

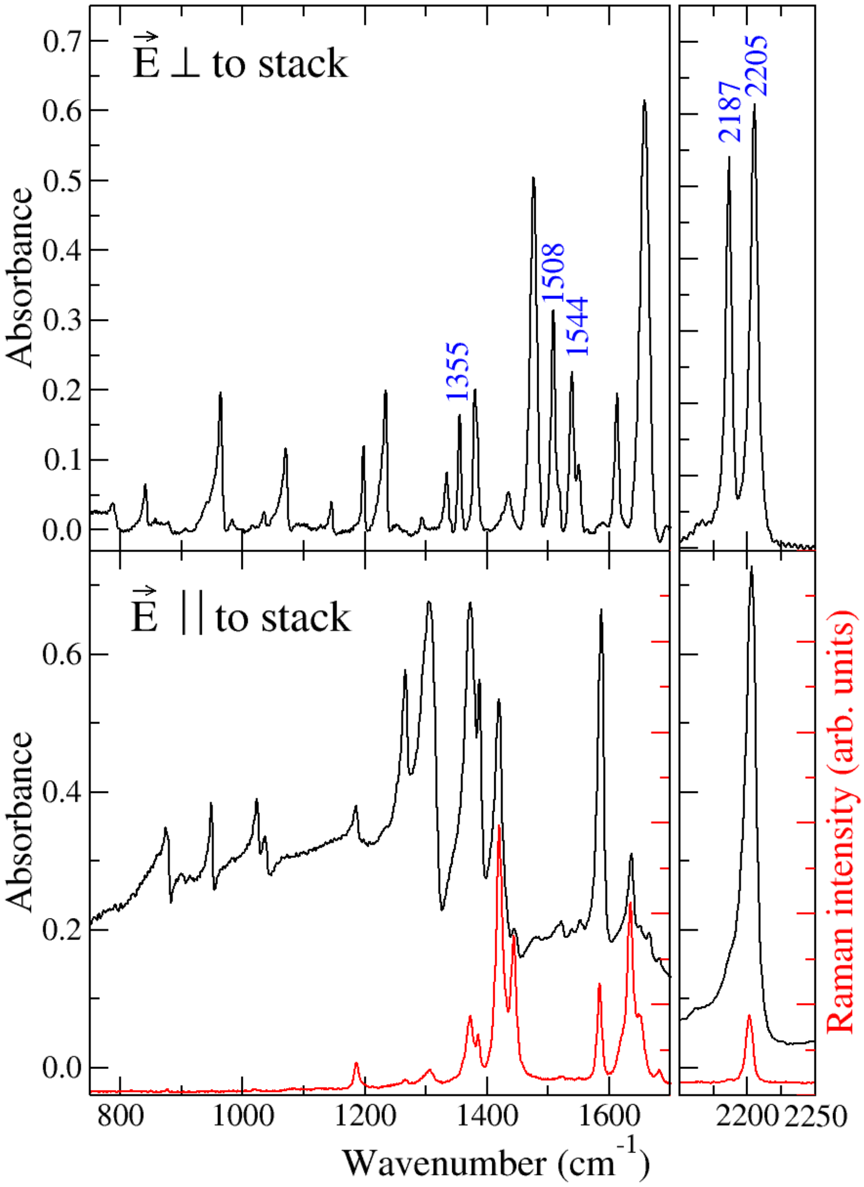

Figure 3.8: Polarized IR and Raman spectra of TCNQF$_4$

Table 3.3: Basic experiment-derived parameters of the TMB-Acceptor series.

System	d (Å)	ρ	ω_{CT} (eV)	t (eV)
TMB-CA	3.322	0.14	0.85	0.19
TMB-BA	3.254	0.16	0.79	0.21
TMB-TCNQ	3.354	0.29	0.60	0.29
TMB-TCNQF$_2$	3.461/3.223	0.66	0.67	–
TMB-TCNQF$_4$	3.340	0.91	0.81	0.17

3.4 Charge transfer transition

We finally investigate the near-IR spectral region, where the CT transition occurs. In this case one has to resort to reflectance spectra, as the absorbance saturates in correspondence with the transition. Due to the strong optical anisotropy of the crystals, only reflectance spectra polarized parallel to the stack axis afforded sufficiently high reflectance. The reflectance spectra of all samples are reported in Fig. 3.9, including the spectrum of TMB-TCNQ. The reflectance reference is a gold mirror, and due to surface irregularities of the samples, the reflectance values cannot be considered as absolute. In Fig. 3.9 we report also the mid-IR region, down to 600 cm^{-1}, where one can detect the out-of-plane vibrational modes and, in the case of TMB-TCNQF$_2$ and TMB-TCNQF$_4$, the e-mv induced modes previously discussed. Due to current experimental limitations, the high frequency limit is 10000 cm^{-1}, preventing a reliable Kramers-Kronig transformation of the data. We have therefore directly fitted the reflectance spectra with a Drude-Lorentz model, using the program RefFIT [56]. In the case of TMB-CA, BA, and TCNQ the CT band appears to have some structure. We tried to fit it with a single or two Lorentians, but the frequency of the main peak does not change significantly. And indeed the only datum that we use from the fitting is the position of the oscillator transverse frequency ω_{CT}. The obtained values are summarized in Table 3.3, and visually marked by a dashed vertical line in Fig. 3.9.

According to exact model calculations for mixed regular stack CT crystals [57], $\omega_{\mathrm{CT}}/(\sqrt{2}t)$ is an U-shaped universal function of ρ, with a minimum around 0.5, where the optical gap closes and the system becomes intrinsically unstable. A glance at Fig. 3.9 shows that $\omega_{\mathrm{CT}}(\rho)$ indeed follows this trend, meaning that t, the DA CT integral, changes little along the series.

In Table 3.3 we compare the experimentally derived basic parameters of the TMB-Acceptor serie, namely d, the interplanar distance between D and A along the stack, ρ, ω_{CT}, and t, the latter obtained from the universal curve of Ref. [57] and the ρ value estimated by IR spectroscopy. The t value is missing in the case of MB-TCNQF$_2$, because the stack is dimerized, but mainly because the calculations suffer from a high degree of uncertainty between $\rho \simeq 0.4$ and $\rho \simeq 0.7$. The interplanar distance is around 3.3 Å for all the systems, by considering the average in the case of the dimerized stack of TMB-TCNQF$_2$. The ionicity, on the other hand, spans from the quasi-neutral TMB-CA to the quasi-ionic TMB-TCNQF$_4$, whereas t remains between 0.2 and 0.3 eV.

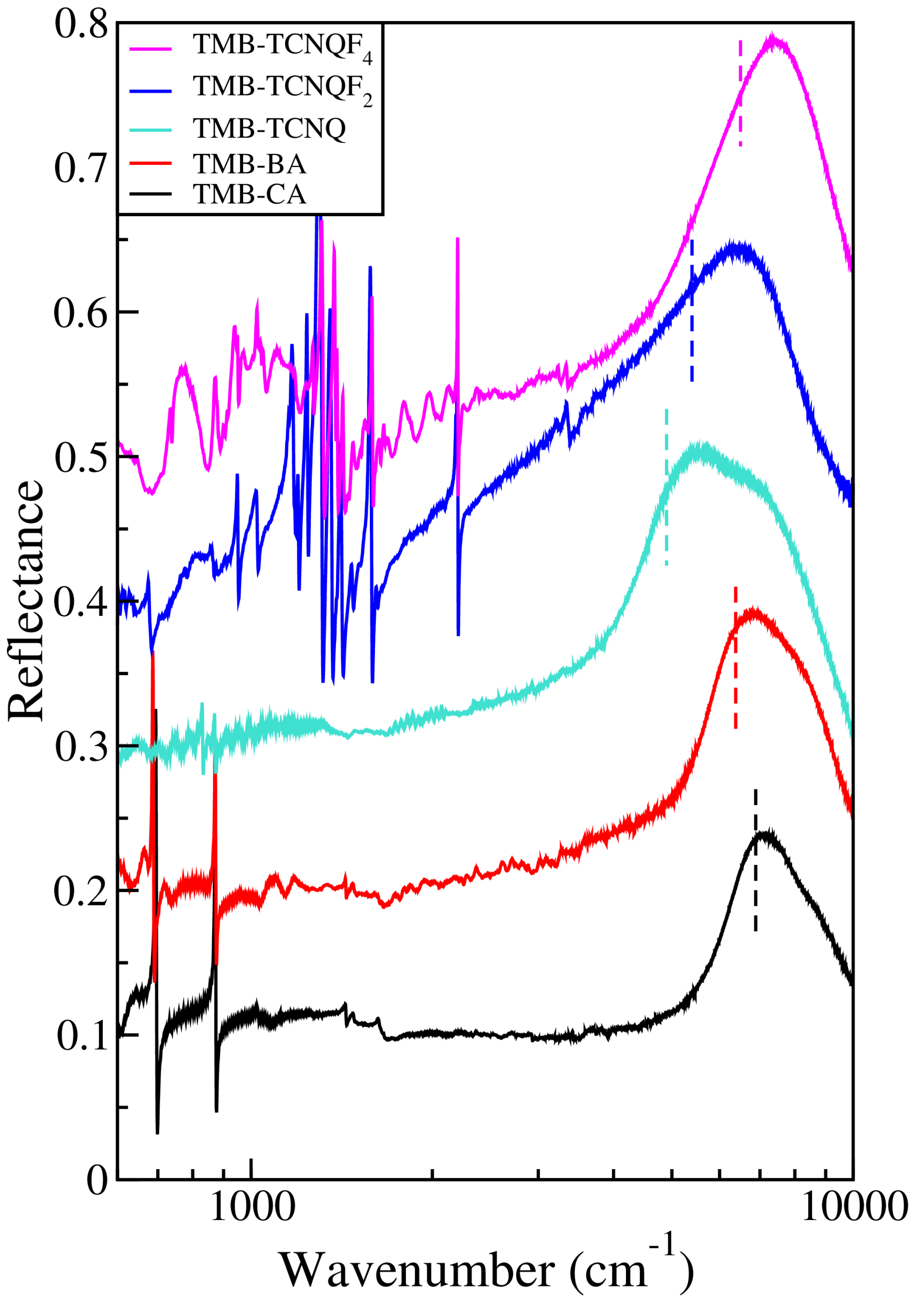

Figure 3.9: Reflectance spectra of the studied TMB-Acceptor CT crystals, with polarization parallel to the stack axis and extension to the near-IR region (10000 cm^{-1}). From bottom to top the spectra refer to: TMB-CA, TMB-BA, TMB-TCNQ, TMB-TCNQF$_2$, TMB-TCNQF$_4$. The spectra are offset by about 0.1 in the reflectance scale for the sake of clarity. Notice the logarithmic wavenumber scale. The dashed lines indicate the oscillator frequency of the Drude-Lorentz model.

3.5 Discussion and Conclusions

The results of the previous Section have shown that the combination of TMB donor with a series of five acceptors of increasing electron affinity provides an extensive exploration of the phase space of ms-CT crystals. At room temperature we have three systems on the neutral side, TMB-CA, BA and TCNQ, with a regular stack. Around 200 K the third system undergoes a valence instability, with dimerization of the stack, but remains on the neutral side ($\rho \simeq 0.4$) [27]. The dimers in the unit cell are arranged ferroelectrically. TMB-TCNQF$_2$ has also intermediate ionicity, but is on the ionic side, and the stack is dimerized, but with anti-ferroelectric arrangement. Finally TMB-TCNQF$_4$ is nearly ionic, and the stack is presumably regular with some degree of local disorder (dimerization). Preliminary investigations have shown that, apart TMB-TCNQ, no other crystal undergoes phase transitions down to 12 K. The ground state experimental behavior fits very well the zero-temperature phase diagram presented many years ago on the basis of an extended Hubbard model including intra- and inter-molecular phonons [58]. Following a recently developed methodology [48], we have undertaken extensive DFT calculations for the five systems at hand, aimed at extracting the basic parameters entering the Hubbard Hamiltonian, in such a way to provide a rationale for the found experimental behavior.

Since we are making a relative comparison in a series of similar molecules, we can safely assume that some of the relevant parameters, like the intramolecular relaxation energy, is approximately constant, so we limit the attention to the following parameters: The CT integral t; half the energy required to form an ionic pair, $z = (I_d - A_A) - (1/2)V$, where I_d is the D ionization potential, A_A is the A electron affinity, and V is the DA intermolecular Coulomb potential; the crystal Madelung energy M. In order to explore the potentiality of the systems to act as ambipolar semiconductors [6], we have also calculated the superexchange hopping integrals for hole and electron transport, t_h^{sxc} and t_e^{sxc}, respectively. The computational approaches are described in Refs. [48, 6] and summarized in Appendix A.

The results are collected in Table 3.4, where the difference $\epsilon_c = V - 2M$ is also reported for convenience.

Table 3.4: Basic computed parameters of the TMB-Acceptor series. Parameter values in eV.

System	z	t	t_h^{sxc}/t_e^{sxc}	V	M	$V-2M$
TMB-CA	0.49	0.26	0.12/0.19	-2.27	-1.49	0.70
TMB-BA	0.47	0.31	0.10/0.16	-2.34	-1.55	0.75
TMB-TCNQ	0.28	0.23	0.16/0.21	-2.03	-1.33	0.62
TMB-TCNQF$_2$	0.11	0.21	–/–	-1.96	-1.30	0.63
TMB-TCNQF$_4$	0.02	0.07	0.29/0.32	-1.89	-0.96	0.03

The monotone decrease of the z values in the first column of Table 3.4 essentially reflects the difference in the electron affinity of the acceptors, slightly affected by an equally monotone decrease of V (fourth column). The computed t values (second column) are in satisfactory agreement with the experimentally derived ones in the fifth column of Table 3.3, also considering the uncertainties in both estimates. The t values are comprised between 0.2 and 0.3 eV, with a slight but appreciable decrease for TMB-TCNQF$_4$ only, probably due to the inclination of the molecules with respect to the stack axis.

As noted in Ref. [6], in mixed stack CT crystals the D-A CT integrals is barely significant for the transport, that for electrons and holes occurs mainly through D and A molecules, respectively. In other words, the electronic coupling has a "superexchange" nature, resulting from the mixing of frontier orbitals of D (or A) trough the bridging A (or D) frontier orbitals. Such superexchange transfer integrals for holes and electrons, t_h^{sxc} and t_e^{sxc}, are reported in the third column of Table 3.4, and can be compared with the corresponding ones calculated by analogous methods for dibenzotetrathiafulvalene-tetracyanoquinodimethane (DBTTF-TCNQ), namely t_h^{sxc} = 0.085 eV and t_e^{sxc}= 0.062 eV [6]. The superexchange integrals of the TMB series are at least as large, or considerably larger (TMB-TCNQF$_4$), and since DBTTF-TCNQ is known to exhibit appreciable hole and electron mobilities [59], one might expect better performances for the TMB co-crystals. However, in ms-CT crystals electron correlations are important [58], and band theory might be inadequate to account for their behavior. It has been indeed noticed that DBTTF-TCNQ crystallizes into two polymorphs, with rather different degree of CT and transfer integrals, yet they exhibit comparable mobilities [59, 60], casting doubts on the proposed mobility mechanism. On the other hand, mobility measurements in the present series would offer a good opportunity to test theoretical models, given the differences of the encompassed parameter values in an otherwise similar packing arrangement.

The Madelung energy in the fifth column of Table 3.4 varies from -1.49 to -0.96, essentially reflecting the three-dimensional packing of the different structures. More interesting are the $V - 2M$ values. Both V and M correspond to attractive interactions, and as such have negative values. Their difference reflects the inter-stack interactions, and positive $V - 2M$ point to the presence of dominant attractive inter-stack interactions, larger than the intra-stack one. This is the case for all the TMB series, but in other cases negative $V - 2M$ have been found [48, 61] typically corresponding to crystals with one DA pair per unit cell. These crystals may exhibit dominant D-D and/or A-A interstack repulsions along directions perpendicular to the stack. Based on the extensive number of investigated systems, we advance the plausible hypothesis that largely positive $V - 2M$ values imply a lattice contraction upon decreasing temperature, whereas strongly negative values point to a lattice instability [61].

Chapter 4

BTBT-TCNQF$_X$ series

BTBT-TCNQF$_x$ series includes the CT crystals formed by the electron donor benzo-thieno-benzothiophene (BTBT) and, like in the case of TMB series, the electron acceptors TCNQF$_x$ (x=0,2,4,), with the electron acceptor character becoming stronger by increasing x. The related BTBT alkylated derivatives that have shown outstanding p-channel semiconducting properties [62, 63] have recently been combined with TCNQF$_X$ acceptors to explore the possibilities of the two-component approach[64, 65]. Surprisingly enough, the obtained transistors are of n-type [65, 66], and the degree of charge transfer do not correlate with the TCNQF$_X$ acceptor strength, like it happens with other mixed stack CT crystals, e.g. the perylene-TCNQF$_X$ series [31, 47] or the TMB-TCNQF$_x$ series (Chapter 3). In order to disentangle the possible effects of the alkyl side-chains on this behavior, we decided to investigate the physical properties of the charge transfer crystals of the TCNQF$_x$ series of acceptors (x= 0, 2, 4) with unsubstituted BTBT. Independently from us, the same crystals were prepared by Sato et al. [67], and studied in OTFT devices. Here we shall report a more detailed characterization, accompanied by a theoretical analysis aimed at understanding the peculiar properties of this series of crystals.

Single crystals for all the components of group were obtained with the same method by controlled slow cooling as described in details in Subsection 1.3.3. Crystals were grown during a period spent at the Institut de Ciència de Materials de Barcelona (ICMAB-CSIC), Bellaterra, (Spain). X-ray diffraction data collection, spectroscopic measurement and theorethical calculation were performed at the university of Parma. The details are reported in Appendix A.

4.1 Results

All compounds crystallize as alternating ...DADA... stacks. The structures essentially coincide with those independently reported by Sato et al [67]. Crystallographic information is given in Table 4.1 and more detailed one can be found in the deposited CIF files (CCDC: 1556355, 1556356, 1556357). BTBT-TCNQ and BTBT-TCNQF$_2$ are isomorphous, both belonging to the triclinic $P-1$ space group. The molecules are stacked along the a crystal axis, and there is one DA pair per unit cell. Notice that the β angle is almost 90 °. BTBT-TCNQF$_4$ instead crystallizes in the monoclinic $P2_1/c$ group, with two DA pairs per unit cell, stacked along the b crystal axis. In BTBT-TCNQF$_4$ the volume per DA pair is appreciably larger (531.5 Å^3) than in the other two CT crystals. Fig. 4.1 puts in evidence the similarity in the stack

Table 4.1: Experimental structural parameters of BTBT-TCNQ BTBT-TCNQF$_2$ and BTBT-TCNQF$_4$

	BTBT-TCNQ	BTBT-TCNQF$_2$	BTBT-TCNQF$_4$
Space Group	P-1	P-1	P2$_1$/c
Z	1	1	2
a (Å)	7.211(3)	7.1628(12)	7.961(2)
b (Å)	8.009(4)	7.9475(13)	7.0803(19)
c (Å)	8.999(4)	9.1113(15)	19.113(5)
α(deg)	81.261(6)	80.918(2)	90
β (deg)	89.379(6)	89.573(2)	99.347(5)
θ (deg)	87.664(4)	87.924(2)	90
V($\AA^3$)	513.3(4)	511.83(15)	1063.0(5)
DA interplanar distance ($\AA$)	3.3862(8)	3.3495(5)	3.3004(4)
DA interplanar dihedral angle(°)	3.80(6)	2.01(6)	0.5(2)

structure of the isomorphous BTBT-TCNQ and BTBT-TCNQF$_2$, and of BTBT-TCNQF$_4$. In all cases the molecules are tilted by approximately the same angle (about 20°) with respect to the stacking axis. However, the reciprocal arrangement of the stacks is different: The layers perpendicular to the stacking axis are made up of equal molecules in BTBT-TCNQ and BTBT-TCNQF$_2$ (Fig. 4.1, 4.2, 4.3, whereas they are arranged in a chessboard layout in BTBT-TCNQF$_4$ (Fig.4.1 and 4.4). The average planes of BTBT and TCNQF$_x$ are slightly inclined each other, and the inclination decreases in going from TCNQ to TCNQF$_4$, as the inter-planar distance does, changing from 3.386 to 3.300 Å (Table 4.1). The same trend, albeit less pronounced, is found in the analogous series of 2,7-dioctyl[1]benzenothieno[3,2-b][1]benzothiophene with TCNQF$_x$ (8BTBT-TCNQF$_x$) [65].

A detailed view of the structures is reported in Figs. 4.2, 4.3 and 4.4.

Of course, the reciprocal arrangement of D and A molecules is such to give the optimum CT overlap. However, in the case of BTBT complexes the overlap is not only between the HOMO and LUMO of the DA pair, but also involves the HOMO-1 orbital of BTBT [64, 65]. This is pictorially shown in Fig.4.5, where the HOMO, HOMO-1 of BTBT and the LUMO of TCNQ are drawn together with the projection of BTBT molecule over TCNQF$_2$ (the projection over TCNQ and TCNQF$_4$ is similar). This peculiar overlap was already pointed out in the 8BTBT-TCNQF$_X$ series [65]: thus the lateral chains have negligible effects on the one-dimensional packing, as we shall also discuss below. We notice that at variance with other complexes of TCNQF$_2$, for instance with perylene [47], in BTBT-TCNQF$_2$ there is no disorder in the F atoms position resulting from rotational disorder, due to the asymmetrical superposition of BTBT and TCNQF$_2$ along the stack (bottom left side of Fig.4.5)

We now turn attention to the determination of the degree of CT, or ionicity ρ, one of the basic parameters characterizing CT crystals [31, 47, 34, 48]. Sato

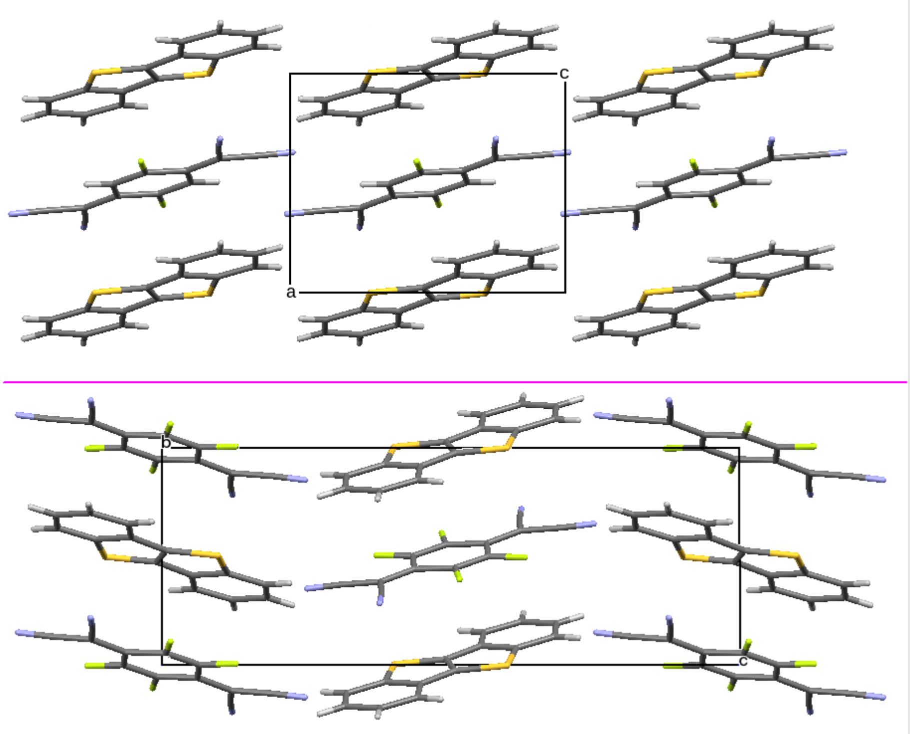

Figure 4.1: (Top) Crystal structure of BTBT-TCNQF$_2$ viewed from the b axis. (Bottom) Crystal structure of BTBT-TCNQF$_4$ viewed from a axis. The chosen view puts in evidence the stack structure and the three dimensional stack arrangement.

et al.[67] used the TCNQF$_X$ bond lengths and the IR CN stretching frequency, obtaining somewhat inconsistent results, as shown in their Table S1. Both methods suffer in fact of some drawback: The bond lengths method depends on the adopted calibration, and the CN stretching frequency is known to give unreliable, generally overestimated, values [33]. As in the case of TMB-TCNQF$_x$ series, we have obtained ρ from the frequencies of other, well tested, IR active charge sensitive modes of TCNQF$_X$ [33, 32].

Fig.4.6 reports the single crystal IR absorption spectra of BTBT-TCNQ, BTBT-TCNQF$_2$ and BTBT-TCNQF$_4$, collected with the electric field of the incident radiation perpendicular to the stack axis, so that the in-plane vibrational modes can be selectively observed. Only the spectral range 1280-1680 cm^{-1} is shown, since all the charge sensitive bands lie in this region. In Fig.4.6 we also report the spectra of BTBT powders, to show that bands originated by this molecule do not interfere with the identification of the charge sensitive bands of TCNQF$_x$ in the three co-crystals. Their frequency is reported directly in the Figure. In the case of BTBT-TCNQ the ionicity is estimated through the position of the TCNQ $b_{1u}\nu_{20}$ C=C antisymmetric stretching. The frequency is shifted by 4 cm^{-1} with respect to the neutral TCNQ. Since the ionization frequency shift of this mode is 47 cm^{-1} [32], we obtain a ρ value of 0.10 ± 0.02. In case of TCNQF$_2$ and TCNQF$_4$ we have three IR active charge sensitive vibrations in this spectral region. For neutral TCNQF$_2$ they are located at 1575, 1550 and 1393 cm^{-1}, with a ionization frequency shift of 50, 63 and 44 cm^{-1}, respectively, [47] and for neutral TCNQF$_4$ they are found at 1599, 1550 and 1396 cm^{-1}, with a ionization frequency shift of 59, 49 and 43 cm^{-1} [33]. From the fre-

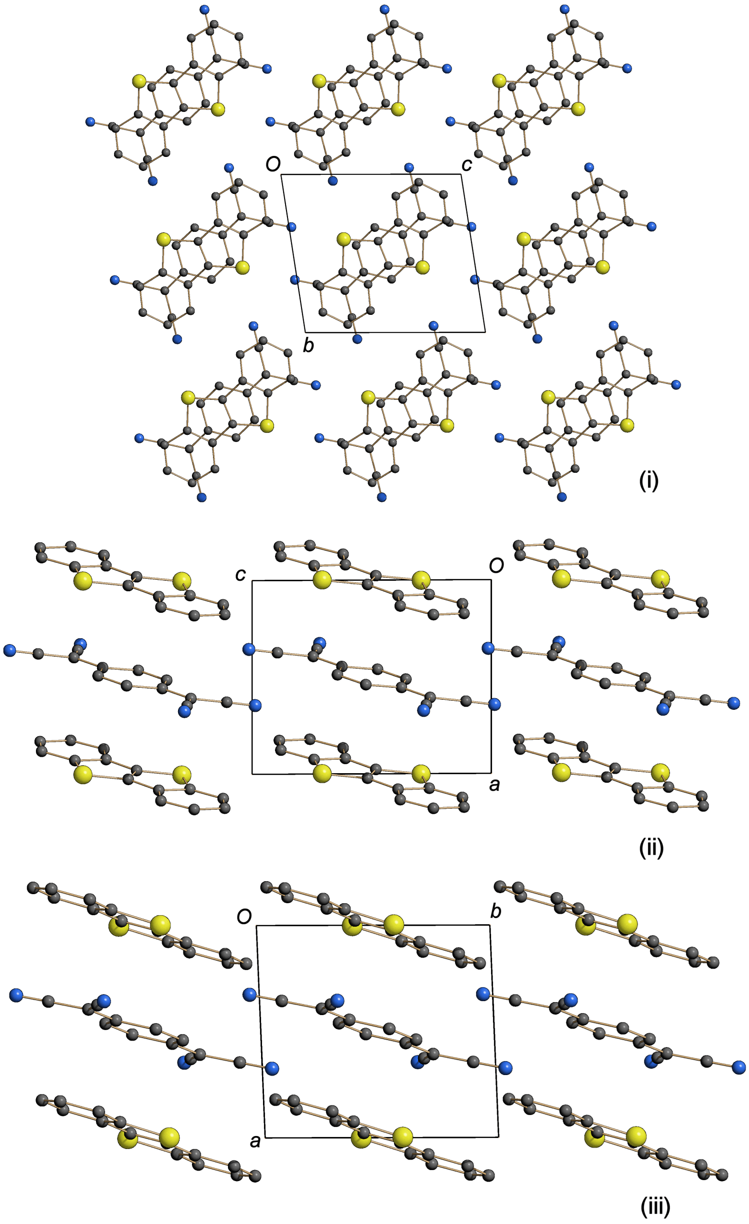

Figure 4.2: Packing diagram of BTBT-TCNQ viewed down the (i) a axis, (ii) b axis and (iii) c axis. Hydrogen atoms are omitted for clarity.

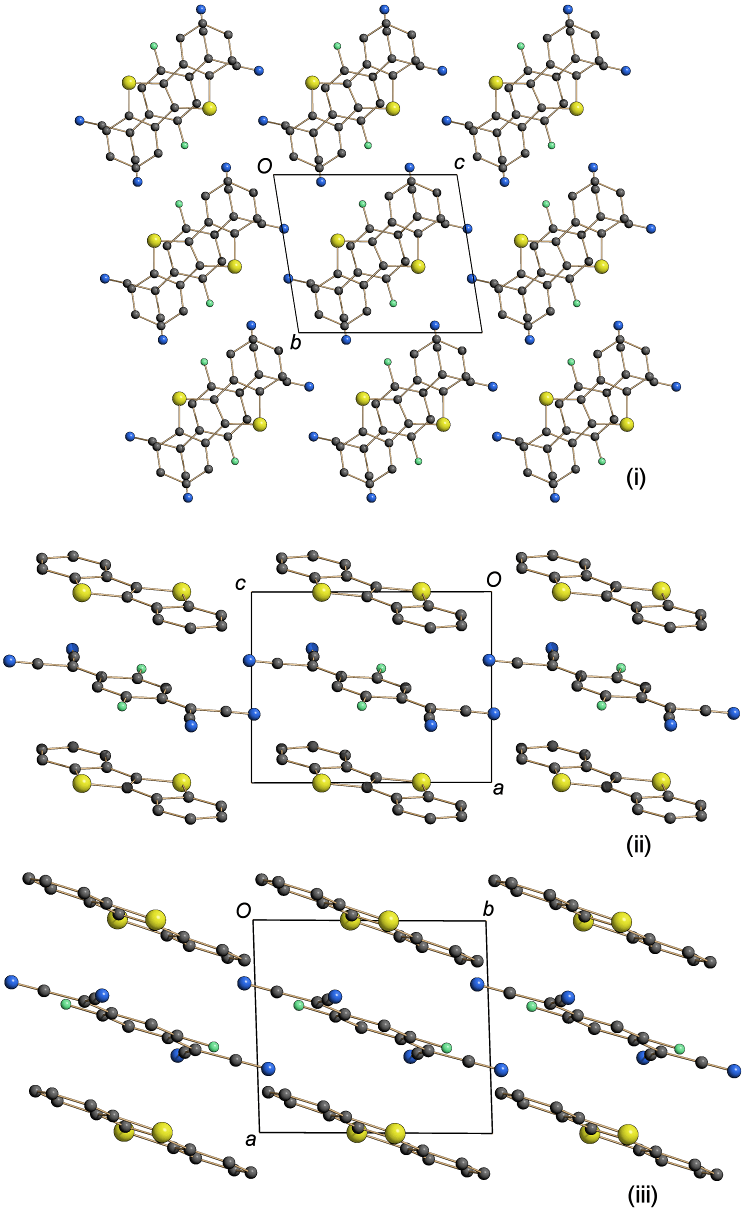

Figure 4.3: Packing diagram of BTBT-TCNQF$_2$ viewed down the (i) a axis, (ii) b axis and (iii) c axis. Hydrogen atoms are omitted for clarity.

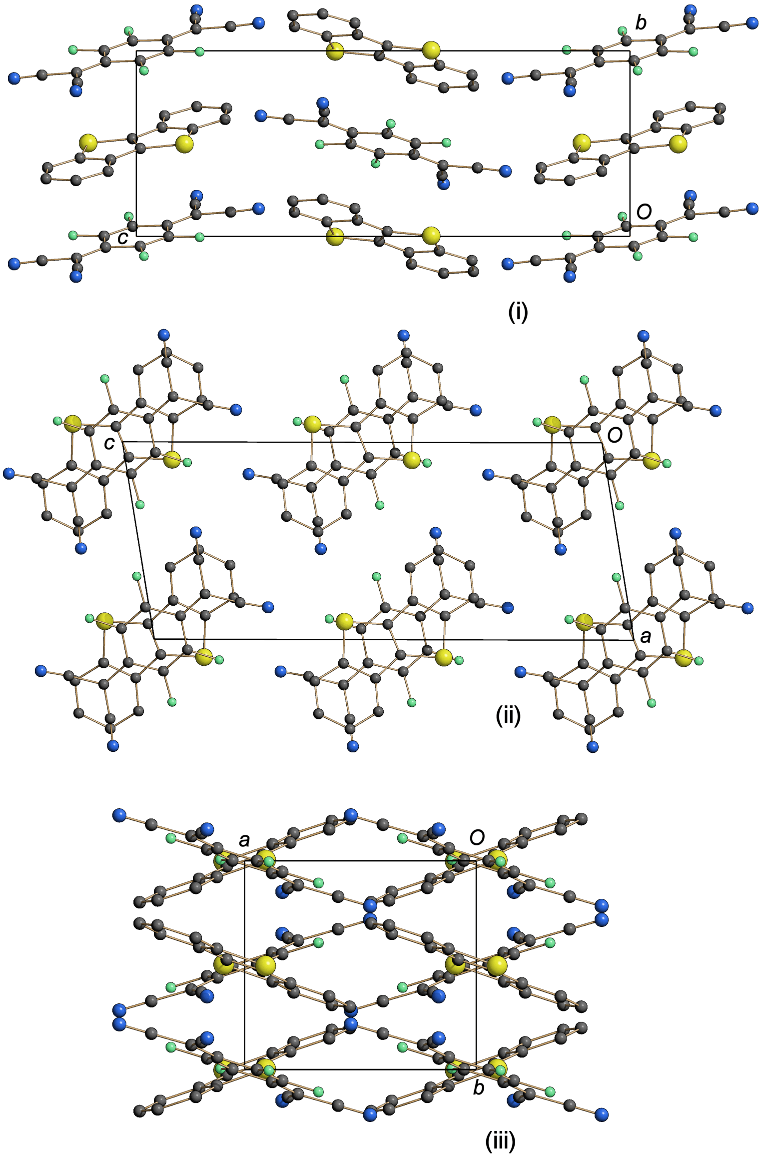

Figure 4.4: Packing diagram of BTBT-TCNQF$_4$ viewed down the (i) a axis, (ii) b axis and (iii) c axis. Hydrogen atoms are omitted for clarity.

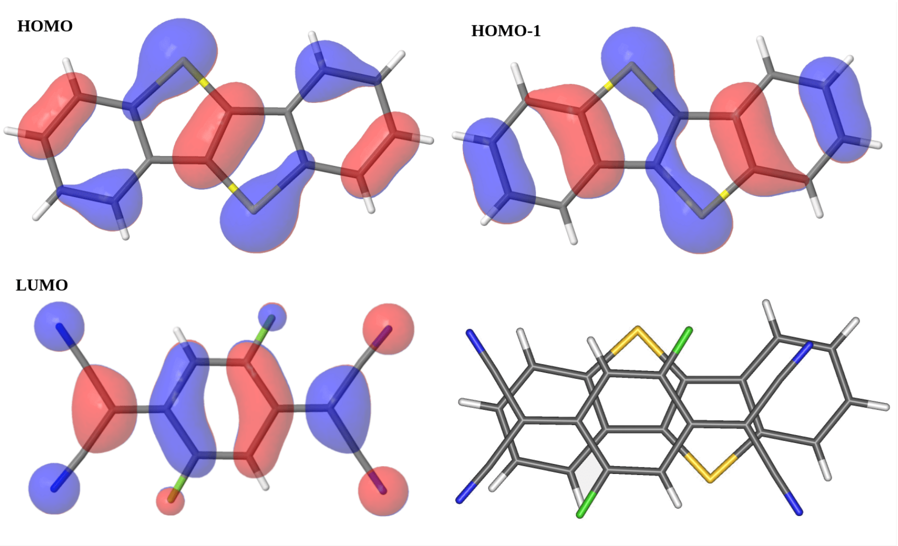

Figure 4.5: Pictorial representation of the HOMO, HOMO-1 of BTBT and of LUMO of TCNQF$_2$, and projection of TCNQF$_2$ on BTBT plane along the stacking axis.

quencies reported in Fig. 4.6 we then derive $\rho = 0.09 \pm 0.05$ and $\rho = 0.12 \pm 0.05$ for BTBT-TCNQF$_2$ and BTBT-TCNQF$_4$, respectively. The averages values we report are weighted by ionization frequency shifts, and the larger uncertainties given for BTBT-TCNQF$_2$ and BTBT-TCNQF$_4$ are due to the fact that some of the charge sensitive bands are split (see bands at ≈1547 and ≈1570 cm^{-1} for BTBT-TCNQF$_2$ and bands at ≈1590 cm^{-1} for BTBT-TCNQF$_4$ in Fig.4.6), probably as a consequence of Fermi resonance with other vibrational modes. The Raman spectra (see Figures 4.7, 4.8, 4.9) confirm that the degree of charge transfer remains more or less the same in the series, around 0.1. This is a somewhat surprising result, since combining the same donor with molecules of increasing electron affinity, one would expect a increasing value of ρ.

4.2 Discussion

Although infrequent, the relative insensitivity of the degree of CT to the difference between the ionization potential of the donor and the electron affinity of the acceptor has been already encountered. Besides the obviously similar case of the co-crystals TCNQF$_4$ with alkylated BTBT [64, 65], this unusual effect has been already explicitly noticed in the CT crystals formed from TCNQ and TCNQF$_4$ with dithieno[2,3-d;2',3'-d']benzo[1,2-b;4,5-b']dithiophene (DTBDT) [68], a molecule which presents some similarity with BTBT, being characterized by the same motif of two fused thiophene rings, separated by a benzene ring. In that case the authors used extensive DFT calculations to try to explain the phenomenon, ascribing it to a difference in the CT mechanism due to the presence of fluorine ligands [68]. We feel that such fully computational approach may be missing some relevant aspect, and in any case the proposed mechanism of the anomaly cannot be extended to the present case, where the overlap between donor and acceptor molecules is the same (Fig. 4.5) in the three studied crystals, and where the BTBT-TCNQ and BTBT-TCNQF$_2$ crystals are isomorphous. We have then decided to follow a different approach, where DFT calculations are only used to estimate the basic parameters entering a simpli-

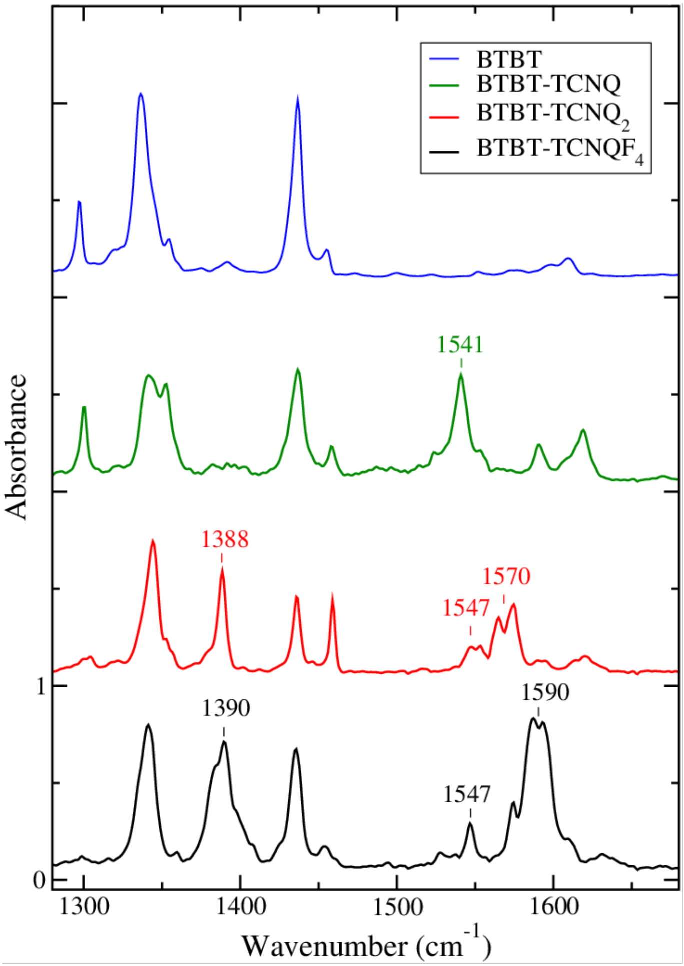

Figure 4.6: IR absorption spectra of BTBT-TCNQ, BTBT-TCNQF$_2$, and BTBT-TCNQF$_4$ single crystals, with polarization perpendicular to the stack axis. The spectra are offset by one absorbance unit for clarity. The top blue line is the spectrum of neutral BTBT powder. The frequencies of the charge sensitive bands are reported.

fied Hamiltonian able to catch the essential physical-chemistry of mixed stack CT crystals. The method has been recently applied successfully to model a series of different CT crystals [48]. Since we are making a relative comparison in a series of similar molecules, we can safely assume that some of the relevant parameters, like the intramolecular relaxation energy, is constant, so that we can limit the calculation to the following parameters: t, the hopping or CT integral between D and A; V, the DA intermolecular Coulomb potential; $z = (I_d - A_A) - (1/2)V$, half the energy required to form an ionic pair (I_d is the D ionization potential and A_A the A electron affinity), and M, the Madelung energy.

Delchiaro *et al.* [48] used a CT dimer model to estimate t and z. However, this two-state model does not consider the possibility of having more than one CT integral, as it is known to occur in BTBT co-crystals: BTBT HOMO and HOMO-1 are close in energy (about 0.5 eV), so we have two CT integrals and two CT transitions [64]. In the present case we have therefore decided to directly calculate z and t. The latter corresponds to the Fock matrix elements between the involved D and A orthogonalized molecular orbitals [69]. The intermolecular Coulomb potential

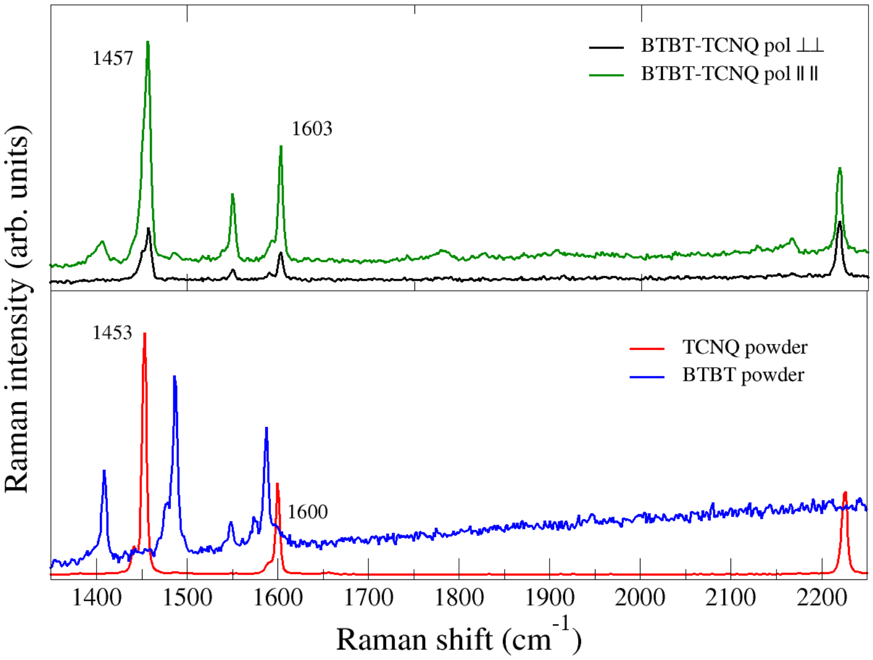

Figure 4.7: Top panel: Polarized Raman spectra of BTBT-TCNQ crystal. Bottom panel: Raman spectra of neutral TCNQ and neutral BTBT powders. Exciting line: 532 nm.

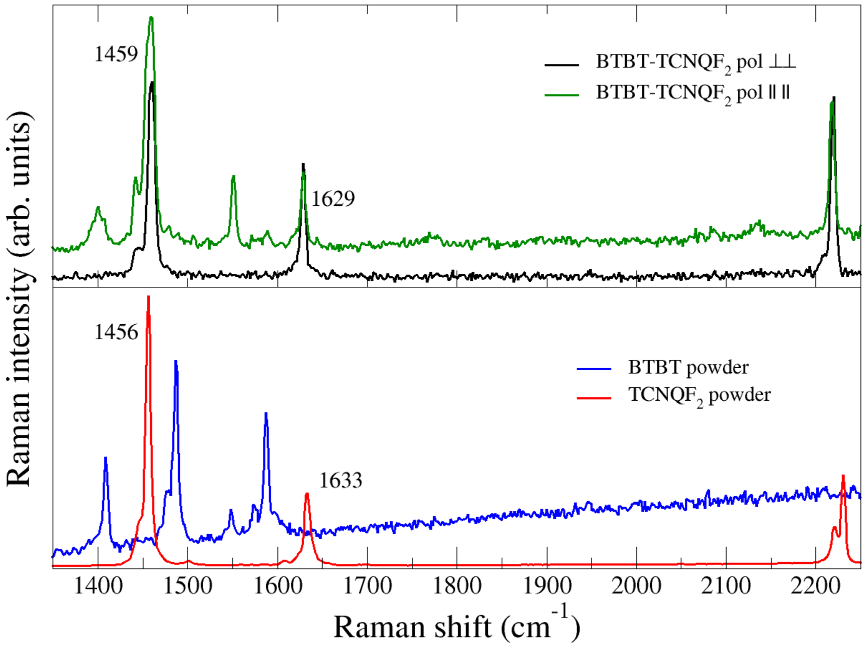

Figure 4.8: Top panel: Polarized Raman spectra of BTBT-TCNQF2 crystal. Bottom panel: Raman spectra of neutral TCNQF2 and neutral BTBT powders. Exciting line: 532 nm.

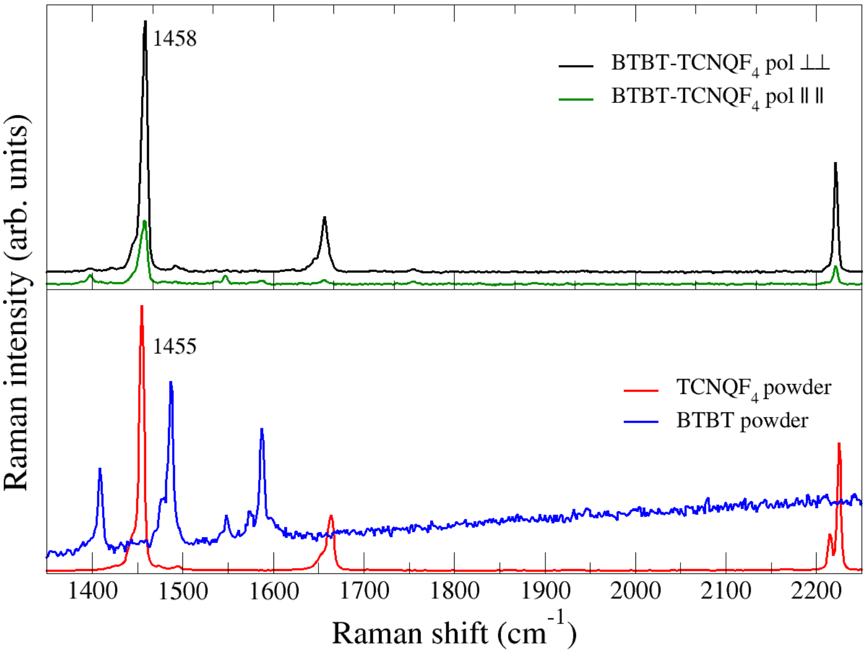

Figure 4.9: Top panel: Polarized Raman spectra of BTBT-TCNQF4 crystal. Bottom panel: Raman spectra of neutral TCNQF4 and neutral BTBT powders. Exciting line: 532 nm.

V and Madelung energy M are calculated in the point-charge approximation of the molecular charge density based on the computed atomic ESP charges. Finally, I_d and A_A energies entering (with V) in the definition of z are taken as the HOMO and LUMO DFT energies. The results of the calculations are summarized in Table 4.2 .

Although only the relative value of the computed parameters is important here, we have nonetheless verified the effect of different choices in the DFT functional and basis set, taking as reference either the experimental values or the results from the dimer model [48]. The basis set choice has in general little influence, provided one uses an extended basis with diffuse contribution, as the 6-31G* of Gaussian [70] or the TZP of ADF [69]. The choice of functional instead affects considerably the orbital energies. In reporting z in Table 4.2, we use the ωB97XD MO energy values, shifting the zero of the energy in such a way that (I_d–A_A) reproduces the experimental difference (1.57 eV) between the ionization potential of BTBT[71] and the TCNQ electron affinity[72]. In any case the difference between the two extremes, BTBT-TCNQ and BTBT-TCNQF$_4$ (about 0.5 eV) is essentially the same whatever DFT functional is adopted, and is always somewhat less than the difference between experimentally determined electron affinities of TCNQ and TCNQF$_4$[72]. In the calculation of t we can divide the effects of the functional in two categories: use of Generalized Gradient Approximations (GGA) always underestimates the t value, whereas hybrid methods such as B3LYP or ωB97XD overestimate it. In Table 4.2 we report the values obtained by GGA-PBE functional and TZP basis set, which compare well with those obtained with similar methods in Ref.[65], and which are underestimated by a constant factor of 1.25 with respect to the experiment and to the dimer model [48]. Finally, the V and M values estimated form ESP charges do not

Table 4.2: Basic computed electronic parameters (eV) of the studied compounds.

System	z	t^*	V	M	$V-2M$
BTBT-TCNQ	0.51	0.12, 0.23	-2.12	-0.96	-0.20
BTBT-TCNQF$_2$	0.25	0.09, 0,22	-2.06	-0.93	-0,20
BTBT-TCNQF$_4$	0.06	0.10, 0.22	-1.99	-1.31	-0.63
10BTBT-TCNQ	0.36 dimer: 0.76	0.11, 0.21 dimer:0.25	-2.00	-1.00	0.00
10BTBT-TCNQ$_4$	-0.10 dimer: 0.57	0.12, 0.21 dimer: 0.23	-1.89	-0.95	0.02

*The two reported values of t correspond to the HOMO-LUMO and (HOMO-1)-LUMO integrals, in this order. In the case of 10BTBT-TCNQ and 10BTBT-F$_4$ the values obtained by the dimer model (Ref. [48]) are reported for comparison.

depend significantly from the adopted functional and basis set. In Table 4.2 we have added for comparison the electronic parameters of 2,7-didecyl[1]benzenothieno[3,2-b][1]benzothiophene (10BTBT) as calculated with the dimer model[48] and by the present method.

First of all, we remark that the CT integrals of 10BTBT-TCNQF$_x$ co-crystals are essentially the same as those of the unsubstituted BTBT, confirming that the sidechains have little effect on the one-dimensional arrangement of donor and acceptor molecules. From Table 4.2 it is also seen that by increasing the TCNQ electron acceptor strength z, the energy required to form a DA pair (first column in Table 4.2) decreases, i.e., the system tends to become more ionic, as expected. The trend is confirmed by the computed degree of CT for the isolated DA pair in gas phase, ρ_{dim} [48]: It is close to zero (0.07) for BTBT-TCNQ and increases monotonically in steps of 0.01 in going from TCNQ to TCNQF$_2$, to TCNQF$_4$, whereas the experimental ρ is estimated to be 0.10, 0.09, 0.12 in the order. It is indeed the Madelung energy M which makes the difference when the DA pair is embedded in the crystal [48]. As shown in the fourth column of Table 4.2, M slightly decreases in going from BTBT-TCNQ to the isomorphous BTBT-TCNQF$_2$, then it increases in BTBT-TCNQF$_4$, despite the fact that in this case we have an increase of the volume per DA pair (Table 4.1). This nonlinear trend accounts for the experimental ρ values found in the three co-crystals: There is practically no change by replacing TCNQ with TCNQF$_2$, as the decrease of z is compensated by the decrease of M. In BTBT-TCNQF$_4$, on the other hand, both the decrease of z and the increase of M cooperate to the very small increase of ionicity.

Even if both z and M contribute to increase the degree of CT in BTBT-TCNQF$_4$ with respect to BTBT-TCNQ, the increase is almost nil, at variance with other cases [47]. This is due to the effect of CT integral: The larger is t, the larger is the electron delocalization along the stack, and the smaller the effect of z and M [48]. In the case of BTBT we have two CT integrals, whose combined effect is at the origin of the insensitivity of ρ to the increased electron affinity of the TCNQF$_x$. Notice incidentally that the (HOMO-1)-HLUMO CT integral is about twice the HOMO-LUMO one. This has to be ascribed to a better overlap, as it can be appreciated from Fig. 4.5.

The fact that in BTBT the two frontier HOMOs are close in energy has been already remarked in the context of co-crystals involving BTBT and BTBT derivatives,[64, 65] but as far as we know the consequences on the physical properties of the various systems have not been extensively addressed. For instance, we believe that the small energy difference (≈ 0.5 eV) between HOMO and HOMO-1 has the likely consequence of the lack of symmetry between the conduction and valence band, a requirement for ambipolar transport in CT crystals, [6] and indeed, BTBT-TCNQF$_X$ co-crystals exhibit n-channel transport only [67]. On the other hand, this proximity might well explain the very good p-channel semiconducting properties of pristine BTBT derivatives [63].

A more detailed discussion of the above points goes beyond the aim of this thesis. We finally address the question of why the Madelung energy slightly decreases in going from BTBT-TCNQ to the isomorphous BTBT-TCNQF$_2$, although the unit cell volume is decreasing (Table 4.1). As a matter of fact, the three dimensional packing of the DA stacks explains the effect of the Madelung energy. This is clearly seen in Fig. 4.10, which shows the layers of BTBT and TCNQF$_x$ perpendicular to the stacking axis of BTBT-TCNQ and BTBT-TCNQF$_2$. Since the structures have a DA pair per unit cell, the layers perpendicular to the stacks contains molecules of the same kind. Fig. 4.10 reports the shortest distances between H, F and N atoms in nearby molecules. Since the (negative) molecular charge in TCNQF$_x$ is concentrated on the N, but also in F atoms when present, the repulsion between the stacks is increased in BTBT-TCNQF$_2$ with respect to BTBT-TCNQ, hence the decrease of the Madelung energy. This electrostatic effect can also explain why the BTBT-TCNQF$_4$ structure is not isomorphous with the other two. The presence of two more F atoms would make the triclinic structure less stable, with a further decrease of the electrostatic energy. Therefore BTBT-TCNQF$_4$ prefers to adopt the monoclinic structure, with two DA pairs per the unit cell, so that in the layers perpendicular to the stack we have the same kind of molecules along the *c* axis, but BTBT and TCNQF$_4$ alternate along the *a* axis (Figure 4.4).

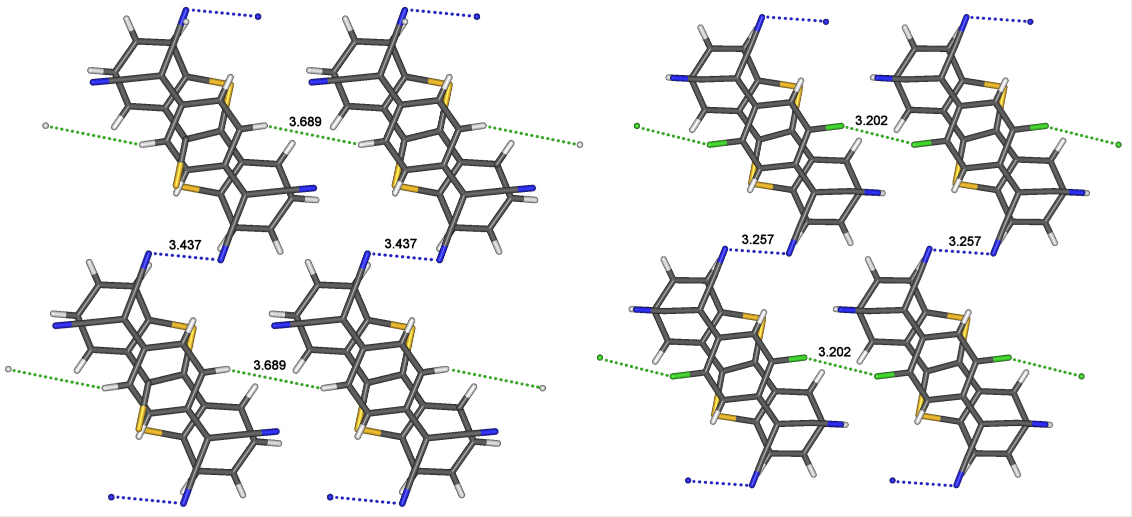

Figure 4.10: View of the isomorphous BTBT-TCNQ and BTBT-TCNQF$_2$ structures perpendicular to the stacking axis, showing the H-H, N-N and F-F shortest distances.

In order to give a more quantitative basis to the above discussion, we report in the rightmost column of Table 4.2 the difference between V and $2M$ (the 2 factor is due to the definition of V and M [48]). V represents the attractions between nearby oppositely charged molecules, and essentially represents the intra-stack Coulomb potential. The Madelung energy M is instead the three-dimensional Coulomb potential, extended to the whole crystal so that $V-2M$ is representative of inter-stack interactions. Negative values, as in the case of BTBT-TCNQ and BTBT-TCNQF$_2$, point to the presence of dominant repulsive inter-stack interactions, larger than the attractive intra-stack interaction. To test the idea that the change of structure of BTBT-TCNQF$_4$ is due to unfavorable electrostatic interactions, we have calculated V–$2M$ for an hypothetical triclinic structure of BTBT-TCNQF$_4$, isomorphous with the other two structures in the series, and we have indeed found a very large negative value, -0.59 eV, which indicates an unstable structure. On the other hand, in systems with small or positive V–$2M$, intra- and inter-stack interactions compensate each other. As shown in Table 4.2, this is the case of BTBT-TCNQF$_4$, but also of 10BTBT-TCNQ and 10BTBT-TCNQF$_4$. The structure of the two latter systems is similar to that of BTBT-TCNQ, triclinic centro-symmetric with one DA pair per unit cell, but in this case nearby equal molecules in the layer perpendicular to the stack are kept apart by the lateral alkyl chains, giving another indirect indication of the importance of electrostatic interactions in establishing the three-dimensional packing of the co-crystals.

4.3 Conclusions

A combined structural and spectroscopic characterization of the series of CT crystals BTBT-TCNQF$_x$ is reported. Through an accurate determination of the degree of CT by polarized IR spectra we have detected a rather anomalous behavior: At variance with other series involving different donors, like perylene [47] or TMB, we have found that ρ increases very little, and in a nonlinear manner, on increasing the TCNQF$_x$ electron accepting strength from TCNQ to TCNQF$_4$. Extensive calculations have allowed us to explain this anomaly as due to the combination of the CT mechanism involving both HOMO and HOMO-1, and three-dimensional Madelung energy. Focusing attention on the latter, we have discovered that the difference in the crystal packing between BTBT-TCNQ and BTBT-TCNQF$_2$, on one side, and BTBT-TCNQF$_4$ on the other, is due to the differences in the interstack electrostatic interactions, as measured by $V - 2M$. From this point of view, the comparison with alkylated BTBT-TCNQF$_X$ co-crystals [65] shows that the role of the alkyl chains is just that of keeping apart the DA stacks, reducing the effect of three-dimensional electrostatic interactions. We believe the above is an important clue in the endeavor to understand the role of intermolecular interactions in the crystal packing of CT crystals.

Chapter 5

TTB and TCNQ

An interesting electron donor, 1,1,4,4-tetrathiabutadiene (TTB), for which just the synthesis and a preliminary characterization of some of its CT crystals is present in the literature [73], is revisited in this Chapter. Here it is reported a detailed spectroscopic, structural and computational characterization of TTB and of the corresponding co-crystal TTB-TCNQ, extending the knowledge basis of mixed stack CT crystals, and showing that this forgotten molecule and its variants have the potential of affording new systems with perspective applications.

5.1 TTB

Chemical synthesis of TTB molecule was performed at Institut de Ciència de Materials de Barcelona (ICMAB-CSIC), Bellaterra, (Spain) following the literature recipe [73]. The synthesis afforded TTB powders, and crystals suitable for XRD were not obtained. We have first performed a DFT calculation of the isolated molecule and its ion.

The minimum energy conformation of neutral and ionic TTB in gas phase has C_i symmetry, with a planar central skeleton and out-of-plane staggered arrangement of the terminal CH_2-CH_2 groups. As chemical intuition suggests, the HOMO is concentrated on the double bonds and sulfur atoms (Fig.5.1). The double bonds will then be weakened upon electron removal, as it happens with electron Donors based on the TTF skeleton. The HOMO energy can be taken as a relative measure of the ionization potential. The TTB HOMO energy is calculated to be - 4.59 eV,

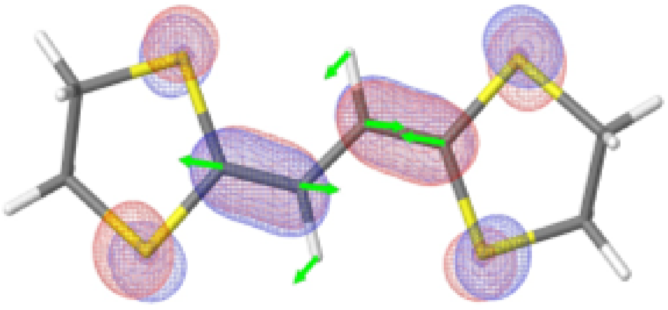

Figure 5.1: Representation of the TTB HOMO. The eigenvectors of the IR active antisymmetric C=C stretching vibration are also shown (green arrows).

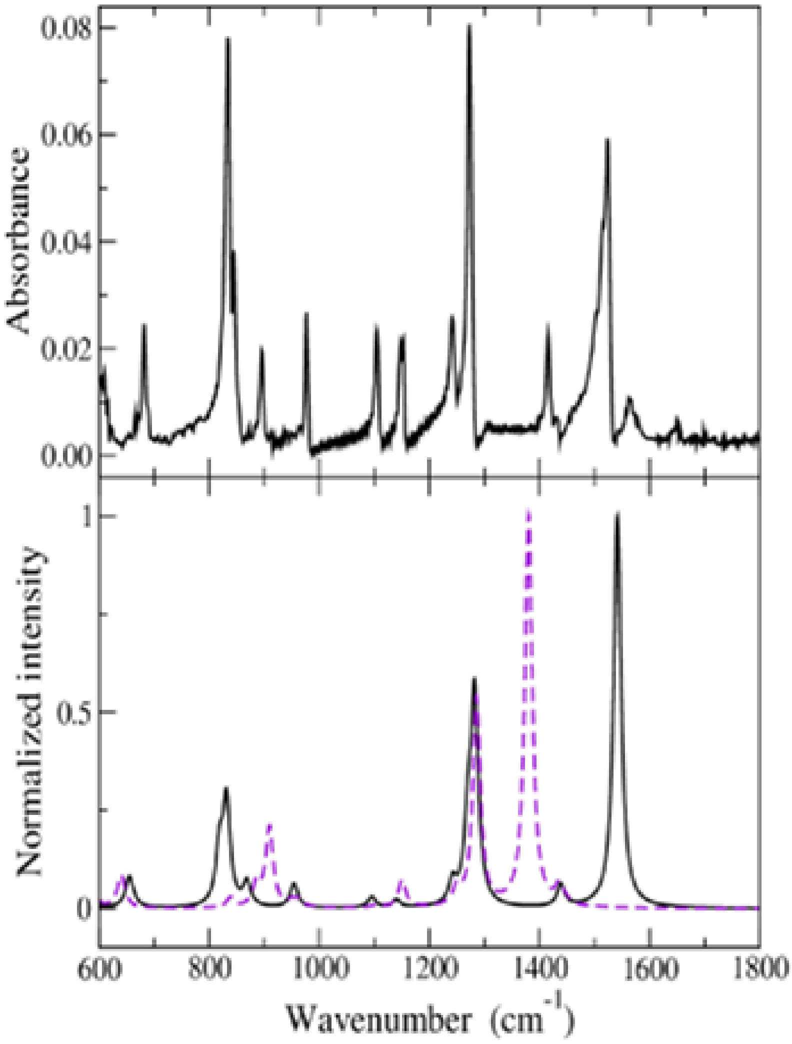

Figure 5.2: Top panel: Experimental IR spectrum of TTB powders. Bottom panel: Calculated IR spectrum of neutral TTB (black line) and TTB$^+$ (violet dashed line).

only 0.13 eV lower than that of TTF (- 4.46 eV, calculated by the same method). Then apparently the electron donor strength of TTB is only slightly smaller than that of TTF, in agreement with measured UPS vertical-ionization energy, less with the relevant ionization potentials [73].

For the free TTB molecule in the C_i conformation, group theory predicts 30 vibrational modes of a_g symmetry, active in Raman, and 30 modes of a_u symmetry, infrared (IR) active. Calculations yield the vibrational assignment of the neutral molecule, as reported in Appendix B. The experimental IR and computed spectra are compared in Fig. 5.2. The experimental IR and computed spectra are compared in Fig. 5.2. The calculated IR spectrum of TTB$^+$ is also reported in the same Figure, in order to put in evidence the charge sensitive vibrational modes which allow the estimation of the degree of charge transfer[52, 74] in the CT complexes in which TTB may be involved. It is seen that the antisymmetric C=C stretching, whose eigenvectors are pictorially represented in Fig. 5.1, and occurring at 1524 cm^{-1}, is the one exhibiting the largest ionization frequency shift, about 160 cm^{-1}. Of course, also the corresponding Raman active C=C symmetric stretching (Table B.2) has a large ionization shift, but this mode mixes with the symmetric stretching of the central C-C bond, and in any case the totally symmetric modes, being coupled with the CT electron, cannot be used to estimate the ionicity of mixed stack CT crystals [75]. We finally notice that the a_u C-S stretching mode located at 834 cm^{-1} is expected to exhibit a considerable (about 70 cm^{-1}) upward frequency shift upon ionization (Fig. 5.2 and Table B.2).

5.1.1 TTB-TCNQ

TTB-TCNQ crystals were obtained by the solvent diffusion method by the Padova university. TTB-TCNQ crystallizes in the triclinic system, space group $P-1$, with one DA pair per unit cell. The basic crystallographic parameters are reported in Table 5.1. Full information is given in the deposited CIF files (CCDC:1576020). The present structure is different from the monoclinic one reported in Ref. [73], probably a case of polymorphism due to a different crystallization procedure. Fig. 5.3 reports two views of TTB-TCNQ crystal structure. The left view shows the ...DADA... stacking along the a crystal axis, and the right view puts in evidence the TTB–TCNQ overlay, with the long axes of the two molecules approximately perpendicular one another, in such a way to maximize the frontier orbital overlap. For what concerns the estimation of the degree of charge transfer ρ, according to

Table 5.1: Room temperature crystal structure of TTB-TCNQ

Space Group	$P-1$
a(Å)	6.9177
b(Å)	8.9769
c(Å)	9.0882
$\alpha(deg)$	68.2461
$\beta(deg)$	77.9771
$\gamma(deg)$	88.7500
Z	2
$T(K)$	294
V(Å^3)	511

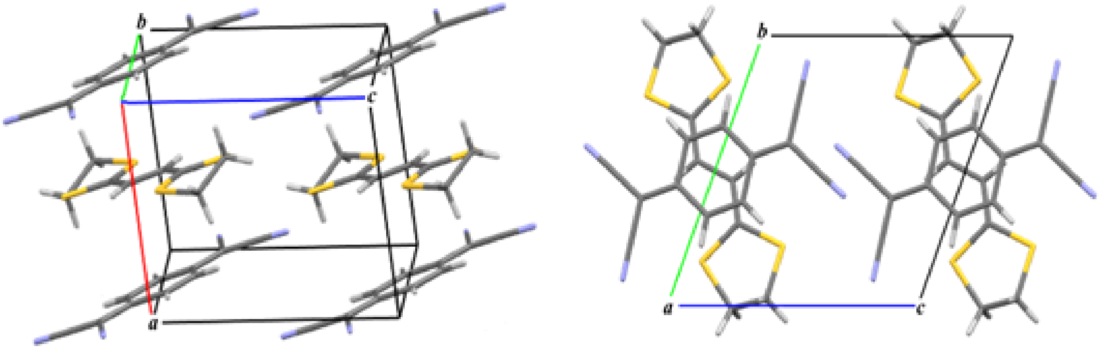

Figure 5.3: Left panel: Crystal structure of TTB-TCNQ. Right panel: Crystal structure of TTB-TCNQ viewed from the a stack axis.)

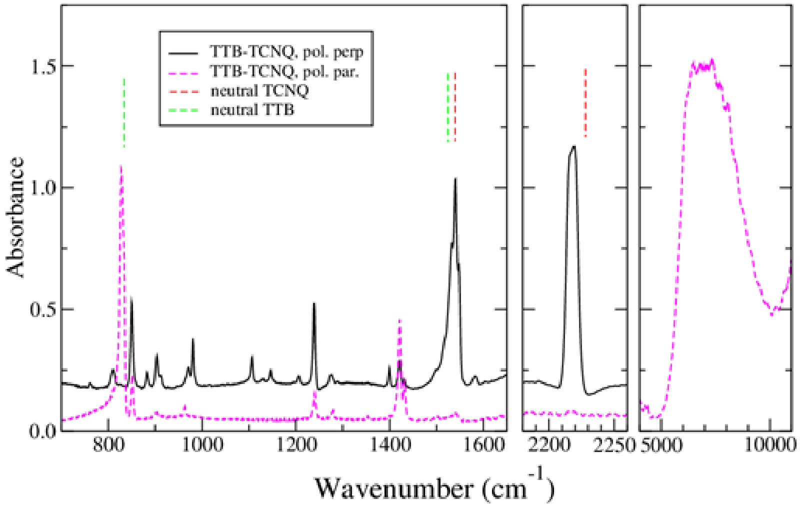

Figure 5.4: Polarized IR spectra of TTB-TCNQ in the spectral regions of the charge sensitive vibrations and of the CT transition. Black continuous line: electric vector perpendicular to the stack axis. Magenta dashed line: electric vector parallel to the stack axis. The spectra are offset for clarity. Red and green dashed lines indicate the frequency of the charge sensitive vibrations in neutral TCNQ and TTB, respectively.

the method based on bond lenght of Ref. [31], it is found a practically zero value. Once again, using the procedure for estimating ρ, based on the frequency shift of vibrational modes that are sensitive to the molecular charge a more trusted value for ρ can be found [52, 74] . Fig. 5.4 reports the polarized IR spectra of TTB-TCNQ in the spectral regions of the charge sensitive vibrations. The rightmost panel shows the frequency range of the CT transition, and will be discussed separately. The continuous black line in the Figure represents the absorption spectrum polarized perpendicularly to the stack, where the in-plane charge sensitive vibrations occur. Red and green dashed lines on top of the spectra indicate the frequency of the charge sensitive vibrations in neutral TCNQ and TTB, respectively, showing at a glance that TTB-TCNQ is well on the neutral side. The assessment of the actual ρ, value is however difficult in the present case In fact, the CN stretching frequency, occurring at 2218 cm^{-1}, indicates ρ= 0.2, but the CN stretching frequency is known to give unreliable, generally overestimated, ρ values [33]. On the other hand, the TCNQ $b_{1u}\nu_{20}$ C=C antisymmetric stretching is very close to the analogous vibration of TTB $a_u\nu_{36}$: In neutral TCNQ and TTB they occur at 1545 [32] and at 1524 cm^{-1} (Table S1), respectively. In this spectral region TTB-TCNQ exhibits an absorption with a complex structure, with several peaks. If we attribute the main peak, at 1540 cm^{-1}, to the TCNQ vibration, we find $\rho = 0.1$ but the frequency of the TTB mode is not safely identified. Finally, the C-S antisymmetric stretch of TTB is located at 850 cm^{-1}, slightly upward in respect to the neutral molecule, as expected, but its precise calibration and actual ionization frequency shift are presently not known. The Raman spectra, shown in Fig. 5.5, confirms that TTB-TCNQ is well on the neutral side, as the observed frequencies are very close to the ones of the neutral molecules - the effect of the interaction of the totally symmetric modes with the CT transition is small when ρ is close to 0 or 1 [75]. To summarize, from vibrational spectra we estimate the degree of CT of TTB-TCBQ around 0.1, with a rather large

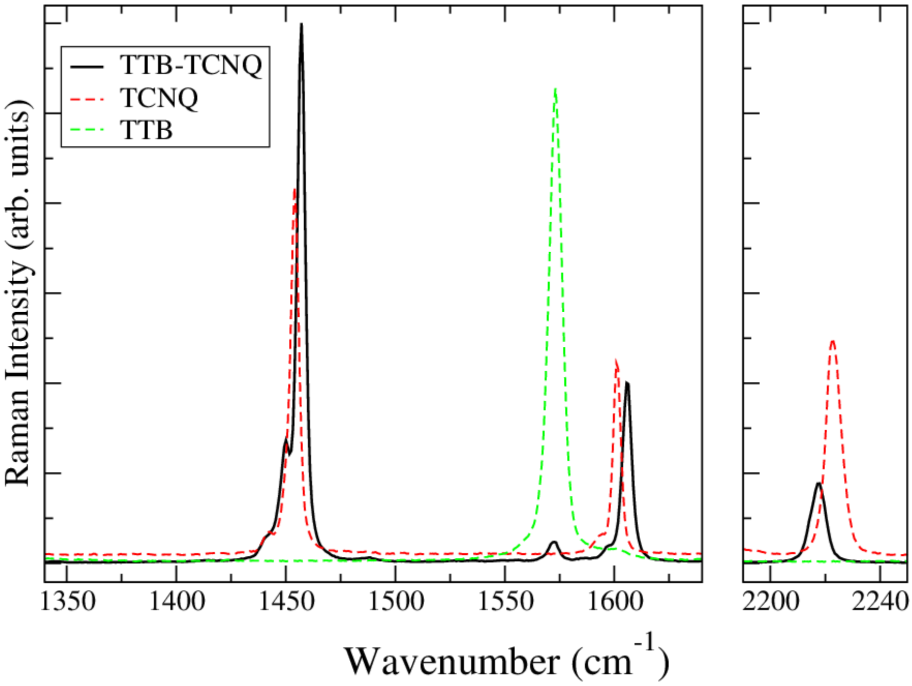

Figure 5.5: Raman spectrum of TTB-TCNQ (black line) in the spctral region of the frequency sensitive modes. The Raman spectra of neutral TCNQ (dashed red line) and of TTB (dashed green line) are also shown for comparison. Exciting line: 676 nm.

uncertainty (± 0.06).

The absorption spectrum in the leftmost panel of Fig. 5.4, with polarization along the stack axis, locates the CT transition of TTB-TCNQ. We explicitly remark that we had problems in recording this part of the spectrum, since the samples are relatively thick, of prismatic shape, and quite often geminated. We attempted to obtain reflectance spectra, but the reflectivity is low and distorted by multiple internal reflections. The absorption spectrum of Fig. 5.4 clearly saturates in this spectral region, and the absorbance cannot be compared with that of the other two panels in the Figure. Nevertheless, the spectrum allows to estimate the frequency of the CT transition at about 7000 cm^{-1}, or 0.87 eV. From the frequency of the CT transition, the above guess of ρ, and the model calculation of Ref. [57], we can estimate the value of the DA hopping or CT integral, t, as 0.16 eV.

The hosting group has recently developed a method to estimate relevant model parameters of mixed stack CT crystals via density-functional theory calculations [48]. Briefly, one calculates the singlet and triplet lowest energy states for an isolated DA pair by keeping the geometry fixed at the one found from the X-ray analysis of the crystal. From these results one can evaluate t and z, half the energy required to form an ionic pair. Furthermore, from the calculation of the charge distribution of both D and A in the neutral and fully ionized state, one calculates V, the DA intermolecular Coulomb potential, and M, the Madelung energy. In the present case, we find $t = 0.21$ eV, in satisfactory agreement with the above experimental estimate, and $z = 0.48$ eV. Moreover, $V = -1.92$ eV and $M = -0.97$ eV. If we compare these values with those obtained for the 11 mixed stack CT crystals considered in Ref. [48], we see that t is on the lower side of the spanned values, and z reflects the TTB ionization potential. The Madeleng energy, on the other hand, is among the smallest in the series, a fact that explains why TTB-TCNQ charge transfer in the crystal is well on the neutral side.

5.2 Conclusions

In summary, an old, little studied electron donor and its mixed stack CT crystal with TCNQ have been characterized. Whereas TTB ionization potential is not dramatically higher than that of TTF, the degree of CT in TTB-TCNQ is low. This fact is probably due to the molecular arrangement of the molecules within the crystal, which is a compromise between the overlap between the frontier orbitals of the two molecules and the steric hindrance. TTB and TCNQ long axes are almost perpendicular one another, and this makes the 3D packing and density rather unfavorable, hence a Madelung energy lower than in other CT crystals. At the same time the CT integral is rather small, but the gap, as estimated by the optical gap, is below 1 eV: According to the experiments by Tsutsumi et al. [76], TTB-TCNQ may exhibit good photocarrier generation and transport. In any case, it is worthwhile to investigate the CT complexes of TTB with other electron acceptors which might provide a better overlap and three-dimensional packing.

Chapter 6

Quinacridone polymorphs

6.1 Introduction

Quinacridone, (5,12-dihydro-quino[2,3-b]acridine-7,14-dione, QA) known with the commercial name of violet 19, is a common pigment used in the dye industry with many derivatives also commercially available. The β-phase is reddish violet whereas the γ-phase is red. Both phases are used for the coloration of lacquers and paints, plastics and printing inks. In solution QA is yellow. QA has also recently revealed important features as semiconductor, attracting attention for its potential application in the "green" organic electronics [8]. Significantly, QA showed better performances than pentacene, of which QA can be considered the H-bonded analogue (see Fig. 6.1): photo-induced charge generation in single-layer QA metal-insulator-metal diodes is more than a hundred times more efficient [77], and QA OFET showed much larger operation stability in air [78].

Difficulties in growing good quality single crystals (see Subsection 1.3.6) and in the identification of the exact crystalline phase is an issue that concerns also the implementation of electronic devices. This prompted us to to undertake a detailed spectroscopic characterization of the phases of QA. As explained in detail in Subsection 1.3.6, many efforts have been done to obtain good quality samples of the various phases, notably the β and γ ones. Even if this work is still not completed, we believe we have singled out these two phases, whereas the work on the other ones is still in progress.

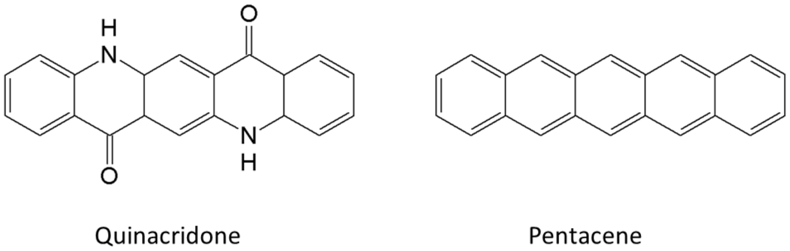

Figure 6.1: Chemical formula of Quinacridone and pentacene

6.2 IR spectra

IR spectra provide the most significant elements for phase recognition. Fig. 6.2 reports the experimental polarized IR spectra recorded for the two samples obtained with two different growth methods, i. e. via closed-tube PVT (c-PVT phase) and via open-tube PVT (o-PVT phase) as described in Subsection 1.3.6. The spectra are polarized along the extinction directions found rotating the samples under an optical microscope using crossed polarisers. The extinction directions were difficult to find in the case of c-PVT due to the irregular, possibly geminated, nature of many of the crystals. These directions are arbitrarily labelled 45° and 135°. For the o-PVT sample extinction direction were easily identified thanks to the more regular, elongated shape of such crystals. These are labelled as 0° (or $\perp$) and 90° (or $\parallel$). Images of the two samples used for measurement can be seen in Fig. 1.14. The c-PVT phase shows no significant variations in the features of the IR absorption in the two directions, as can be seen from the top panel of Fig. 6.2. On the contrary, o-PVT phase presents dramatic changes in the two different polarizations. Between 2900 and 3300 cm^{-1}, corresponding to the region of NH stretching, an intense group of bands appears in the perpendicular polarization, while no absorption at all is present in the same region in parallel polarization. Also in the range 1200-1650 cm-1 significant differences can be detected, the most remarkable being the two peaks at 1594 and 1342 cm^{-1}. Such features can be ascribed to the CO stretching and to NH and CH (bending). All these vibrational modes concern atoms involved in intermolecular H-bonds and provide a useful hint for phase identification.

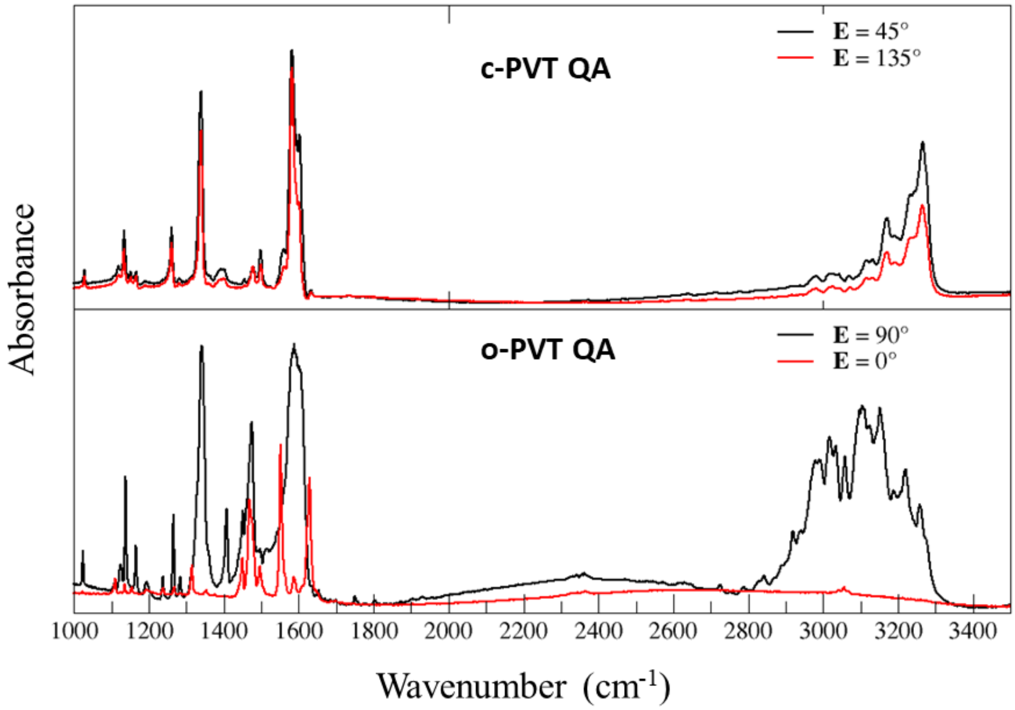

Figure 6.2: Polarized IR spectra of c-PVT (top panel) and o-PVT QA (bottom panel).

By observing the crystalline structures of β and γ QA taken from Ref. [20] (CCDC: 620258, 620259) and reported in Fig. 6.3, one can observe how the frameworks formed by H-bond are different in the two phases: In β QA, each molecule

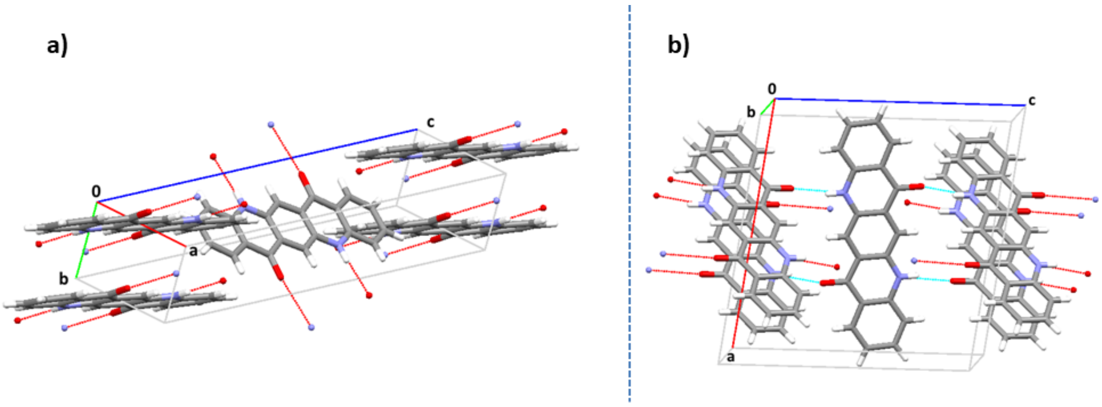

Figure 6.3: Crystalline structure of β-QA (a) and γ-QA (b) taken from Ref [20]. Intermolecular H-bonds are depicted to highlight the resulting framework

is bonded trough two H-bonds, to the nearest two neighboring molecules forming chains. The so formed chains are not parallel, but half of the chains run in the [110] direction, the other half in the [$1\bar{1}0$]. As a consequence H-bonds develop perpendicularly to these two directions (see Fig. 6.3a). In γ-QA instead, each molecule is connected by single hydrogen bonds to four neighboring molecules. Therefore in γ-QA the molecules are not arranged in chains, but form a criss-cross pattern and H-bond network develops along a unique direction (see Fig. 6.3b).

The different H-bond frameworks explains the differences observed in the polarized IR spectra of c-PVT and o-PVT. In fact the features of the spectra of o-PVT QA in the bottom panel of Fig. 6.2 can be ascribed to absorptions in a direction parallel to H-bonds (the c axis) in the 90° polarization (black line), and absorptions in a direction perpendicular to the H-bonds in the 0° polarization (red line). This is coherent with the γ phase structure. On the opposite, the corresponding features of the c-PVT phase (top panel of Fig. 6.2) fit nicely what expected for the β phase, in which H-bonds pattern is similar in the two different directions. A confirmation of the above finding is provided by the comparison of our spectra with the spectra

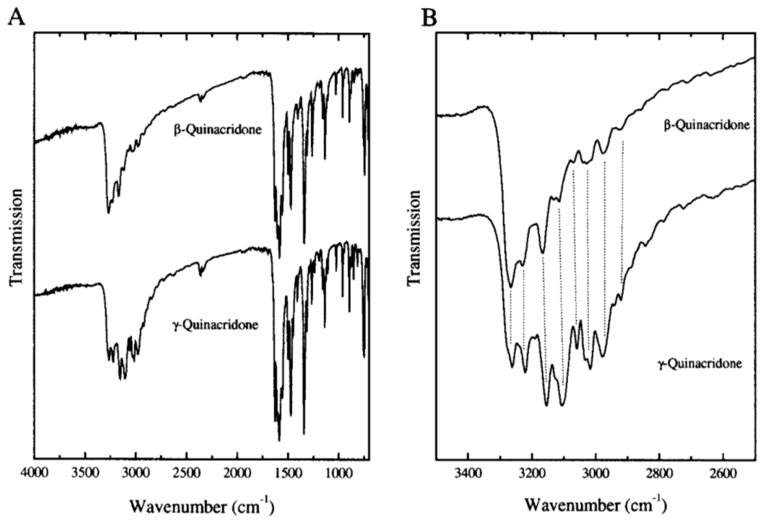

Figure 6.4: IR absorption spectra of β and γ-QA powders dispersed in CCl_4 (From Ref. [79])

available in literature. In fact IR spectra for powders of β and γ-QA were reported by Oliveira [80] and by De feyter [79]. In Fig. 6.4 IR spectra of powders of β and γ-QA dispersed in CCl_4 are reported (taken from ref. [79]). In these spectra the only part that clearly changes from one phase to the other is the one in the range of NH stretching (2900-3300 $cm{-}1$). A very good agreement can be found with the characteristics of our spectra in the same spectral range. The same asymmetric shape of the band can be found in our c-PVT spectra, and the same symmetric shape of the γ-phase bands can be found in the 90° polarized spectrum of our o-PVT spectra. Our polarized data allow to better understand the origin of the difference.

6.3 Raman Spectra

So far it has not been possible to obtain good Raman spectra for β-QA due to a strong fluorescence emission that prevails over Raman signal. A complete Raman characterization of γ-QA has instead been obtained. Polarized Raman spectra (676 nm exciting line) are reported in Fig. 6.5. Raman spectra in the low energy region for the same QA-phase were recorded with the 752 nm exciting line. Spectra are reported in Fig. 6.6 and show the presence of 6 lattice-modes. (One of them is visible at 102 cm^{-1} in the $\perp\perp$ polarization spectra of Fig. 6.5). Six is indeed the number of lattice modes expected for the γ-phase, characterized by 2 molecules in the unit cell.

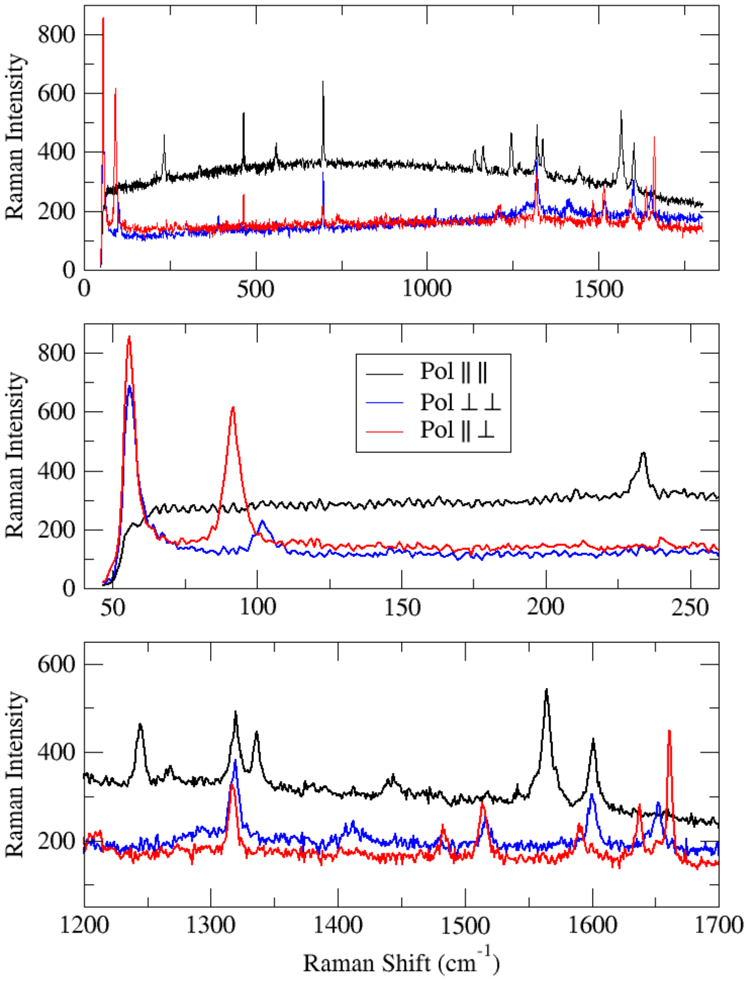

Figure 6.5: Polarized Raman spectra of o-PVT phase

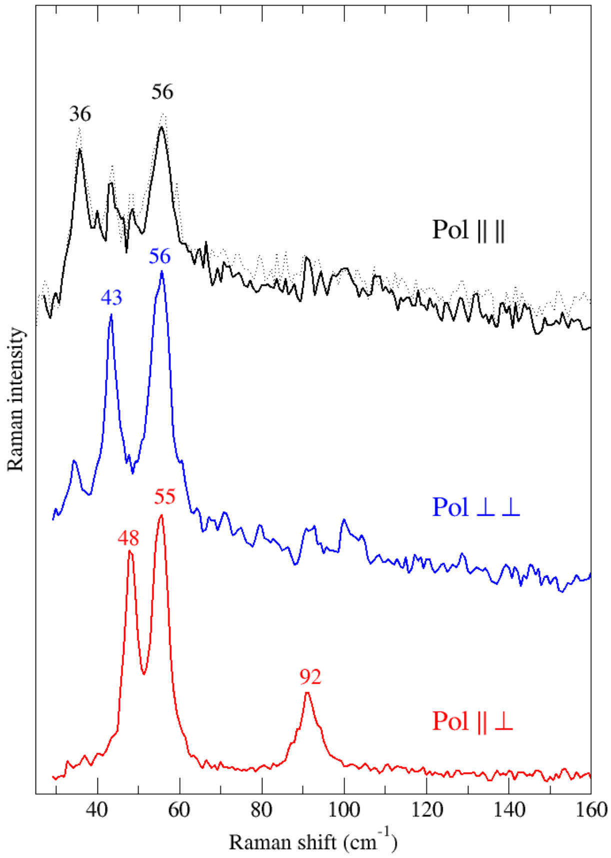

Figure 6.6: Polarized Raman spectra of o-PVT phase in the spectral region of reticular phonons

6.4 UV-Vis Spectra

It was also possible to register the polarized UV-Vis absorption spectra on the same single crystal for γ-QA by the use of a UV-Vis spectrometer coupled to an optical microscope. As can be seen from Fig. 6.7 the spectrum polarized in the parallel direction saturates in the 450-600 nm range, while a well defined absorption profile is found in the perpendicular direction of polarization. Further investigation are needed to understand these features.

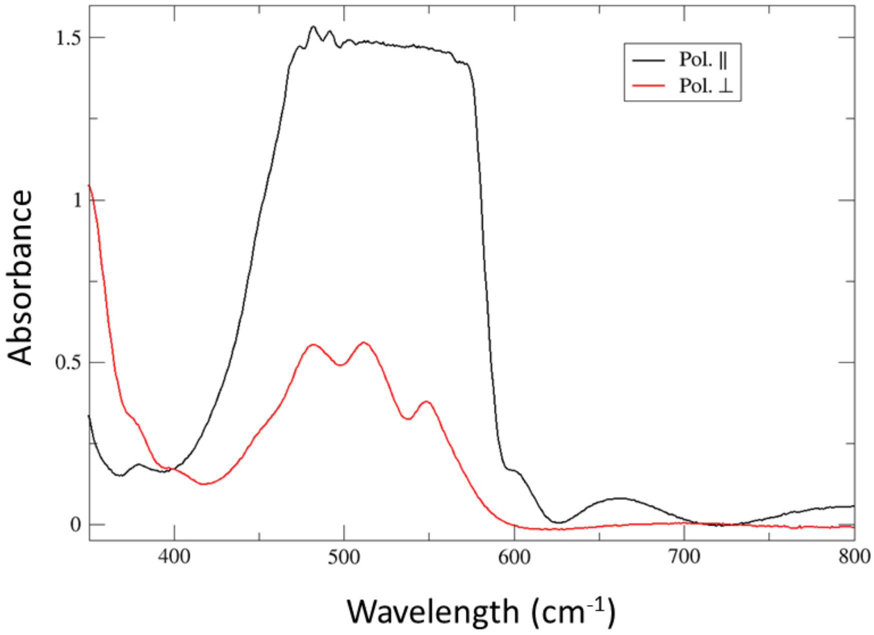

Figure 6.7: Polarized Uv-Vis spectra of o-PVT QA

6.5 Looking ahead

The preliminary work presented in this chapter has provided solid evidences of a precise and rational spectroscopic identification of the γ and β phases of QA. Obtaining one or the other phase is likely connected to the growth methods: Closed-tube PVT at higher temperature yields β-QA, while by open-tube PVT at lower temperature γ-QA is obtained. This could be consistent with the fact that β-QA is more dense (3 %) and less stable than γ-QA [20], so that a higher vapour pressure is needed to grow crystals (higher growth temperature). Further efforts aimed at the optimization of the growth process, in order to achieve single crystals of better quality, particularly of β-QA would be beneficial. In addition, a spectral identification of the α phases is still lacking, and the presence of additional phases cannot be excluded.

Appendices

Appendix A

Experimental and computational methods

A.1 Diffraction measurements

The X-ray diffraction characterization of the high temperature phase of TMB-TCNQ has been done by Dr. G. Kociok-Köhn by the Chemical Characterisation and Analysis Facility (CCAF) of the University of Bath (UK). The crystal diffraction intensity data were collected at 230 K on an Agilent SuperNova-E Dual diffractometer equipped with an Oxford Cryosystem, using CuKα radiation (λ = 1.5418 Å). Data were processed using the CrysAlisPro software.

All the other diffraction measurements have been executed at "Laboratorio di Stutturistica Mario Nardelli" dell'Universitá di Parma by Prof. C. Rizzoli or by Dr. F. Mezzadri.

For the low temperature phase determination of TMB-TCNQ, single crystal diffraction data were collected on a Bruker Smart diffractometer equipped with an APEX II CCD detector using Mo Kα radiation. Temperature control was achieved thanks to an Oxford Cryosystems cryostream, cooling/heating rate was set to 50°/h. Data reduction was carried out by using the SADABS program. Temperature dependent lattice parameters determination was carried out collecting X° of three nonplanar sections of the reciprocal space, so that N reflections were available for unit cell indexing and refinement. (F. Mezzadri)

For all the other sample, single crystals were mounted on a Bruker SMART 1000 CCD diffractometer equipped with graphite monochromated Mo Kα radiation (λ)= 0.71073 Å) finefocus sealed tube. The intensity data were collected using ω scan at 295(2) K. Cell refinements and data reductions were performed using the Bruker SAINT software . The structures were solved by direct methods using the program SIR97 . The molecular graphics were prepared using Mercury 3.9 and Jmol programs. (C. Rizzoli)

A.2 Spectroscopic measurements

The spectroscopic measurements have been executed with the instrumentation of the hosting laboratory. The infrared (IR) spectra were recorded with a Bruker IFS66 Fourier transform IR (FT-IR) spectrometer coupled to the Hyperion 1000

IR microscope. The instrument set-up allows for reflection and transmission measurements with polarized light, and we used both the techniques depending on the crystal thickness and surface quality.

The Raman spectra, excited with the lines of a Lexel Kr laser, have been recorded with a Renishaw 1000 Raman spectrometer, equipped with the appropriate edge filter, and coupled to a Leica M microscope. A small liquid nitrogen cryostat (Linkam HFS 91) has been used for the low-temperature optical measurements under the microscopes.

The UV-visible polarized absorption spectra of γ-QA (350-800 nm range, step 1 nm) were collected with a Zeiss MPM03 microspectrophotometer equipped with 10X strain-free ultrafluar-pol objectives and Glan-Thompson-type polarizing prisms to produce linearly polarized light (ratio of transmitted light between parallel and crossed polarizers of >8000:1). The microscope stage was at room temperature. These measurements were performed by, or under the supervision of L. Ronda, and thanks to the collaboration with A. Mozzarelli, from the Department of Medicine and Surgery of the university of Parma.

A.3 Computational methods

Density Functional methods (DFT, GAMESS package, B3LYP functional, 6-31G(d) basis set) have been used for the equilibrium geometry and molecular vibrations of the isolated molecules. A semi-empirical approach (MOPAC16 package [44], PM7 parametrization) has been adopted for for the calculation of the equilibrium structure of the TMB-TCNQ crystal.

For the calculations of DA and crystal parameter at the experimental geometry our laboratory has used the DFT method as implemented in the Gaussian09 package [70]. All calculations have been performed in vacuum using the unrestricted ωB97XD hybrid functional together with the 6-31+G* basis set. The average charge residing on the D and A molecules is estimated on the basis of the computed Hirshfeld atomic charges. Intermolecular charge transfer integrals have been also calculated directly by using ADF [69], with TZP basis and GGA:PBE functional. The electrostatic interaction V within a DA pair and the Madelung energy M are computed by adopting the point-charge approximation of the molecular charge density based on ESP atomic charges computed for neutral and charged molecules and lattices. The crystal electrostatic sums have been obtained for finite clusters of increasing size using the MESCAL code [81]. Computational calculation were performed mainly by A. Girlando.

Appendix B

Computed vibrational frequencies of TMB, TTB and their ions

The N,N-Tetramethylbenzidine (TMB) and TTB molecules and their ions are not very well characterized in the literature. Here we report the results of DFT calculations, with B3LYP functional, 631G(d) basis set, and unrestricted Hartree-Fock for both the neutral molecules and the ions.

B.1 N,N-tetramethylbenzidine (TMB)

The first question concerns the equilibrium geometry. In the CT-crystals, the two benzene rings are co-planar, whereas the NH_2 group is slightly piramidal, with a CC-NH dihedral angle of 11.7 . The computed equilibrium geometry of the neutral TMB molecules has a CC-NH angle of 27.4 deg, which however reduces to 0 deg (planar NH_2) in TMB^+. Moreover, in the free molecule the two benzene rings are not coplanar, with torsional angle of 36.8 deg and 27.4 deg for TMB and TMB^+, respectively. On the other hand, the energy difference between the co-planar and twisted benzenes is small, about 0.02 eV, which is easily overcome by the packing energy. We have therefore decided not to break the molecular symmetry of the solid state, and adopted the symmetry group C_i (co-planar benzene ring and pyramidal NH_2). In calculating the normal modes, we then get an imaginary torsional frequency of 50.0 and 33.7 cm^{-1} for TMB and TMB^+, respectively.

The vibrational degrees of freedom of TMB are 108. In the C_i symmetry group, they divide into 54 a_g, Raman active, and 54 b_u, infrared active. The computed scaled frequencies of TMB and TMB^+ (scale factors: 0.9679 and 1.0100, for frequencies above and below 1300 cm^{-1}, respectively[74]) are reported in Table B.1.

Table B.1: Scaled calculated frequencies (cm^{-1}) of TMB and TMB$^+$ (C_i symmetry). Calculated intensities (D^2 Å^{-2} amu^{-1}) are reported for the a_u infrared active modes only.

	TMB	TMB$^+$		TMB		TMB$^+$	
Label	ω_{scaled}	ω_{scaled}	Label	ω_{scaled}	IR intensity	ω_{scaled}	IR intensity
a_g ν_1	3530.4	3598.8	a_u ν_{55}	3530.4	0.41779	3598.8	2.77362
ν_2	3437.2	3495.2	ν_{56}	3437.1	0.50137	3491.8	24.98417
ν_3	3105.4	3137.7	ν_{57}	3104.5	1.01748	3136.7	0.33362
ν_4	3085.6	3116.0	ν_{58}	3086.6	0.31688	3116.0	0.14859
ν_5	3023.1	3043.2	ν_{59}	3023.0	0.49294	3043.2	0.27901
ν_6	3022.8	3043.1	ν_{60}	3022.9	0.77637	3043.1	0.07938
ν_7	2963.1	2982.9	ν_{61}	2963.1	2.29281	2983.0	1.00185
ν_8	2962.9	2982.8	ν_{62}	2962.9	0.22864	2982.8	0.02199
ν_9	2914.6	2936.0	ν_{63}	2914.3	2.99513	2935.7	1.29607
ν_{10}	2913.6	2935.4	ν_{64}	2913.6	1.94899	2935.5	0.54916
ν_{11}	1644.2	1645.3	ν_{65}	1645.3	4.06584	1642.3	24.09294
ν_{12}	1605.1	1608.9	ν_{66}	1613.7	0.06143	1614.5	3.51071
ν_{13}	1589.7	1530.6	ν_{67}	1584.7	0.07058	1545.0	0.47363
ν_{14}	1512.7	1511.6	ν_{68}	1493.2	3.74267	1488.4	6.61695
ν_{15}	1488.0	1490.9	ν_{69}	1485.4	0.57900	1484.8	0.47282
ν_{16}	1467.0	1465.9	ν_{70}	1466.7	0.00412	1465.5	0.00003
ν_{17}	1465.7	1464.8	ν_{71}	1466.0	0.59139	1465.2	1.03084
ν_{18}	1460.8	1456.1	ν_{72}	1446.7	5.31853	1436.4	17.46583
ν_{19}	1444.5	1452.7	ν_{73}	1397.2	0.03036	1425.2	0.11473
ν_{20}	1396.2	1403.5	ν_{74}	1395.3	0.00835	1398.0	0.07044
ν_{21}	1394.8	1398.6	ν_{75}	1391.2	0.01260	1396.7	2.44405
ν_{22}	1325.9	1383.5	ν_{76}	1323.9	0.00015	1333.4	2.15630
ν_{23}	1315.3	1338.5	ν_{77}	1290.1	0.38390	1322.6	0.13343
ν_{24}	1281.0	1322.2	ν_{78}	1276.4	1.75825	1276.5	0.00002
ν_{25}	1266.1	1266.1	ν_{79}	1269.0	0.48003	1268.6	4.20405
ν_{26}	1217.4	1230.8	ν_{80}	1193.7	0.12803	1156.5	0.26216
ν_{27}	1188.0	1151.9	ν_{81}	1138.2	0.78661	1114.9	3.18293

Table 1 (continued)

	TMB	TMB$^+$		TMB		TMB$^+$	
Label	ω_{scaled}	ω_{scaled}	Label	ω_{scaled}	IR intensity	ω_{scaled}	IR intensity
a_g ν_{28}	1084.3	1085.0	a_u ν_{82}	1083.4	0.00434	1083.5	0.00001
ν_{29}	1079.3	1081.2	ν_{83}	1080.3	0.14168	1082.7	0.17940
ν_{30}	1055.5	1063.4	ν_{84}	1053.8	0.29911	1050.3	0.30923
ν_{31}	1049.6	1048.7	ν_{85}	1022.8	0.32106	1015.5	0.18163
ν_{32}	985.8	976.9	ν_{86}	954.7	0.03404	932.0	0.02740
ν_{33}	962.6	939.3	ν_{87}	889.0	0.92941	909.6	0.85468
ν_{34}	898.4	891.1	ν_{88}	856.9	0.22238	861.7	0.00000
ν_{35}	878.8	892.2	ν_{89}	850.2	0.00123	857.3	0.07879
ν_{36}	794.5	750.6	ν_{90}	749.4	1.51542	748.0	0.08966
ν_{37}	746.9	660.1	ν_{91}	696.4	0.35911	697.3	0.01558
ν_{38}	668.7	588.6	ν_{92}	646.9	16.77243	576.9	0.16420
ν_{39}	637.9	560.4	ν_{93}	587.4	0.06717	575.0	0.00055
ν_{40}	591.5	538.1	ν_{94}	575.2	2.43287	557.9	0.00001
ν_{41}	553.4	527.0	ν_{95}	506.1	0.04485	502.7	0.00493
ν_{42}	533.6	449.0	ν_{96}	497.1	1.12603	487.1	1.76175
ν_{43}	511.8	367.1	ν_{97}	494.9	0.00389	438.0	0.00000
ν_{44}	388.9	356.8	ν_{98}	360.3	0.56761	351.6	0.08135
ν_{45}	363.2	329.3	ν_{99}	322.6	0.33260	325.2	9.91372
ν_{46}	326.4	323.7	ν_{100}	307.9	0.57183	320.5	0.00180
ν_{47}	317.0	232.7	ν_{101}	300.4	0.08416	303.5	0.01687
ν_{48}	266.7	270.9	ν_{102}	213.0	0.11166	237.9	0.00000
ν_{49}	236.6	240.0	ν_{103}	199.5	0.02831	205.8	0.13254
ν_{50}	227.9	234.1	ν_{104}	178.2	0.09146	192.2	0.00000
ν_{51}	209.2	215.3	ν_{105}	137.2	0.02084	125.2	0.01244
ν_{52}	183.5	192.8	ν_{106}	105.7	0.02053	109.9	0.02353
ν_{53}	179.1	179.8	ν_{107}	57.3	0.06583	51.8	0.13550
ν_{54}	113.2	97.1	ν_{108}	50.0	0.00718	33.7	0.00000

B.2 1,1,4,4-tetrathiabutadiene (TTB)

The minimum energy conformation of neutral and ionic TTB in gas phase has C_i symmetry, with a planar central skeleton and out-of-plane staggered arrangement of the terminal CH_2-CH_2 groups. Group theory predicts 30 vibrational modes IR active. The experimental scaled and unscaled frequencies of TTB and TTB^+ are reported in Table B.2.

Table B.2: Experimental, scaled and unscaled calculated frequencies (ω, cm^{-1}) of TTB and TTB$^+$ (C_i symmetry). Calculated intensities (D^2 Å^{-2} amu^{-1}) are reported only for a_u IR active modes.

	TTB			TTB$^+$	
Label	$\omega_{\text{exp.}}$	$\omega_{\text{scal.}}$	$\omega_{\text{unscal.}}$	$\omega_{\text{scal.}}$	$\omega_{\text{unscal.}}$
$a_g\nu_1$		3042.1	3164.3	3049.9	3172.3
ν_2		3020.3	3141.6	3041.7	3163.8
ν_3	2992	3007.3	3128.0	3030.6	3152.3
ν_4	2969	2962.3	3081.2	2978.0	3097.6
ν_5	2921	2959.3	3078.1	2976.7	3096.2
ν_6	1573	1591.6	1655.5	1541.6	1603.5
ν_7		1450.1	1508.4	1447.3	1505.5
ν_8		1438.8	1496.6	1434.8	1492.4
ν_9	1318	1308.4	1360.9	1290.5	1342.3
ν_{10}	1307	1283.8	1335.3	1289.5	1341.2
ν_{11}	1245	1246.6	1296.6	1255.2	1305.6
ν_{12}	1162	1149.1	1195.3	1223.4	1272.5
ν_{13}	1143	1134.5	1180.0	1149.8	1195.9
ν_{14}		1095.1	1139.0	1099.9	1144.0
ν_{15}	955	954.4	992.7	963.6	1002.3
ν_{16}	931	948.4	986.5	959.7	998.2
ν_{17}		895.9	931.9	939.3	977.0
ν_{18}		845.8	879.7	839.7	873.4
ν_{19}	822	811.1	843.6	828.8	862.1
ν_{20}	684	663.5	690.1	676.4	703.6
ν_{21}		655.5	681.8	645.6	671.5
ν_{22}		643.5	669.3	638.0	663.6
ν_{23}	480	466.5	485.2	463.4	482.0
ν_{24}	463	443.2	461.0	457.7	476.0
ν_{25}	444	427.9	445.1	431.4	448.8
ν_{26}	299	291.7	303.4	244.7	254.5
ν_{27}	229	242.4	252.1	219.2	228.0
ν_{28}		215.9	224.5	216.9	225.6
ν_{29}	155	148.4	154.4	154.9	161.2
ν_{30}		44.7	46.5	89.5	93.1

Table B.2 (continued)

	TTB				TTB$^+$		
Label	$\omega_{\text{exp.}}$	$\omega_{\text{scal.}}$	$\omega_{\text{unscal.}}$	IR int.	$\omega_{\text{scal.}}$	$\omega_{\text{unscal.}}$	IR int.
$a_u\nu_{31}$		3051.1	3173.6	0.13979	3058.8	3181.7	0.06192
ν_{32}	3003	3020.3	3141.6	0.54849	3041.7	3163.8	0.00219
ν_{33}	2956	3007.3	3128.0	0.15225	3030.6	3152.3	0.00287
ν_{34}	2920	2962.2	3081.1	1.62965	2978.1	3097.6	0.07510
ν_{35}		2959.4	3078.2	0.52615	2976.7	3096.2	0.04336
ν_{36}	1524	1541.4	1603.2	4.34586	1447.2	1505.3	0.15533
ν_{37}		1450.0	1508.2	0.00306	1434.9	1492.5	0.55480
ν_{38}	1415	1438.8	1496.5	0.24332	1380.1	1435.5	12.49079
ν_{39}	1273	1282.3	1333.8	2.27983	1290.0	1341.8	0.13625
ν_{40}		1270.1	1321.1	0.81498	1285.5	1337.1	6.52965
ν_{41}	1241	1242.3	1292.2	0.24307	1250.6	1300.8	0.56710
ν_{42}	1147	1140.0	1185.7	0.08545	1150.4	1196.6	0.86802
ν_{43}	1104	1095.4	1139.4	0.11832	1100.1	1144.2	0.05113
ν_{44}	975	954.2	992.5	0.25573	963.5	1002.1	0.23410
ν_{45}		947.3	985.3	0.01378	950.3	988.4	0.19009
ν_{46}	845	868.6	903.5	0.26638	909.5	946.0	2.53659
ν_{47}	834	831.5	864.9	1.15079	886.6	922.2	0.76855
ν_{48}		818.6	851.5	0.58594	838.6	872.3	0.30940
ν_{49}	682	663.6	690.3	0.03844	647.4	673.4	0.03556
ν_{50}		654.6	680.9	0.33384	639.9	665.6	1.01749
ν_{51}		550.9	573.0	0.85310	578.3	601.5	1.66569
ν_{52}		471.3	490.2	0.04412	513.4	534.0	0.04378
ν_{53}		449.2	467.2	0.13030	454.1	472.3	0.01359
ν_{54}		405.2	421.5	0.04778	426.2	443.3	0.18401
ν_{55}		401.6	417.7	0.30074	399.7	415.8	0.22625
ν_{56}		243.3	253.1	0.16083	217.9	226.7	0.20193
ν_{57}		94.6	98.4	0.03493	149.2	155.2	0.05791
ν_{58}		62.6	65.1	0.02683	65.4	68.0	0.01564
ν_{59}		34.7	36.1	0.16329	50.7	52.8	0.12389
ν_{60}		31.7	33.0	0.02761	34.4	35.8	0.00097

Conclusions

In the present Thesis we have prepared and characterized several molecular crystals with perspective applications in the field of organic electronic devices. In this field, crystal growth is one of the key issues. Solid state properties in fact depend on the molecular packing and crystal perfection, avoiding both chemical and physical impurities, the latter due to the possible presence of different polymorphs in the same crystallite [10]. Therefore, a great part of the Thesis work has been devoted to the crystal growth. The main techniques employed in order to obtain samples of optimal quality has been extensively described in Chapter 1. Different techniques have indeed been employed and refined during the Thesis, building on the progressively gained experience. Starting with the most common solution based techniques, other methods, in particular vapour phase methods, have been introduced in the guest group and successfully exploited.

The development of vapor phase methods has actually been the key for the growth of crystals of different polymorphs of Quinacridone (Chapter 6). Quinacridone, a well known bio-compatible die, has been proposed as a good semiconductor, but it displays many different polymorphic forms and mixed phases [20]. The Thesis work has started with attempt to crystallize Quinacridone, but at the time was unsuccessful. Only after perfecting the crystal growth by vapour phase it has been possible to obtain and precisely characterize the two most important polymorphs of Quinacridone, β and γ, the former grown by the closed tube method, and the second by the open tube. Actually, this goal has been achieved during the final writing of the Thesis, and for this reason only a brief Chapter has been added at the end. But the results obtained are important and will lead to further developments. In fact, it was believed that the two polymorphs could be obtained by different deposition temperatures, but we have shown that instead the condition of transport are important as well, since we have used comparable temperatures. This open the way to a more precise control of the growth.

The main body of the thesis has been devoted to the study of mixed stack organic CT crystals, which are well known for the so-called Neutral-Ionic phase transition [54], a rather rare transition induced by temperature or pressure, and implying a collective charge migration from Donor to Acceptor molecules. Interest in this class of compounds has been recently resurrected in view of potential applications as ambipolar semiconductors or as ferroelectrics. In the present Thesis we have explored the "phase space" of these compounds, which spans from a neutral to a ionic ground state, with a chain of Donor/Acceptor molecules which can have a constant or alternating intermolecular distance (regular or dimerized stack). We have approached the problem by combining a given Donor molecule with a series of Acceptors of increasing strength, as previously done for instance by combining perylene with TCNQF_X [47].

A first attempt has been done by combining a little known Donor, TTB, with TCNQ (a crystal already available in the guest laboratory) and with $TCNQF_4$. Unfortunately, the growth of crystals of TTB-$TCNQF_4$ did not succeed, so in this case we have limited ourselves to the characterization of TTB-TCNQ (Chapter 5). This complex is almost neutral, despite the fact that TTB has a Donor strength only slightly less than the well known TTF. From our study it emerges that the reason has to be searched in the unfavourable packing of TTB with TCNQ, so the work with this Donor will be prosecuted by combining it with different Acceptors, like Tetracyanoethylene (TCNE).

Two other series of CT crystals have been considered. One is described in Chapter 4, where we describe the CT crystals composed by the donor BTBT and the acceptors $TCNQF_X$ (X=0,2,4). The analogue CT compounds, formed with BTBT alkylated derivatives in place of the simple BTBT, were already investigated and known in literature to show n-type semiconductive character and a basic lack of correlation of the degree of charge transfer with the acceptor strength. The same CT structures were prepared independently from us by Sato et al. [67] who tested them in OTFT . By our spectroscopic measurements it turned out that even for the BTBT-$TCNQF_X$ series the degree of charge transfer doesn't vary significantly passing from BTBT-TCNQ to BTBT-$TCNQF_2$ and BTBT-$TCNQF_4$. Trough extensive first principle calculations we found in the crystal packing a rationale of this behaviour. The presence of the HOMO-1 very close in energy to the HOMO of BTBT, gives rise to a high level of electron delocalization along the stack axis, which reduces the effect of the Madelung energy. The closest contacts between the negatively charged F and N atoms also explains the modest variation of the Madelung energy along the series.

The second and most important series of CT crystals we have considered is that obtained by using Tetramethylbenzidine (TMB) as a Donor molecule. We have started by studying the nature of an already known phase transition displayed by the TMB-TCNQ crystal (Chapter 2). The transition which was classified as a Neutral-Ionic one has now been redefined by us as a “valence shell instability” in which an ionicity jump occurs together with a stack dimerization but without overcoming the Neutral-Ionic borderline. The structure of the (initially unknown) low temperature phase has also been obtained, revealing ferroelectric order. These significant results provide the base for further investigations: if TMB-TCNQ itself doesn't seem to provide more room for practical applications or further investigations (the crystal breaks or is in any case damaged at the transition), future efforts may be dedicated to TMB derivatives coupled with TCNQ. The basic idea is to test the effects of small changes in the donor molecule (e. g. substitution of CH_3 with other alkylic groups) on the eventual phase transition and on the structural stability of the low-temperature phase. In this view TMB-TCNQ has the potential to be a candidate of a new prototypical CT system with possible ferroelectric properties. Inspired by the latter study, we describe in Chapter 3 the results obtained with a series of CT systems formed by TMB, and different acceptors of increasing strength, Chloranil (CA), Bromanil (BA), $TCNQF_2$ and $TCNQF_4$. With the addition of the just mentioned TMB-TCNQ, we have obtained a series of CT crystals whose degree of charge transfer spans from quasi neutral (CA, BA) to quasi ionic values ($TCNQF_2$, $TCNQF_4$). No new Neutral-Ionic phase transitions have been found (at least down to 77 K) nor ferroelectric arrangements. Despite this apparently discouraging outline, some findings deserve more attention and constitute the starting point for further investigations. First of all it will be of interest to perform mobility measurements in order to test the possibility of ambipolar semiconductivity. Moreover, even if TMB-TCNQF$_4$ crystallizes in a centrosymmetric system, the spectroscopic evidence suggests the presence of DA dimers. DA a dimers could be present in a disordered arrangement, with opposite distortion, not detectable by XRD which relies on long-range order. In this case it could be possible to reach a ferroelectric arrangement upon the application of an electric field. Both these lines of investigations are being pursued by the guest group in collaboration with experts of both kind of measurements.

Bibliography

[1] Mizuka Sano. “Studies of Organic Semiconductors for 40 Years - Foreword”. In: *Molecular Crystals and Liquid Crystals Incorporating Nonlinear Optics* 171.1 (1989), pp. v–vi.

[2] M. Schwoerer and H.C. Wolf. *Organic Molecular Solids*. Lehrbuch Physik. Wiley, 2008. ISBN: 9783527618668. URL: `https://books.google.it/books?id=dlr62zMnpToC`.

[3] C.D. Dimitrakopoulos and P.R.L. Malenfant. “Organic Thin Film Transistors for Large Area Electronics”. In: *Advanced Materials* 14.2 (2002), pp. 99–117. ISSN: 1521-4095. DOI: `10.1002/1521-4095(20020116)14:2<99::AID-ADMA99>3.0.CO;2-9`. URL: `http://dx.doi.org/10.1002/1521-4095(20020116)14:2%3C99::AID-ADMA99%3E3.0.CO;2-9`.

[4] Henning Sirringhaus. “25th Anniversary Article: Organic Field-Effect Transistors: The Path Beyond Amorphous Silicon”. In: *Advanced Materials* 26.9 (2014), pp. 1319–1335. ISSN: 1521-4095. DOI: `10.1002/adma.201304346`. URL: `http://dx.doi.org/10.1002/adma.201304346`.

[5] Mihai Irimia-Vladu. ““Green” electronics: biodegradable and biocompatible materials and devices for sustainable future”. In: *Chem. Soc. Rev.* 43 (2 2014), pp. 588–610. DOI: `10.1039/C3CS60235D`.

[6] Lingyun Zhu et al. “Prediction of remarkable ambipolar charge-transport characteristics in organic mixed-stack charge-transfer crystals”. In: *Journal of the American Chemical Society* 134.4 (2012), pp. 2340–2347.

[7] Sachio Horiuchi, Tatsuo Hasegawa, and Yoshinori Tokura. “Molecular Donor–Acceptor Compounds as Prospective Organic Electronics Materials”. In: *Journal of the Physical Society of Japan* 75.5 (2006), p. 051016. DOI: `10.1143/JPSJ.75.051016`. eprint: `https://doi.org/10.1143/JPSJ.75.051016`. URL: `https://doi.org/10.1143/JPSJ.75.051016`.

[8] Eric Daniel Glowacki et al. “Natural and nature-inspired semiconductors for organic electronics”. In: *Proc.SPIE* 8118 (2011), 8118_1–$8118_1$0. DOI: `10.1117/12.892467`. URL: `http://dx.doi.org/10.1117/12.892467`.

[9] Aldo Brillante et al. “Structure and dynamics of pentacene on SiO_2: From monolayer to bulk structure”. In: *Phys. Rev. B* 85 (19 May 2012), p. 195308. DOI: `10.1103/PhysRevB.85.195308`. URL: `https://link.aps.org/doi/10.1103/PhysRevB.85.195308`.

[10] A. Brillante et al. “Characterization of Phase Purity in Organic Semiconductors by Lattice-Phonon Confocal Raman Mapping: Application to Pentacene”. In: *Advanced Materials* 17.21 (2005), pp. 2549–2553. ISSN: 1521-4095. DOI: `10.1002/adma.200501350`. URL: `http://dx.doi.org/10.1002/adma.200501350`.

[11] J. B. Torrance et al. “Discovery of a Neutral-to-Ionic Phase Transition in Organic Materials”. In: *Phys. Rev. Lett.* 46 (4 Jan. 1981), pp. 253–257. DOI: `10.1103/PhysRevLett.46.253`.

[12] J. B. Torrance et al. “Anomalous Nature of Neutral-to-Ionic Phase Transition in Tetrathiafulvalene-Chloranil”. In: *Physical Review Letters* 47.24 (1981), pp. 1747–1750. ISSN: 0031-9007. DOI: `10.1103/PhysRevLett.47.1747`. URL: `https://link.aps.org/doi/10.1103/PhysRevLett.47.1747` (visited on 07/21/2017).

[13] Alberto Girlando et al. “Vibrational spectroscopy of mixed stack organic semiconductors: Neutral and ionic phases of tetrathiafulvalene–chloranil (TTF–CA) charge transfer complex”. In: *The Journal of Chemical Physics* 79.2 (1983), pp. 1075–1085.

[14] “The Neutral-Ionic Phase Transition”. In: *Crystals*. Ed. by A. Painelli and A. Girlando. Vol. 7. MDPI, 2017.

[15] Sachio Horiuchi et al. “Ionic versus Electronic Ferroelectricity in Donor?Acceptor Molecular Sequences”. In: *Chemistry Letters* 43.1 (Jan. 5, 2014), pp. 26–35. ISSN: 0366-7022, 1348-0715. DOI: `10.1246/cl.130840`. URL: `http://www.journal.csj.jp/doi/10.1246/cl.130840` (visited on 07/04/2017).

[16] Hui Jiang and Christian Kloc. “Single-crystal growth of organic semiconductors”. In: *MRS bulletin* 38.1 (2013), pp. 28–33.

[17] RA Laudise et al. “Physical vapor growth of organic semiconductors”. In: *Journal of Crystal Growth* 187.3 (1998), pp. 449–454.

[18] PG Simpkins and KS Chen. “Convection in horizontal cavities”. In: *Journal of Fluid Mechanics* 166 (1986), pp. 21–39.

[19] Y Iwasa et al. “Temperature-induced neutral-ionic transition in tetramethylbenzidine-tetracyanoquinodimethane (TMB-TCNQ)”. In: *Physical Review B* 42.4 (1990), p. 2374.

[20] Erich F Paulus, Frank JJ Leusen, and Martin U Schmidt. “Crystal structures of quinacridones”. In: *CrystEngComm* 9.2 (2007), pp. 131–143.

[21] Naoko Nishimura, Takatoshi Senju, and Jin Mizuguchi. “5, 7, 12, 14-Tetrahydro [2, 3-b] quinolinoacridine (β form)”. In: *Acta Crystallographica Section E: Structure Reports Online* 62.10 (2006), o4683–o4685.

[22] GD Potts et al. “The crystal structure of quinacridone: an archetypal pigment”. In: *Journal of the Chemical Society, Chemical Communications* 22 (1994), pp. 2565–2566.

[23] J Mizuguchi, T Sasaki, and K Tojo. “Refinement of the crystal structure of 5, 7, 12, 14-tetrahydro [2, 3-b]-quinolinoacridine (γ-form), C20H12N2O2, at 223 K”. In: *Zeitschrift für Kristallographie-New Crystal Structures* 217.1 (2002), pp. 249–250.

[24] W. S. Struve. 2844485. 1955.

[25] G Lincke and H-U Finzel. “Studies on the Structure of alpha-Quinacridone”. In: *Crystal Research and Technology* 31.4 (1996), pp. 441–452.

[26] M Buron-Le Cointe et al. “Thermal hysteresis phenomena and mesoscopic phase coexistence around the neutral-ionic phase transition in TTF-CA and TMB-TCNQ”. In: *Physical Review B* 68.6 (2003), p. 064103.

[27] Nicola Castagnetti et al. “Temperature-induced valence instability in the charge-transfer crystal TMB-TCNQ”. In: *Physical Review B* 95.2 (2017), p. 024101.

[28] Kenichi Imaeda et al. “Electronic Properties of 3, 3’, 5, 5’-Tetramethyl-Benzidine Complexes with TCNQ Derivatives”. In: *Molecular Crystals and Liquid Crystals* 141.1-2 (1986), pp. 131–140.

[29] Y Iwasa et al. “Spectroscopic study on (anti) ferroelectric molecular systems”. In: *Molecular Crystals and Liquid Crystals* 216.1 (1992), pp. 195–200.

[30] Th J Kistenmacher et al. “Structure of the red, semiconducting form of 4, 4’, 5, 5’-tetramethyl-Δ2, 2’-bi-1, 3-diselenole-7, 7, 8, 8-tetracyano-p-quinodimethane, TMTSF–TCNQ”. In: *Acta Crystallographica Section B: Structural Crystallography and Crystal Chemistry* 38.4 (1982), pp. 1193–1199.

[31] Peng Hu et al. “Crystal Growth, HOMO–LUMO Engineering, and Charge Transfer Degree in Perylene-F X TCNQ (X= 1, 2, 4) Organic Charge Transfer Binary Compounds”. In: *Crystal Growth & Design* 16.5 (2016), pp. 3019–3027.

[32] Renato Bozio et al. “Influence of the intermolecular charge transfer interaction on the solution and solid state infrared spectra of 7, 7, 8, 8-tetracyanoquinodimethane (TCNQ) alkaline salts”. In: *Journal of the Chemical Society, Faraday Transactions 2: Molecular and Chemical Physics* 74 (1978), pp. 235–248.

[33] Moreno Meneghetti and Cesare Pecile. “Charge–transfer organic crystals: Molecular vibrations and spectroscopic effects of electron–molecular vibration coupling of the strong electron acceptor TCNQF4”. In: *The Journal of chemical physics* 84.8 (1986), pp. 4149–4162.

[34] Antonia Morherr et al. “Crystal growth of new charge-transfer salts based on π-conjugated donor molecules”. In: *Physica B: Condensed Matter* 496 (2016), pp. 98–105.

[35] Matteo Masino, Alberto Girlando, and Zoltan G Soos. “Evidence for a soft mode in the temperature induced neutral-ionic transition of TTF-CA”. In: *Chemical physics letters* 369.3 (2003), pp. 428–433.

[36] A Girlando and C Pecile. “Polarized raman spectra of TCNQ and TCNQ-d4 single crystals”. In: *Spectrochimica Acta Part A: Molecular Spectroscopy* 29.10 (1973), pp. 1859–1878.

[37] R Bozio and C Pecile. *physics and chemistry of low dimensional solids.* NATO Scientific Affairs Division, by L. Alcacers et al., 1980.

[38] C Pecile, A Palnelli, and A Girlando. “Studies of organic semiconductors for 40 years—V”. In: *Molecular Crystals and Liquid Crystals* 171.1 (1989), pp. 69–87.

[39] M Hanfland et al. “Raman study of the pressure-induced neutral-to-ionic transition in tetrathiafulvalene chloranil”. In: *Physical Review B* 38.2 (1988), p. 1456.

[40] Matteo Masino et al. “High-pressure optical study of the neutral–ionic phase transition in TTF-CA”. In: *Materials Science-Poland* 22.4 (2004).

[41] Paolo Ranzieri et al. “Temperature-induced valence and structural instability in DMTTF-CA: Single-crystal Raman and infrared measurements”. In: *Physical Review B* 76.13 (2007), p. 134115.

[42] Aldo Brillante et al. “Probing polymorphs of organic semiconductors by lattice phonon Raman microscopy”. In: *CrystEngComm* 10.8 (2008), pp. 937–946.

[43] M Le Cointe et al. “Symmetry breaking and structural changes at the neutral-to-ionic transition in tetrathiafulvalene-p-chloranil”. In: *Physical Review B* 51.6 (1995), p. 3374.

[44] *title*. 2016. URL: `http://OpenMOPAC.net`.

[45] *Program STRCONVERT*. URL: `http://www.cryst.ehu.es/index.html`.

[46] Zoltán G Soos and Anna Painelli. “Metastable domains and potential energy surfaces in organic charge-transfer salts with neutral-ionic phase transitions”. In: *Physical Review B* 75.15 (2007), p. 155119.

[47] Tommaso Salzillo et al. “Structure, stoichiometry, and charge transfer in cocrystals of Perylene with TCNQ-F x”. In: *Crystal Growth & Design* 16.5 (2016), pp. 3028–3036.

[48] Francesca Delchiaro et al. “Towards first-principles prediction of valence instabilities in mixed stack charge-transfer crystals”. In: *Physical Review B* 95.15 (2017), p. 155125.

[49] V. K. Belsky, O. N. Zorkaya, and P. M. Zorky. “Structural classes and space groups of organic homomolecular crystals: new statistical data”. In: *Acta Crystallographica Section A* 51.4 (1995), pp. 473–481.

[50] A. Girlando and C. Pecile. “Vibrational spectra of fluoranil”. In: *J.Chem. Soc. Faraday II* 71 (1975).

[51] A. Girlando et al. “Raman and infrared frequency shifts proceeding from ionization of perhalo-p-benzoquinones to radical anions”. In: *J.Chem.Phys.* 68 (1978).

[52] Paolo Ranzieri, Matteo Masino, and Alberto Girlando. “Charge-Sensitive Vibrations in p-Chloranil: The Strange Case of the CC Antisymmetric Stretching”. In: *The Journal of Physical Chemistry B* 111.44 (2007), pp. 12844–12848.

[53] A Girlando et al. “Direct evidence of overdamped Peierls-coupled modes in the temperature-induced phase transition in tetrathiafulvalene-chloranil”. In: *Physical Review B* 78.4 (2008), p. 045103.

[54] Matteo Masino, Nicola Castagnetti, and Alberto Girlando. “Phenomenology of the Neutral-Ionic Valence Instability in Mixed Stack Charge-Transfer Crystals”. In: *Crystals* 7.4 (2017), p. 108.

[55] S. A. Bewick et al. In: *J. Chem. Phys.* 122 (2005), p. 024710.

[56] Alexey Kuzmenko. *RefFIT.* `https://sites.google.com/site/reffitprogram/`. Version 1.2.95. 2015.

[57] A Painelli and A Girlando. "Mixed regular stack charge–transfer crystals: Fundamental microscopic parameters from optical spectra". In: *The Journal of chemical physics* 87.3 (1987), pp. 1705–1711.

[58] A. Painelli and A. Girlando. "Zero-Temperature Phase Diagram of Mixed-Stack Charge-Transfer Crystals". In: *Physical Review B* 37.10 (1988), pp. 5748–5760.

[59] Katelyn P. Goetz et al. "Polymorphism in the 1:1 Charge-Transfer Complex DBTTF-TCNQ and Its Effects on Optical and Electronic Properties". In: *Advanced Electronic Materials* (Sept. 2016), p. 1600203.

[60] Alberto Girlando. "Comment on Polymorphism in the 1:1 Charge-Transfer Complex DBTT-TCNQ and Its Effects on Optical and Electronic Properties". In: *Advanced Electronic Materials* 3.3 (Mar. 2017), p. 1600437.

[61] Nicola Castagnetti et al. "Mixed stack organic semiconductors: The anomalous of the BTBT-TCNQFx series". In: *Crystal growth & design* (2017).

[62] Yongbo Yuan et al. "Ultra-high mobility transparent organic thin film transistors grown by an off-centre spin-coating method". In: *Nature communications* 5 (2014), p. 3005.

[63] Yusuke Tsutsui et al. "Charge Carrier Mobility: Unraveling Unprecedented Charge Carrier Mobility through Structure Property Relationship of Four Isomers of Didodecyl [1] benzothieno [3, 2-b][1] benzothiophene (Adv. Mater. 33/2016)". In: *Advanced Materials* 28.33 (2016), pp. 7291–7291.

[64] Henry Méndez et al. "Doping of organic semiconductors: impact of dopant strength and electronic coupling". In: *Angewandte Chemie International Edition* 52.30 (2013), pp. 7751–7755.

[65] Jun'ya Tsutsumi et al. "N-type field-effect transistors based on layered crystalline donor–acceptor semiconductors with dialkylated benzothienobenzothiophenes as electron donors". In: *Journal of Materials Chemistry C* 3.9 (2015), pp. 1976–1981.

[66] Yosei Shibata et al. "Unidirectionally Crystallized Stable n-Type Organic Thin-Film Transistors Based on Solution-Processable Donor–Acceptor Compounds". In: *Advanced Electronic Materials* (2017).

[67] Ryonosuke Sato et al. "Charge-Transfer Complexes of Benzothienobenzothiophene with Tetracyanoquinodimethane and the n-Channel Organic Field-Effect Transistors". In: *The Journal of Physical Chemistry C* 121.12 (2017), pp. 6561–6568.

[68] A Chernenkaya et al. "Microscopic origin of the charge transfer in single crystals based on thiophene derivatives: A combined NEXAFS and density functional theory approach". In: *The Journal of chemical physics* 145.3 (2016), p. 034702.

[69] *SCM,* URL: `http://www.scm.com.`.

[70] MJ Frisch et al. "GAUSSIAN09, Gaussian, Inc., Wallingford, CT, USA,(2009)". In: *Google Scholar* (2016).

[71] Tohru Nishinaga. *Organic Redox Systems: Synthesis, Properties, and Applications.* John Wiley & Sons, 2015.

[72] Kaname Kanai et al. “Determination of electron affinity of electron accepting molecules”. In: *Applied Physics A* 95.1 (2009), pp. 309–313.

[73] Daniel J Sandman et al. “Synthesis, electronic structure, and complex formation of simple 1, 1, 4, 4-tetrathiabutadienes”. In: *Journal of the Chemical Society, Chemical Communications* 16 (1981), pp. 829–831.

[74] Alberto Girlando. “Charge Sensitive vibrations and electron-molecular vibration coupling in bis (ethylenedithio)-tetrathiafulvalene (BEDT-TTF)”. In: *The Journal of Physical Chemistry C* 115.39 (2011), pp. 19371–19378.

[75] A Girlando et al. “Discovery of vibronic effects in the Raman spectra of mixed-stack charge-transfer crystals”. In: *Physical Review B* 26.4 (1982), p. 2306.

[76] Jun’ya Tsutsumi et al. “Generation and Diffusion of Photocarriers in Molecular Donor–Acceptor Systems: Dependence on Charge-Transfer Gap Energy”. In: *The Journal of Physical Chemistry C* 116.45 (2012), pp. 23957–23964.

[77] Eric Daniel Głowacki et al. “Intermolecular hydrogen-bonded organic semiconductors—Quinacridone versus pentacene”. In: *Applied Physics Letters* 101.2 (2012), p. 023305.

[78] Eric Daniel Głowacki et al. “Hydrogen-Bonded Semiconducting Pigments for Air-Stable Field-Effect Transistors”. In: *Advanced Materials* 25.11 (2013), pp. 1563–1569.

[79] Steven De Feyter et al. “Aggregation properties of soluble quinacridones in two and three dimensions”. In: *Chemistry of materials* 14.3 (2002), pp. 989–997.

[80] CMF Oliveira et al. “Crystalline modifications of lineartrans-quinacridone pigments”. In: *Journal of materials science* 27.18 (1992), pp. 5101–5107.

[81] Gabriele D’Avino et al. “Electronic polarization in organic crystals: a comparative study of induced dipoles and intramolecular charge redistribution schemes”. In: *Journal of chemical theory and computation* 10.11 (2014), pp. 4959–4971.

List of publications

- Temperature-induced valence instability in the charge-transfer crystal TMB-TCNQ
  N Castagnetti, G Kociok-Köhn, E Da Como, A Girlando
  Physical Review B 95 (2), 024101; 2017

- Phenomenology of the Neutral-Ionic Valence Instability in Mixed Stack Charge-Transfer Crystals
  M Masino, N Castagnetti, A Girlando
  Crystals 7 (4), 108; 2017

- Mixed stack organic semiconductors: The anomalous case of the BTBT-TCNQF$_\mathrm{x}$ series
  N Castagnetti, A Girlando, M Masino, C Rizzoli, C Rovira
  Crystal Growth & Design 17 (12), pp 6255–6261; 2017

- Extensive study of the electron donor 1, 1, 4, 4-tetrathiabutadiene (TTB) and of its charge transfer crystal with TCNQ
  N Castagnetti, A Girlando, M Masino, C Rizzoli, MR Ajayakumar, M Mas-Torrent, C Rovira
  Synthetic Metals 235, 29-33; 2018

- Mixed stack charge transfer crystals: Crossing the neutral-ionic borderline by chemical substitution
  N Castagnetti, M Masino, C Rizzoli, C Rovira, A Girlando
  Physical Review Materials; article accepted for publication; 2018.

Acknowledgements

I'd like to express my deepest gratitude to my supervisor, Prof. Alberto Girlando, for welcoming me in this research group and for having mentored me in a new and fascinating scientific activity during the whole period of my doctorate course. An other special thanks to my co-supervisor Dr. M. Masino who has supported and trained me in many experimental activities. I'd like to thank all the other academic members of the research group of the University of Parma: Prof. Anna Painelli, Prof. Francesca Terenziani and Dr. Cristina Sissa.

I'd like to thank Prof. Enrico Da Como from the University of Bath for giving me the opportunity to spend a period of 3 months as visiting Ph.D. student in his lab. Here I learnt and experimented the techniques of vapor phase growth applied to organic CT materials.

I'd like to thank Prof. Concepciò Rovira, Prof. Imma Ratera, Dr. Manuel Souto and Dr. Marta Mas Torrent from the Institut de Ciència de Materials de Barcelona (ICMAB-CSIC), for hosting me in their research group for a period of 3 months as visiting Ph.D. student. In this period I was trained in electrocrystallization.

Thanks to all the people of the group of spectroscopists of the University of Bologna, Prof. Aldo Brillante, Prof. Elisabetta Venuti, Prof. Raffaele Guido Della Valle and Dr. Tommaso Salzillo for the stimulating scientific collaboration and their informal and friendly company.

Thanks to Dr. Francesco Mezzadri and Prof. Corrado Rizzoli for their collaboration, which providing XRD studies on our samples, resulted essential for the realization of this thesis project.

A special thanks to all the mates I met during my stay in the working group in Parma and with which I shared office, labs, sometimes stress and frustration, but especially the most pleasant and funny moments: Paola, Francesca, Domna, Somananda, Sergey, Francesco, Brunella, Marcello, Sara, Marco, Carlotta and Mattia.

Finally I'd like to thank my family for supporting and encouraging me throughout these three years: my father Imer, my mother Patrizia, my sister Chiara and my brother Davide.

A special, great "thanks" to Angelica.